Semiconductor Magnetoelectronics and Prospects for a Spin Transistor

Thesis by

Franklin Gregory Monzon

In Partial Fulfillment of the Requirements
for the Degree of
Doctor of Philosophy

California Institute of Technology
Pasadena, California

1999

(Submitted May 19, 1999)

©1999

Franklin Gregory Monzon

All rights reserved

Acknowledgements

The accumulated time and effort spent on the work described here strains the memory in such a way that it is sometimes difficult for me to know exactly how many people contributed directly to the work itself, let alone indirectly, by helping me in various non-technical ways. Moreover, the demands implicit in being one of the first students in a research group with an ambitious agenda are not readily expressed. In the small space available here I express my gratitude to those who affected the work most significantly.

For my training in equipment building, semiconductor fabrication, and all-around know-how I thank Andrew Cleland, Keith Schwab, and Tom Tighe, all of whom had the arduous task of being postdocs working on very difficult projects while also needing to pass some of their skills on to less experienced researchers. For giving me an extremely interesting project to work on, for providing the equipment to do the work with, and for supporting me in my pursuit of publications, talks, and general recognition amidst a pool of very smart people across the world I am grateful to my advisor, Michael Roukes. Without Michael's insights, the science obviously would not have not been possible. The experiments described in this thesis often required custom designs and parts and would have taken me much, much longer to do without the assistance of Nils Asplund in showing me how to machine different parts or in just doing it himself (usually in a humblingly efficient manner). Nils was also perhaps my biggest supporter throughout my six years at Caltech, providing optimism when I encountered walls of pessimism. For help with specific aspects of the work discussed in this thesis, and for assistance with the myriad frustrating aspects of constructing, maintaining, and repairing lab equipment, I thank Robert Blick (GaAs fabrication), Erik Henriksen (general fabrication), Mike Murphy (resonator displacement detection), Dave Patterson (local Hall effect), Selwyn Scharnhorst (transfer resistance), and Hongxing Tang (spin-coupled ballistic transport). With regards to the spin-coupled ballistics I also owe thanks to Mike Cross and Ron Lifshitz for very enlightening theoretical discussions and suggestions. Finally, the spin work would not have been possible without the high quality InAs material provided to us by Herb Kroemer's group, and specifically Mason Thomas and Hans-Richard Blank, at UCSB.

The environments of grad school at Caltech in general and in the Roukes group, in particular, are at times very intense, very frustrating, and overall, just plain hard. And, while I think I wouldn't have learned nearly as much had my time been filled with smaller challenges, I owe thanks to the many people who helped me maintain a balance in life so that my lessons could be learned without too much distress. I thank Biff Yamazaki and Pavel Svitek from the hockey team—without such legal means for full-contact activity my pent-up aggressions might have found less acceptable outlet. I thank Coach John D'Auria of the baseball team for allowing me the privilege of helping to coach what was consistently a group of super bright and good-natured undergrads. Thanks to the Phys Rev Netters for many soccer memories, to the Chainsaw Cowboys/Huggers for great memories of softball dominance, and to all the staff at Braun gym for providing a remarkable place to take one's mind off work.

Finally I want to thank specifically some of the great friends I made in grad school. In addition to the people mentioned above, these are who and what I will miss most about Caltech: Mike Kleeman, Lisa Thurston, Pat Chuang, Mike Slessor, Jon Hodowany, Dave Vernooy, and Bill Weber. I owe a great debt to my parents Nancy and Philip Monzon, and my brother Eric, for providing me with the tools and the support, throughout Princeton and Caltech, to persist and to be able to conclude 10 years of higher education with this original work. Last I thank Mi Chang for her love and support throughout this strenuous time in my life, during which my moods may not have been reasonable, but throughout which she helped me to maintain my sanity and perspective. Though I have doubtless left this scorecard incomplete, these are primarily the individuals who have made this thesis possible. My deepest gratitude to all.

Abstract

The first demonstration of spin-coupled electronic transport, in all-metallic devices, occurred over ten years ago. Although the development of similar ferromagnet/semiconductor structures poses unique difficulties, these devices are exciting because they afford the possibility of constructing active circuit elements based upon the manipulation of spin rather than charge.

In this thesis we clearly delineate the requirements that must be met in order to successfully implement a semiconductor spin transistor. We present extensive 4.2 K measurements of NiFe/InAs quantum well spin devices fabricated both by photolithography and electron beam lithography, both wet-etched and dry-etched. These measurements often exhibit strong magnetoelectronic phenomena, not based on spin transport, that complicate the demonstration of spin injection/detection. We use local Hall voltages to carefully characterize submicron ferromagnetic thin films in order to improve the switching behavior of our ferromagnetic contacts and to minimize stray field effects. We describe theoretical calculations for ballistic spin-coupled transport, along with careful on-chip electrical characterization, that reveal our InAs conduction channels to be adequate spin-preserving wires. We conclude that inefficient spin transfer across the NiFe/InAs interface severely degrades the spin polarization of the injected current. Though we therefore do not obtain a conclusive demonstration of spin transport even in our smallest devices, with injector/detector spacings of less than 1 mm, we make firm suggestions for future spin devices, including expectations for what consitutes a definitive demonstration of spin transport in a high mobility two-dimensional electron gas (2DEG).

From a physics standpoint, such a demonstration is very interesting because control of a semiconductor spin-polarized current offers possibilities both for experiments in spin dynamics without the use of high magnetic fields or optical-polarization schemes, and for the investigation of spin-scattering mechanisms in tunable-density (gated) devices. From an engineering standpoint, these same transistor-like devices are intriguing as novel memories or switches. Despite this, the development of semiconductor spin devices has lagged behind the advance of metallic multilayer (GMR) spin devices. This thesis addresses the difficulties

inherent in implementing semiconductor spin devices, with the aim of enabling the successful manufacture of a spin transistor in the near future.

Contents

1 Introduction 1
1.1 History of Spin Injection 2
1.2 Recent History 5
1.3 Summary of Chapters 6

2 Requirements for Spin Injection Devices 9
2.1 Metallic Spin Injection 9
2.1.1 Sample Geometry and Signal Strength 9
2.1.2 Qualitative Expectations for Different Experimental Setups 10
2.1.3 Quantitative Expectations 13
2.2 Improvements to the Spin Transport Model 15
2.2.1 Estimate of R_s for InAs 16
2.2.2 The Diffusive Case in More Detail 17
2.2.3 The Diffusive Case with Two Interfaces 19
2.3 Spin Scattering Mechanisms 20
2.3.1 Estimate of Rashba Precession 22
2.3.2 Estimate of Hanle Precession 25
2.4 Requirements for a Spin-FET 26
2.4.1 Control of the Ferromagnets 26
2.4.2 Control of the InAs 26
2.4.3 Control of the Ferromagnet/InAs Interface 27

3 InAs Device Fabrication 28
3.1 InAs Contact Etch 28
3.1.1 Wet Etching 28
3.1.2 Dry Etching 30
3.2 Ferromagnetic Contact Deposition 33
3.3 Device Isolation Etch 34

3.3.1 Wet Etching 34
3.3.2 Dry Etching 35
3.4 Metal Interconnects, Wirebonding, and Chip Mounting 36

4 Measurement of Photolithographically-Defined InAs Spin Devices 38
4.1 Device Layout 38
4.2 Measurement Setup 44
4.3 Probe Configuration 46
4.4 Measurement Results 47
4.4.1 Zero-Field Features 48
4.4.2 Hysteretic Features 52
4.5 Summary 63

5 The Local Hall Effect 65
5.1 Early Devices 65
5.2 LHE Round 2 67
5.2.1 Measurement Results 68
5.2.2 Analysis of the Dependence of ΔR_H on s 70
5.2.3 Analysis of the temperature Dependence of ΔR_H 73
5.2.4 Summary of PL LHE Devices 74
5.3 LHE Devices with Nanoscale Ferromagnets 74
5.3.1 Device Geometry 75
5.3.2 Measurement Results 76
5.3.3 Single vs. Multidomain Magnets 80
5.3.4 LHE Sensitivity 81
5.4 Summary 83

6 Spin Devices II: Electron-Beam Lithography 85
6.1 Ebeam Device Design and Implementation 85
6.2 InAs Ebeam Spin Chip Measurements and Results 92
6.2.1 InAs Characterization 92
6.2.2 Ferromagnet Characterization 96
6.2.3 Spin Device Results 98

6.3 Summary: Inefficient Interfacial Spin Transfer 103

7 Conclusion **106**

7.1 Spin-Coupled Ballistic Modeling 107

7.1.1 The Ballistic Hanle Effect 108

7.2 Rashba Precession 111

7.3 Interface Modeling Possibilities 114

7.3.1 A Simple Interface Model 114

7.3.2 Spin-Polarized Tunneling 117

7.4 Possibilities for the Future 118

Bibliography **121**

A Recipe for Ebeam Spin Devices **127**

A.1 Photolithography Routines 127

A.1.1 (A) Shipley Microposit S1813 positive PR for Liftoff 127

A.1.2 (B) Hoechst Celanese AZ5214-E negative PR for Liftoff 128

A.1.3 Descum 128

A.1.4 (C) PR as an Etch Mask 128

A.1.5 Photoresist Templates 129

A.2 Ebeam Lithography 129

A.2.1 Layer 1: SiO_2 Mask for Ferromagnetic Contacts 130

A.2.2 Layer 2: Ferromagnetic Contact Deposition 130

A.2.3 Layer 3: SiO_2 Mask for Isolation Etch 131

A.2.4 Layer 4: Metallization to Connect Ferromagnetic Contacts 131

B Calculation of Local Hall Fields **132**

B.1 Case 1: Calculation of $\langle B_z \rangle$ and ΔR_H for LHE Devices 132

B.2 Case 2: Calculation of $\partial B_z / \partial z$ 134

C Transfer Resistance Devices and Ballistic Modeling **138**

C.1 Landauer-Büttiker Formalism Applied to Spin-Polarized Currents 143

List of Figures

2.1 Schematic representations of the spin devices of Johnson and Silsbee. 10
2.2 Pedagogical diagram showing the basic components of a spin device. 11
2.3 Representative data from all-metallic spin devices, both polarize/analyze and Hanle geometries. 12
2.4 Schematic diagrams of the densities of states in the ferromagnets and paramagnet, with and without bias. 14

3.1 A representative InAs quantum well heterostructure. This was the structure used almost exclusively in the ebeam experiments. 29

4.1 The four PL device geometries. 39
4.2 Micrographs of two type I devices showing improvements in processing. . . 40
4.3 Micrograph of a type II device with sputtered contacts, one ferromagnetic and one normal. 40
4.4 Micrograph of a type III device with sputtered contacts. 41
4.5 Micrographs of two type IV devices, again showing processing improvements. 41
4.6 The layout of the first spin chip. 42
4.7 The layout of the second spin chip. 43
4.8 The layout of the third spin chip. 43
4.9 The layout of the fourth spin chip. 44
4.10 Schematic drawing of the measurement electronics. 45
4.11 Data showing the ZF1 feature from each of the four device types. 49
4.12 Examples of known magnetoresistive phenomena, in perpendicular magnetic field. 50
4.13 Five example magnetoresistive backgrounds found in InAs PL devices, in perpendicular magnetic field. 51
4.14 The three basic hysteretic signals observed in InAs PL devices, in parallel magnetic field. 52
4.15 Plots from one of our type I devices. 54

4.16 An example of the probe configuration dependence of measured phenomena in type I devices. 55
4.17 An example of the probe configuration dependence of hysteretic features in a type II device. 56
4.18 The modified type II device geometry. 57
4.19 The one example of hysteresis in a type II (mod or not) device in the R_m probe configuration. 58
4.20 More examples of hysteresis in type II devices in the R_x config. 59
4.21 Temperature dependence of the R_x signal in a type IImod device. 59
4.22 Type IV hysteretic phenomena. 61
4.23 Data from another type IV device. 62

5.1 Drawings of simple devices for characterization of local Hall voltages. 66
5.2 Data from early local Hall devices, both InAs and GaAs. 66
5.3 Drawings of 2nd generation LHE devices. 68
5.4 Micrographs of LHE devices. 68
5.5 Data from a LHE device at 4.2 K and 300K. 69
5.6 Measured dependence of ΔR_H on magnet separation s for two chips. 70
5.7 Temperature dependence of carrier density n_s, mobility μ, and apparent field $\langle B_\perp \rangle_{app}$ for GaAs LHE devices. 73
5.8 Micrographs of ebeam LHE devices. 75
5.9 Width dependence, at 300 K, of the hysteresis of small NiFe magnets with an aspect ratio of 10. 76
5.10 Hysteresis loops, at 300 K, for different aspect ratio (AR) magnets at the same width. 78
5.11 Evidence for incoherent switching in a 125 nm × 5 μm magnet at 4.2 K. . . 79

6.1 Micrograph of the chip layout for ebeam devices. 86
6.2 Two low magnification micrographs of spin devices. 87
6.3 Four micrographs of ebeam spin devices, both PMMA-masked and SiO_2-masked. 87
6.4 Micrographs showing slight errors in ebeam devices (SiO_2 series). 89
6.5 Micrographs showing more serious defects in ebeam devices (PMMA series). 90

6.6 Micrographs of wet-etched ebeam devices. 91
6.7 Micrographs of the multiprobe device, for characterization of the InAs and of the ferromagnets, that was part of each spin chip. 92
6.8 InA characterizations for two spin chips, one ion-milled and one wet-etched. 93
6.9 InAs characterization from four SiO_2-masked chips. 94
6.10 On-chip local Hall characterizations of two pairs of NiFe magnets. 97
6.11 Two more local Hall characterizations of spin device magnets, one NiFe pair and one CoFe pair. 97
6.12 Hysteretic phenomena from three ebeam spin devices. 99
6.13 Two more examples of hysteresis. 100
6.14 Data showing varied amounts of hysteresis in an in-line device with 500 nm contact separation and CoFe contacts. 101
6.15 Perpendicular field sweeps of two nonlocal devices (R_m configuration) showing transfer resistance backgrounds. 102
6.16 Perpendicular field sweeps of in-line devices (R_m config.). 103

7.1 Modeling results of the ballistic spin transresistance in an in-line geometry as a function of perpendicular magnetic field. 109
7.2 Schematic depiction of different electron trajectories, with differing spin orientations, which will undergo differing amounts of precession. 111
7.3 Modeling results for spin-coupled resistance vs. Rashba effective field in an InAs in-line device. 112
7.4 Schematic representation of the large difference between the Fermi energies and wave vectors in a ferromagnetic metal and a degenerate semiconductor. 115

B.1 Plots for B_z and $\partial B_z/\partial z$ vs. z for $x = 100$, 200, 300, and 400 nm. 136
B.2 Modeling results for the decay of B_z and $\partial B_z/\partial z$ with x. 137
B.3 Modeling results for the decay of $\partial B_z/\partial z$ vs. y for separations of 200, 300, and 400 nm. 137

C.1 Schematic drawing of a transfer resistance device. 139
C.2 Transfer resistance curves from 4.2 K experiments with InAs and from computer simulation. 139

C.3 Micrographs of PMMA-masked ebeam transfer resistance devices. 141

C.4 Maximum transfer resistance (at zero field) vs. lead separation for devices with channel widths of 0.5, 0.75, and 1 μm. 142

C.5 Simulation results of maximum transfer resistance vs. lead separation. . . . 142

C.6 Schematic representation of the basic components of our ballistic transport model with spin polarization and precession, for the in-line geometry. 144

List of Tables

4.1 A listing of the magnetic field-dependent features found in PL devices . . . 63

5.1 LHE chips A and B: Results from experiments and from the simple line charge model for the magnetic fringe field. 71

6.1 Carrier densities, electrical channel widths (out of 1.5 μm nominally), and mobilities for a sampling of ebeam spin devices. 95

Chapter 1 Introduction

The idea of injecting a spin-polarized electric current from one material to another is not a recent one. Such experiments have been performed for nearly 30-years, and the question of why one attempts such experiments deserves a brief discussion. Ferromagnetism is a phenomenon that is not, at least in a quantitative or predictive sense, very well understood. Thirty years ago this was even more true, but nevertheless it was shown that an electric current, sent through a ferromagnet, does in fact acquire a net spin polarization dependent upon the orientation of the ferromagnet's magnetization. These initial experiments allowed one to extract the polarization of conduction electrons in different materials. Though the relationship between these polarization values and the fixed, atomic or molecular, magnetic dipole moments in each material is not straightforward, it does indeed turn out that stronger ferromagnets have stronger conduction electron spin polarizations. Spin injection experiments thus became a tool for characterizing the interplay of electric and magnetic (or *magnetoelectronic*) material properties. The potential of such experiments for practical application in some kind of useful device was not, however, immediate.

Eventually the discovery of giant magnetoresistance phenomena, in 1988, provided a lucrative path for magnetoelectronic devices as nonvolatile memory elements. These all-metallic devices are not suitable as active circuit elements, though, due to the lack of tunability of the electronic properties of metals. For a device with power gain, one wants to be able to control the propagation of the spin-polarized current completely with on-chip tools, as in a field-effect transistor (FET) whose channel conductance is tuned by an electrostatic gate. Put another way, one would like to demonstrate a solid-state device whose operation requires no clumsy external biasing magnets. This point brings us to attempt spin injection using a semiconductor material in conjunction, of course, with the ferromagnets that provide the spin-filtering of electrons. Semiconductors are much more versatile than metals in this regard: their carrier densities can be varied through doping or gating and, less prominently but nonetheless significantly for certain applications, mobilities can be varied by more exotic means such as the epitaxial growth of heterojunctions. In addition, the accumulated body of knowledge concerning semiconductor processing is extensive: etching

recipes, masking materials, and deposition parameters are well known. The objective of the research presented here has been to make a first step in the demonstration of a ferromagnet/semiconductor device. This device, much like a conventional FET, has a current source, a current drain, and a channel in between with, in principle, a tunable conductance. Instead of two charge species (electrons and holes) providing this tunability, however, the operation of the spin-FET [1] is based on the manipulation of the spin (up or down) of the electron.

1.1 History of Spin Injection

The first experimental spin injection results were reported in 1971 by Tedrow and Meservey [2] using superconductor/insulator/ferromagnet tunnel barriers. Aluminum was used for the superconductor and aluminum oxide for the insulator. The experiments took advantage of the fact that, upon applying an external magnetic field, the superconductor quasiparticle density of states is split into spin up and spin down bands. This splitting, equal to the Zeeman energy of the electronic spins in the magnetic field, allows the superconductor to be used as a spin filter. By varying the voltage between the ferromagnet and superconductor, Tedrow and Meservey (T&M) produced a tunneling current sensitive to the detailed structure of the spin-dependent density of states in both the ferromagnet and the superconductor. Tunneling conductance was then deconvolved to give the ferromagnet's density of states. Values obtained for some of the elemental ferromagnets were 44% for Fe, 34% for Co, and 11% for Ni. These are remarkably proportional to the saturation magnetizations of the bulk materials: 1.714×10^3, 1.422×10^3, and 0.484×10^3 emu/cm^3 respectively [3]. That this is so may make intuitive sense but is by no means straightforward to calculate. Moreover, the question of whether majority or minority spins comprise the larger percentage of the tunneling current is similarly complicated (for some discussion of the detailed nature of the injected electrons see the references to Stearns [4], Slonczewski [5], and the references found at the end of Chapter 7, [88]–[91]). For the purposes of this Introduction these issues are not so important—the essential point is simply that conduction electrons in a ferromagnet are spin-polarized and that this polarized current can be injected into another material.

The work of T&M was carried on in a slightly different form in 1975 by Julliere [6] who

used Fe/Ge/Co junctions. The experiments were conducted at 4.2 K so that the Ge was insulating. The magnetizations of Fe and Co could be varied independently (that is, their coercivities were different enough that an applied magnetic field could switch the magnets independently), which resulted in modulation of the tunnel conductance. Based on T&M's analysis, Julliere expressed this magnetoconductance (the difference in conductance values for the parallel and antiparallel magnetization configurations) as $\Delta G/G = 2PP'/(1+PP')$ where P and P' represent the conduction electron spin polarizations in the Fe and Co. The maximum measured value $(\Delta G/G)_{V=0}$ was 14%, somewhat below the anticipated value, based on the polarizations determined by T&M, of 26%. However, Julliere pointed out that coupling between the ferromagnets, resulting in less-than-saturated magnets, or spin-flip scattering in the Ge or at the interfaces, could reduce the effect. This demonstration of spin-filtering without the use of a superconducting analyzer film opened up the possibility of spin injection at higher temperatures, although this would not follow for some time.

The next proposal for a spin injection experiment came from A.G. Aronov [7] in 1976. Aronov was principally concerned with amplification of electron spin resonance (ESR) signals in the presence of a spin-polarized current injected *directly* from a ferromagnet into a normal metal. The injected spins, he proposed, could then induce a polarization of the nuclei as the spins scattered. Most importantly, the spin relaxation length of electrons in aluminum was estimated to be on the order of 1 cm. We note that any estimate of spin scattering presumes a certain type of spin scattering mechanism. Different mechanisms will be discussed in Chapter 2, but it was not until relatively recently that spin scattering in semiconductors began to be probed experimentally.

The experiment most directly relevant to this thesis was reported by M. Johnson and R.H. Silsbee [8], initially in 1985. In this experiment an aluminum foil 50 μm thick was used as the normal metal (treated as a free electron or Pauli paramagnet) and Permalloy, a NiFe alloy, served for both the ferromagnetic injector and detector. The details of the spin-coupled signal detected in this experiment will be discussed thoroughly in Chapter 3, in connection with the InAs-based experiments which are the main topic of this thesis; however, the main result was that either by switching the magnetization of one of the ferromagnets at constant current, or by applying a magnetic field perpendicular to the sample plane so that conduction electron spins underwent precession in the Al, a spin-coupled voltage was measured. This signal was quite small: Johnson and Silsbee needed a SQUID voltmeter to

measure tens of picovolts deflection with tens of milliamps drive. Nevertheless, the spin-coupled signal was detectable up to 55 K (limited by the cryostat) and spin relaxation lengths of up to 450 μm were extracted. This work was later extended to devices in which evaporated Au was used as the paramagnet and Co was sometimes substituted for one of the NiFe magnets [9]. In this case the spin relaxation length was much shorter (just over 1μm) but the spin-coupled signal was still ostensibly present, and 1000 times greater.

The discovery of GMR in 1988 accelerated interest in spin-dependent phenomena. Most of this work has focused on the behavior of magnetoresistances in metallic multilayers [10], or multilayers with intervening insulator barriers, where layer thicknesses are on the order of tens of angstroms. Although the 1990 proposal by Datta and Das [1] of the InAs-based spin-FET device is significant because such a device has no analog in all-metallic structures (and it is this proposal that spurred the work in this thesis), the rapid progress of GMR—from discovery to implementation in the read heads of commercial hard drives in ten years—has made prospects for the practical application of spin-based semiconductor devices, as memories, slim. On the other hand, the fact that a multi-billion dollar industry relies increasingly on devices with spin-dependent operation places a high priority on the understanding of spin transport mechanisms in general. While devices have been rapidly developed, much of this progress has been based on phenomenological observations. Comprehension of how spin scattering mechanisms contribute to a given level of magnetoresistance, or of how certain materials should be chosen for maximal device performance, is not as advanced. Semiconductor systems are therefore still interesting, if more from the standpoint of characterizing the influence of material properties, or processing, on spin phenomena. Put another way, demonstrations of large or small spin-coupled signals in semiconductor-based devices could in principle be fruitfully applied to maximize, or at least avoid degradation, of similar phenomena in GMR or other devices dependent on spin scattering mechanisms. Furthermore, demonstration of the spin-FET device as proposed in 1990 would still be an important achievement. From a more purely physics standpoint, spin injection devices could be used to perform novel on-chip Stern-Gerlach or Aharonov-Casher experiments, or to investigate the possibility of utilizing electronic spins in coherence experiments for quantum computing [11].

1.2 Recent History

Before we leave the topic of spin injection history, a brief account of recent results is merited. On-chip injection experiments are rare, but one example of progress utilizes half-metallic materials (100% spin-polarized) to achieve spin-polarized tunneling into high-T_c superconducting materials [12]. Although off-chip methods for injection and possibly detection are much more prevalent, these are still very significant because their success increases the body of knowledge necessary for realizing a useful on-chip spin device. Prospects for spin-polarized scanning tunneling microscopy (STM) were raised in 1992 [13] by the demonstration of spin-polarized tunneling from a Ni tip into GaAs at room temperature, with detection via circularly polarized light emitted from the GaAs. A somewhat related class of experiments implemented a ferromagnetic electrode as a spin filter either for electrons photoexcited directly by circularly polarized light [14], or for electrons photoemitted first from GaAs by similarly polarized light, and then focused with electron optics [15] onto the sample. In both cases the samples were ferromagnet/insulator/GaAs structures and a modulation in the current, depending on the magnetization orientation of the ferromagnet, was detected.

A second class of experiments relies similarly on photoexcitation by circularly polarized light but relies on III-V or II-VI semiconducting materials doped with magnetic impurities to induce some measure of magnetism within the semiconductor itself. Such compounds include Mn-doped GaAs [16], Mn-doped ZnSe or ZnCdSe [17], and Mn-doped CdTe [18]. In both the ZnSe and CdTe systems, spin injection experiments with optically injected (and detected) spin polarization have been successfully demonstrated (at liquid helium temperatures). The results of the ZnSe experiments led to further experiments [19] on Si-doped (n-type) GaAs that resulted in surprisingly long spin relaxation times of tens of nanoseconds (at room temperature). By applying an electric field to similar n-type or undoped GaAs, nonequilibrium spin polarizations were transferable over distances up to 100 μm [20]. Finally, practical demonstration of tunable channel conductance has also been demonstrated, though perhaps less robustly, in InGaAs channels at 0.4 K [21], and in InAs channels at 1.3 K [22], by applying a voltage to a gate electrically isolated from the channel and measuring changes in Shubnikov-de Haas oscillations. In these experiments each piece of the spin-FET puzzle is demonstrated. However in no case are the pieces assembled within

one material system and used to make a solid state spin device. It is the objective of this work to illuminate some of the key issues involved in the implementation such a device.

1.3 Summary of Chapters

During the course of this work the main goal of an InAs-based spin device has led to several interesting side projects. The vast majority of the work has been heavily experimental, but related computer modeling work has also been undertaken. This diversity of work is reflected in the Appendix material and in the discussion of Chapter 5. Ongoing work on certain projects will be mentioned as the topics arise.

The focus of Chapter 2 is a more detailed discussion of spin injection concepts. We delineate specific requirements for successful implementation of a spin-FET and we discuss areas of relative progress and challenge, in anticipation of our experimental results, and with reference to possible improvements. In addition, we explain our expectations for InAs devices in light of the different spin scattering mechanisms at work in high mobility semiconductors as compared to metals.

In Chapter 3 we discuss the fabrication of InAs devices (a detailed account of some recipes is given in Appendix A). We describe recipes based on photolithography and we discuss deposition techniques. We point out problems specific to InAs quantum well heterostructures and potential solutions, which ultimately involved moving to electron-beam (ebeam) lithography. Finally, we mention issues regarding ebeam lithography recipes, such as masking materials, contacting procedures, and the inherent constraints imposed by device geometries.

Design and measurement of photolithographically-defined (PL) devices is the subject of Chapter 4. We reiterate expectations and explain their connection to the measured hysteretic phenomena, and discuss the influence of probe geometry in our PL devices, which are not quite in the diffusive regime of transport (the regime of previous all-metallic spin devices). We stress the importance of certain experimental checks on the validity of any hysteretic phenomena and point out how our devices can be improved (via ebeam lithography).

The work presented in Chapter 5 embodies a significant, but necessary, departure from our InAs work. We show how the interaction between the fringe magnetic fields of our

thin film ferromagnets and our low carrier density InAs channel can result in strong Hall voltages. The strength of these voltages depends on the detailed geometry of a device, and even on the micromagnetic structure of the ferromagnets themselves. In order to characterize the potential role of local Hall voltages in magnetoelectronic devices we fabricated and measured control devices in which the ferromagnets were electrically isolated from the conducting channel. We find that such devices are interesting in their own right, from the standpoint of characterizing the magnetic properties of small ferromagnets, and perhaps even as nonvolatile memory elements, and we discuss possible future improvements to these local Hall effect (LHE) devices. (Devices are analyzed more thoroughly in Appendix B.) Based on our work with the control devices explained in this Chapter, we were able to minimize local Hall voltages in our next generation ebeam devices.

Ebeam devices are the subject of Chapter 6. We show how we were able to characterize, on-chip, the quality of our nanomagnets and our InAs processing so that previous unknowns regarding expected device operation became well understood. We elucidate fabrication issues specific to ebeam devices with submicron dimensions. Certain key pieces of information regarding processing parameters, such as how much etching is required to achieve device isolation, comes from work with simple InAs transfer resistance devices (explained in more detail in Appendix C). Related to this, initial difficulties using electron beam resist as a dry etch mask were overcome by using SiO_2 masks patterned by liftoff. An unnerving lack of hysteretic features in the vast majority of these devices leads us to question the origin of the hysteretic features observed in previous PL spin devices. While spin scattering mechanisms are not as well understood as we would like in these devices (especially since they are ballistic), we note that the main source of uncertainty stems from the NiFe/InAs contacts. Variation in contact resistances seems unavoidable for devices processed with nominally the same parameters, therefore the quality of the interface from the perspective of spin-flip scattering events is unknown. We briefly mention more subtle conduction band alignment issues, prevalent in GMR research, that could result in inefficient spin injection and that lead one to consider other possible material combinations.

We conclude our discussion of InAs-based spin devices in Chapter 7. Preliminary modeling results regarding the role of ballistic transport in spin-coupled phenomena have yielded some insight into improvement of semiconductor spin devices, but more work is clearly needed. The assumptions and machinery of this modeling effort are treated more fully

in Appendix C. Preliminary efforts to better understand the ferromagnet/semiconductor interface are also described in this Chapter. We finish by discussing prospects for future spin-FET devices, given the results of Chapter 6 and the demonstrations of spin-dependent device operation in the literature.

Chapter 2 Requirements for Spin Injection Devices

We begin the discussion of the ingredients required for successful operation of an InAs-based spin device by discussing in more detail the work of Johnson and Silsbee. Their experiments, since they used on-chip injection and detection of a spin-polarized current, were the basis for our initial work. We then move on to a description of the semiconductor case and the important differences between this case and the all-metallic case. We conclude with a specific list of requirements for the successful fabrication of a spin device.

2.1 Metallic Spin Injection

2.1.1 Sample Geometry and Signal Strength

Figure 2.1 shows the basic layout of the two types of spin devices used in the two rounds of experiments of Johnson and Silsbee: (a) gives the geometry of the early experiments using Al as the paramagnet and (b) illustrates the later experiments using Au as the paramagnet. In (a) the device dimensions are quite large but this is compensated by the high purity of the single crystal Al, which in some devices had an electron mean free path of 17 μm, and hence correspondingly large spin diffusion lengths, δ_s, that approached 500 μm. The separation between injector (F1) and detector (F2) was varied between 50 μm and 300 μm and currents, I_e, of 30 mA or more were sourced through F1 and into the Al bar, *away* from F2. Voltage V_s at F2 was then measured with a SQUID picovoltmeter, with respect to ground at the end of the Al bar opposite the current ground. From this, Johnson and Silsbee extracted a spin transresistance, $R_s = V_s/I_e$. To reiterate: current and voltage paths do not overlap in this 4-terminal arrangement as in conventional 4-terminal resistance measurements. This nonlocal measurement configuration allows one to probe the spin-coupled component of transport arising from diffusion of spin-polarized electrons in the Al from one ferromagnet to the other, without potentially large background voltage offsets that result from ohmic drops associated with the drift component of transport. One can still obtain small background

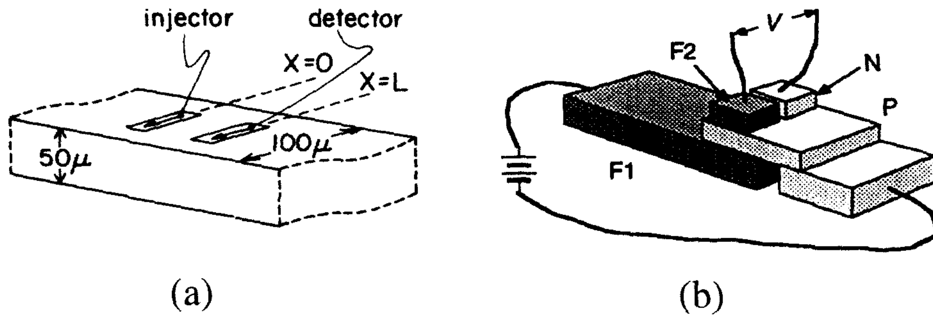

Figure 2.1: Schematic representations of the spin devices of Johnson and Silsbee. (a) Geometry used in the early experiments employing Al foil (from Ref. [8]). (b) Geometry used in the later work using thin film Au (from Ref. [9]).

offsets due to asymmetries in electric field gradients and Hall voltages in the Al bar, but these are unavoidable.

The drawing in (b) of Figure 2.1 illustrates the difference in device geometry between the two sets of metallic spin experiments. In the later experiments a sandwich structure was used, in which the two ferromagnets (usually NiFe, but sometimes one NiFe and one Co) were positioned on opposite sides of a 1.6 μm-thick disordered, polycrystalline, Au film. A second normal metal contact was positioned near the detector ferromagnet to allow for grounding of the detector voltage, so that once again the measurement was a nonlocal one (though not as cleanly as in the first case). For these experiments the injected current level was several mA and the magnitude of the spin-coupled signal was tens of nV (detection by rf SQUID)—much larger than in the first case. One possible reason for this is the much smaller size of the paramagnet. This should have been more than compensated, however, by a dramatic decrease in the size of δ_s, extracted as 1.5 μm, due to the much lower quality of the Au film compared to the Al foil. It was the surprising strength of the spin-coupled signal in this work that spurred the work in this thesis.

2.1.2 Qualitative Expectations for Different Experimental Setups

Figure 2.2 shows a simple diagram intended to highlight the components of a spin device. A current sourced through a ferromagnet, F1, acquires a spin polarization whose magnitude depends on the ferromagnetic material. Injection of this current into a non-ferromagnet, P (taken to be a free-electron paramagnet), induces a net spin polarization (represented as

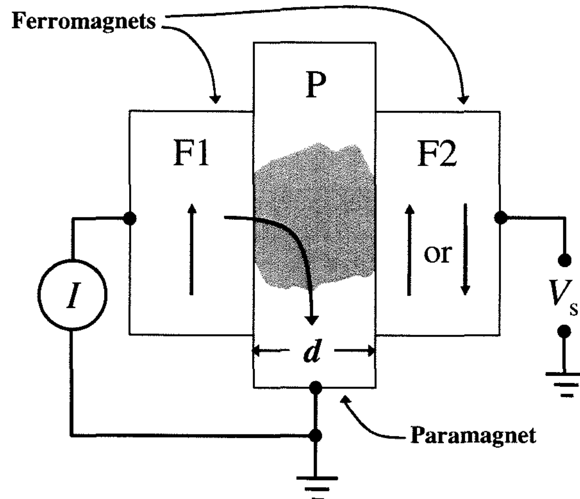

Figure 2.2: Pedagogical diagram showing the basic components of a spin device. The ground connection (current return) for P is made many spin diffusion lengths from the injection region, and therefore far from the cloud of induced magnetization (shaded region). The ground connection for the detected voltage is not necessarily the same as the ground for current return, allowing for nonlocal measurements, as described in the text.

a shaded cloud of magnetization in the Figure) that dies off with a characteristic length scale δ_s. Assuming the separation between the two ferromagnets, d, is less than this spin relaxation length, the second ferromagnet, F2, will interact with this spin polarization. This picture also assumes that d and δ_s greatly exceed the mean free path for momentum scattering. Note in the Figure that current and voltage paths do not share the same ground, for the reasons mentioned above. In the InAs devices discussed in this work, device dimensions are often *smaller* than the characteristic momentum scattering length, l_e. In this case electron transport cannot be considered in the same way as in diffusive metallic devices. We therefore note that, although we often started a round of measurements by probing in the nonlocal configuration, we would also look at other probe configurations. The magnetization current density injected into the paramagnet can be expressed as

$$J_m = \eta \frac{\mu_B J_e}{e} \tag{2.1}$$

where J_e is the electric current density; μ_B is the Bohr magneton, or magnetic dipole of each electron; e is the electron charge, and η is a phenomenological parameter measuring nonidealities such as partial polarization at the Fermi energy, differences in Fermi velocities, and different interfacial transmission probabilities, including inefficient spin transfer across

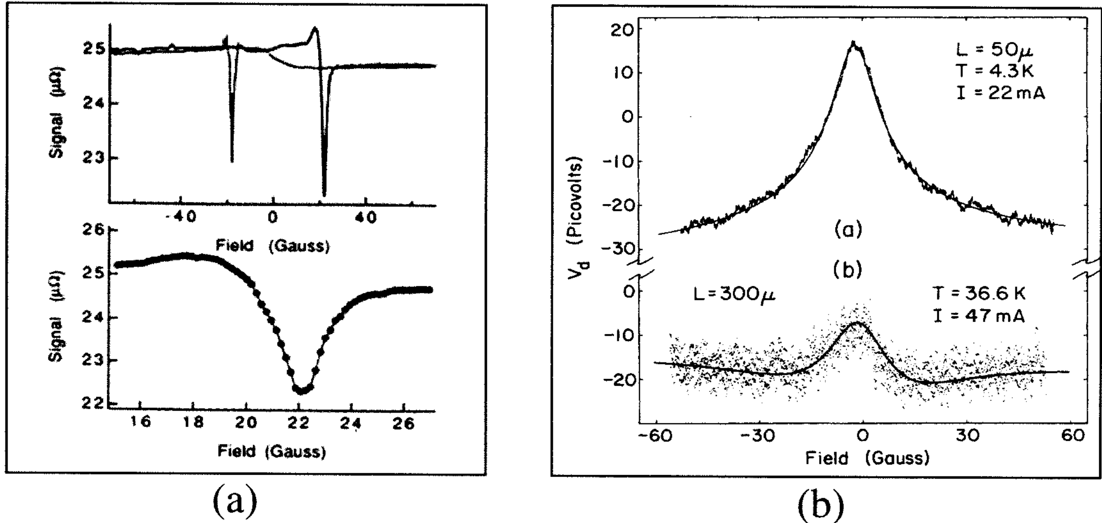

Figure 2.3: Representative data from all-metallic spin devices: (a) Polarize/analyze experiment [9] and (b) Hanle effect experiment [8].

the interface. In the early Al spin injection work, extracted values for η ranged from 0.043 to 0.075. In the later Au work, this model apparently broke down, since extracted values were greater than 1. (This result has not been duplicated, nor fully explained.) Problems with this simple view of injected magnetization will be discussed more below.

There are basically two different ways to probe the spin-coupled transport in these devices. The first of these, which we call the 'polarize/analyze' experiment in analogy with optical polarization of light, is the easier of the two to realize. In this experiment a magnetic field is applied in the plane of the sample, along the easy axis of the ferromagnets, so that sweeping the field from positive to negative field values results in switching of the magnetizations of the ferromagnets. One then looks for a voltage change at the detector when the injector and detector magnetizations change from parallel to antiparallel. Data from such experiments with the Au metallic devices are shown in Figure 2.3(a). The pronounced dips in voltage correspond to antiparallel magnetizations in the two NiFe contacts.

In the second experimental approach, termed the Hanle effect, the magnetic field is applied perpendicular to the sample plane (or, if in the sample plane, transverse to the easy axis of the ferromagnets). Sweeping this transverse field causes precession of the injected spins (we assume for now that the magnetizations of the ferromagnets remain unaffected by the transverse field). As the field bias is increased from zero, spins precess more as they diffuse from 'source' to 'drain' until the signal becomes weak and, eventually, vanishes

due to the variance in path lengths (and hence variance in accumulated precession). Note that in a single transverse subband all electron velocities are directed the same way, so one should be able to detect oscillations in the Hanle signal as electrons precess π radians, then 2π, and so on. However, in quasi-one-dimensional devices (with multiple occupied 1D subbands) and two- or three-dimensional devices, there is a range in path lengths taken by electrons in their traversal from injector to detector. When we integrate over contributing trajectories these add incoherently, and oscillations are suppressed. The Hanle experiment is somewhat harder than the polarize/analyze approach because it requires saturating the magnets with an in-plane field, and then applying a transverse field. The experiment is important, though, because it provides a crucial demonstration that a spin polarization exists in P. Representative Hanle data from the Al metallic devices (the only such unambiguous traces in existence in the literature for a spin injection device) are shown in Figure 2.3(b).

2.1.3 Quantitative Expectations

For the all-metallic case, a conceptual guide to the basic understanding of the origin of this spin-coupled voltage modulation is offered in Figure 2.4. The figure shows a series of density of states diagrams, each with spin down on the left of the vertical axis and spin up on the right. This represents the case in which the ferromagnets have parallel magnetizations. (The representation of the ferromagnet states is schematic only—in general the polarization of electrons transmitted out of the ferromagnet is sensitive to details of the interface.) At zero current bias, shown in (a), the Fermi levels in the injector (F1), paramagnet (P), and detector (F2) line up and the system is in equilibrium. When a current is turned on in (b), electrons are injected into P from F1; its down-spin population increases and the up-spin population decreases as current leaves P to close the loop (we impose an open circuit boundary condition at F2). The amount by which the Fermi levels of the two spin subbands are raised and lowered is determined by the steady state balance between spin injection and spin relaxation. (In a small device there can also be significant spin diffusion out of the 'active' region.) The open circuit boundary condition on F2, which corresponds to ideal voltage measurements, i.e. involving a high impedance voltmeter, requires that there be no net current flow into F2, so the down-spin chemical potential (or Fermi level) rises to match the chemical potential for down-spins in P. Note that we have assumed ideal Stoner ferromagnets, with 100% spin polarization at the Fermi energy, and a simple free-electron

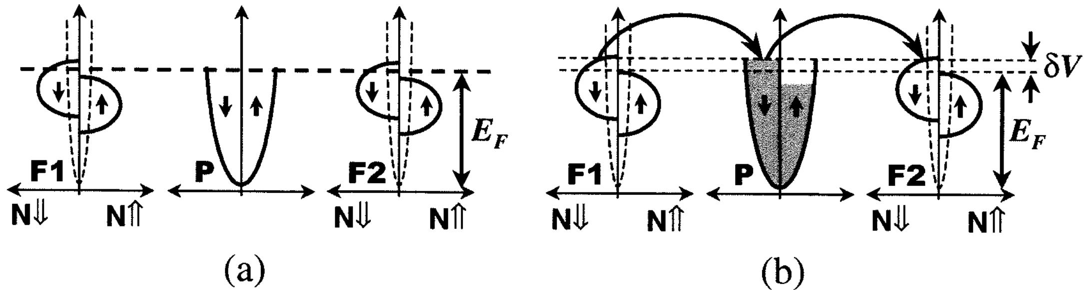

Figure 2.4: Schematic diagrams of the densities of states (horizontal axis) in the ferromagnets and paramagnet. In (a) the zero current bias case is shown while in (b) bias current from F1 to P preferentially builds up one spin population (shaded).

metallic paramagnet. Although this is not the case with the ferromagnets we use, the analysis proceeds similarly, with the exception that the voltage induced in the detector will not match the rise in chemical potential in P, but will be attenuated somewhat to satisfy the boundary conditions on both the up and down spin subbands [8].

Based on this simple model of injected magnetization we can now make a crude estimate of the spin-induced voltage, as it was originally derived in the work of Johnson and Silsbee. Magnetic moments are injected, per unit area, into P at the rate J_m, and in steady state are relaxed at the rate $1/\tau_{sf}$, where τ_{sf} is a simple relaxation time approximation for spin flip scattering (relevant for a k-space average over the Fermi surface electrons). Therefore the nonequilibrium magnetization, M, in P is

$$M = \frac{J_m \tau_{sf}}{d} = \frac{\eta_1 \mu_B J_e \tau_{sf}}{ed} \tag{2.2}$$

where d is the separation between F1 and F2 and η_1 is the non-ideality parameter for the F1-P interface. This result applies to the case $\delta_s = \sqrt{v_F^2 \tau_e \tau_{sf}/3} \gg d$ where v_F and τ_e are the Fermi velocity and momentum lifetime in P. The spin-induced voltage detected at F2 is proportional to the rise in chemical potential in F2 associated with the injected spins in P. Since M/μ_B is the number of non-equilibrium spins:

$$\eta_2 \frac{M}{\mu_B} = N(E_F) e V_s \tag{2.3}$$

or,

$$V_s = \frac{\eta_2 M}{e\mu_B N(E_F)} \tag{2.4}$$

where $N(E_F)$ is the density of states at the Fermi level. This is valid assuming linear response, i.e. that V_s is sufficiently small so that $N(E)$ has the roughly constant value $\sim N(E_F)$ over the range of energies of the injected electrons. Plugging in $N(E_F) = 3n/2E_F$, where n is the volume density of electrons in P, we arrive at

$$V_s = \frac{2\eta_1\eta_2}{3e^2}\frac{J_e E_F \tau_{sf}}{nd} \tag{2.5}$$

or, putting this in terms of a spin-coupled resistance (or transresistance, for nonlocal detection) $R_s = V_s/I_e$, with $J_e = I_e/A$ and A the area of the injection contact,

$$R_s = \frac{2\eta_1\eta_2}{3e^2}\frac{E_F \tau_{sf}}{nAd}. \tag{2.6}$$

Note that this result assumes uniform η parameters over the contact area A. Using this expression, values extracted for τ_{sf} from the original experiments with Al are between 1 and 10 ns, and for the Au experiments are just over 10 ps.

2.2 Improvements to the Spin Transport Model

We begin this section by applying the above equations to provide a simple first estimate of the size of the spin-coupled resistance in an InAs quantum well. The result has historical significance because its large magnitude provided our original incentive to attempt these experiments. A more careful accounting of the ballistic nature of electron transport in our high mobility InAs quantum wells will be addressed in Chapter 7, as will uncertainties regarding interfacial spin transfer.

2.2.1 Estimate of R_s for InAs

The potential magnitude of the spin-coupled voltage signal in a semiconductor 2DEG is, at first glance, much larger than in the all-metal case pioneered by Johnson and Silsbee. For a two-dimensional system like our InAs quantum wells, we know that

$$E_F = \frac{\hbar^2 k_F^2}{2m^*} = \frac{\pi\hbar^2 n_s}{m^*} \tag{2.7}$$

with m^* the electron effective mass in InAs (= 1/40 of the free electron mass [23]), $k_F = \sqrt{2\pi n_s}$ the magnitude of the Fermi wavevector, and n_s the sheet density of electrons. Plugging this into Eqn. 2.6 and substituting w for A for the two-dimensional case (w is the width of the injection region) we arrive at:[1]

$$R_s = \frac{2\eta_1\eta_2}{3e^2}\frac{\pi\hbar^2\tau_{sf}}{m^* w d}. \tag{2.8}$$

We do not know the appropriate value of τ_{sf} to represent the non-equilibrium magnetization decay in our InAs devices. In fact, as we discuss below, precessional mechanisms dominate, and a firm grasp on the spin-coupled ballistic transport can only be achieved by computational modeling. As a first approximation we take the value $\tau_{sf} = 1.75$ ps, obtained from weak antilocalization experiments [24]. This is likely to be a significant underestimate of the spin-flip lifetime for our experiments, since the weak antilocalization experiments probe the electron's phase-breaking time, which is a much more sensitive quantity. Also, in the absence of detailed knowledge of spin transfer across our device interfaces, we use a value of 0.05 for the parameters η_1 and η_2 (as was found in the original Johnson and Silsbee experiments). We further assume a relatively small device with $w = d = 1$ μm (which can be fabricated, and indeed was fabricated, using ebeam lithography). This gives us $R_s = 175$ mΩ, about *five orders of magnitude* larger than in the all-metallic Au experiments, and *eight* orders larger than in the Al experiments. More importantly, a signal of this strength is easily detected without a SQUID voltmeter: at a drive current of 10 μA we expect a spin-coupled voltage signal of order 1 μV. This estimate assumes that the device dimensions are smaller or comparable to the spin diffusion length, δ_s. We verify this by

[1] The result is approximate because, again, we have made the assumption that the η parameters are constant over the contact width. Also, the estimate is for 1D contacts, while in the experiments described later the contacts are 2D (although current crowding at the edge of the contact may result in approximate 1D line injection). This is mentioned again in Chapter 7.

taking $\delta_s = \sqrt{D_{el}\tau_{sf}}$, where the electron diffusion constant $D_{el} = 1/2(v_F^2\tau_e)$. We obtain then $\delta_s = 2$ μm for mobility $\mu = 2 \times 10^5$ cm^2/Vs, indicating that, optimally, our device dimensions should be on the scale of a few microns or less. This estimate for δ_s is flawed, however, as is explained below. Also described below are the assumptions included in the above estimate, and how a more exact model might change R_s. But we stress that the large magnitude of this estimate makes a good initial case for constructing spin injection devices using high mobility InAs electron systems.

2.2.2 The Diffusive Case in More Detail

Johnson and Silsbee considered the ferromagnet/normal metal interface in more detail in Refs. [25] and [26], taking into account spin relaxation in the ferromagnet and the normal metal, and interfacial resistance (which can in general be spin-dependent). Assuming a ferromagnet with spin imbalance p (which includes such things as differences in the density of states at E_F, Fermi velocities, and relaxation times in each spin subband)[2] their more general expressions for the magnetization current density and interfacial resistance are

$$J_M = \frac{\eta\mu_B}{e} J_e \frac{g_P g_F \left(1-p^2\right) + G g_P p \left(1-\eta^2\right)/\eta}{g_P g_F \left(1-p^2\right) + G\left(1-\eta^2\right)\left[g_P + g_F\left(1-p^2\right)\right]} \tag{2.9}$$

and[3]

$$R = \frac{1}{G} + \frac{g_P (p-\eta)^2 + g_F \eta^2 \left(1-p^2\right) + G p^2 \left(1-\eta^2\right)}{g_P g_F \left(1-p^2\right) + G\left(1-\eta^2\right)\left[g_P + g_F\left(1-p^2\right)\right]} \tag{2.10}$$

where G is the interfacial conductance in the absence of a spin imbalance and $g_F = \sigma_F/\delta_F$ and $g_P = \sigma_P/\delta_P$ are the conductances of segments of the bulk materials (with unity cross sectional area) of length equal to one spin diffusion length δ_F or δ_P.[4] In the limit $G \to \infty$ one obtains the result for the interfacial resistance,

$$R_{G\to\infty} = \frac{p^2}{g_P\left[1 + g_F/g_P\left(1-p^2\right)\right]}, \tag{2.11}$$

[2] If β represents the conduction electron contribution from the majority spins, then $p = 2\beta - 1$ (e.g., $p = 0.4$ if 70% of the electric current is made up of majority spins.)

[3] The numerator in the fractional part of the expression for the interfacial resistance could not be verified by the author. Rather, the expression $g_P\left(\eta^2 - p^2\right) + g_F\eta^2\left(1-p^2\right) - Gp^2\left(1-\eta^2\right)$ was obtained.

[4] Note the difference between the spin diffusion length, δ_P (or δ_s), and the spin relaxation length, l_s: in the normal metal $\delta_P = \delta_s = \sqrt{l_e l_s/2}$ where l_e is the elastic mean free path.

which was also obtained independently by van Son *et al.* [27], who considered the infinite interfacial conductance limit from the beginning of their calculation (and whose treatment is, therefore, less general than that of Johnson and Silsbee). The two approaches differ slightly in that Johnson and Silsbee derived their expression from thermodynamic considerations, taking into account a nonequilibrium injected magnetization as in Eqn. 2.2 whereas van Son *et al.* based their treatment on an analysis of the spin-resolved chemical potentials and conductivities near the interface.

Johnson and Silsbee point out that Eqn. 2.11 is valid for high interfacial conductance, i.e. $G \gg g_P, g_F$, an assumption that does not necessarily hold for typical metallic interfaces [26]. Nevertheless it is interesting to note the crucial role the ratio $g_F/g_P = \sigma_F\delta_P/\sigma_P\delta_F$ plays in the high transmission case of Eqn. 2.11. Assuming g_F is fixed we consider what influence the use of different normal metals has on the junction resistance. We expect that $\delta_P > \delta_F$ so that $g_F > g_P$ for similar conductivity materials. For $g_F \gg g_P$ we obtain $R \approx p^2/g_F(1-p^2)$. This is often termed the 'spin accumulation' or 'spin bottleneck' regime because spins injected into the normal metal relax slowly and the nonequilibrium magnetization builds up, significantly raising the chemical potential of the injected spins in both materials and hence increasing the interfacial resistance. If, on the other hand, spins relax rapidly in the paramagnet, then $R \approx p^2/g_N$. In this case there is no spin bottleneck because all spins injected into the normal metal are quickly relaxed, and the interfacial resistance is proportional to the square of the ferromagnet's spin imbalance.

If the interface is not highly conductive compared to the bulk materials then the spin distributions in each material are less strongly coupled across the interface and the magnetization transport is dominated by spin dependent transmission at the interface, through the parameter η. In this limit, Eqn. 2.9 reduces to Eqn. 2.1. For the ferromagnet/semiconductor system where contact resistances are relatively large compared to metal/metal contacts, this limit is perhaps the more relevant one.

Before moving on we note that the above results assume a sharp, clean (no spin-flip scattering) interface with diffusive transport on either side of the interface. However, the concepts of chemical potentials, conductivities, and diffusion lengths are spatial averages valid only on distance scales larger than the mean free path l_e. For our InAs where l_e is on the scale of several microns, and in fact the separation between injector and detector can easily be less than l_e, a different nonlocal treatment must be used to accurately capture the

interfacial spin dynamics. This will be discussed more in Chapter 7.

2.2.3 The Diffusive Case with Two Interfaces

Fert and Lee [28] considered the possibilities of non-zero interfacial resistance (contact resistance), interfacial spin-flip events, and spin relaxation in the ferromagnets independently in their model of all-metallic spin injection devices. Given the discussion above we will not consider their results in detail; however we will highlight their most interesting qualitative conclusions. Not surprisingly, the inclusion of spin relaxation in the ferromagnets and interfacial spin-flip scattering tend to reduce the size of the spin-coupled signal significantly (though not catastrophically). On the other hand, the inclusion of interfacial resistance (without an increase in spin-flip scattering) tends to have the opposite effect: higher contact resistances lead to better confinement of the carriers in P and hence to a reduction in the influence of relaxation in the ferromagnets. (This assumes the spin accumulation regime of Eqn. 2.11.) Fert and Lee, primarily concerned with understanding GMR and the reconciliation of the later Au experiments of Johnson [9] with GMR results, point out that contact resistances in metallic structures are normally too small, by two orders of magnitude, to enhance spin accumulation (in direct contradiction to the speculations of the work of Johnson). Moreover they acknowledge that an increase in contact resistances (often implying dirtier contacts) would likely increase spin-flip scattering too, so that any gain from the enhanced resistances would probably be nullified or worse. Finally we note that Fert and Lee find it impossible to reconcile the Au spin injection results with the existing body of GMR data (which is far more extensive). Possible reasons for these as yet unresolved discrepancies are discussed in the conclusion of this thesis.

The use of InAs as the paramagnet in a spin device does not affect the conclusions about spin relaxation in ferromagnets. However, the contact resistances at 4.2 K normally obtained in our work for NiFe on InAs are at best *seven* orders of magnitude higher than those quoted by Fert and Lee (10^{-4} Ωcm^2 vs. 10^{-11} Ωcm^2). This indicates that perhaps enhanced confinement of spins in P due to interfacial resistances may occur in InAs spin devices. Hard estimates of how this might help the situation are not feasible, however, because there is no knowledge of the extent to which spin-flip scattering takes place at the interfaces. For high enough contact resistances, one enters the regime of essentially decoupled materials mentioned as a limiting case at the end of the previous Section. In this

case we do not think in terms of spin accumulation, and there is no benefit from enhanced confinement of spins in P.

The structure of ferromagnet/semiconductor interfaces is not completely unknown, however. Epitaxial growth of Fe on GaAs was pioneered in the 1980s [29]. The researchers found that intermixing can occur, resulting in As and Ga in solid solution and Fe_2As and other compounds at the interface. The extent of this intermixing increased with increasing growth temperature. Later this work was extended and the magnetization loss of epitaxial thin films of Fe due to interfacial mixing was characterized as a function of growth temperature [30]. By fitting measured magnetization to expectations of magnetization strength at a given film thickness, the researchers deduced the existence of 'dead' layers with approximately half the magnetization of bulk Fe. Dead layer thicknesses varied from just under 1 nm at a growth temperature of 50°C to almost 6 nm at 250°C. These results are for GaAs substrates whose native oxide was thermally desorbed at around 600°C before the Fe growth. Attempts at growing better Fe using the native oxide as a barrier were not successful. However, by oxidizing the GaAs under O_3 so that about 2 nm of oxide was formed at the GaAs surface, Fe could be grown at temperatures up to 200°C without any detectable magnetization loss.

The influence of these magnetically dead layers on spin-flip scattering is unknown, but one expects a spatially varying magnetic environment at the interface to be detrimental. Other researchers have shown that similar intermixing occurs with Co thin films thermally evaporated on InAs [31], resulting in a several monolayer-thick layer with ferromagnetic properties. This layer was found not to be detrimental to contact resistances, both in magnitude and linearity, but, again, the role of spin-flip scattering in such layers is unknown.

2.3 Spin Scattering Mechanisms

The second problem with the estimates of Section 2.2.1 is in the details of the spin relaxation time, τ_{sf}.[5] In the case of metals, spin relaxation is normally caused by either a spin-orbit interaction with ions or impurities, or by a momentum relaxation process due to impurities or phonons [32]. These are termed Elliot-Yafet mechanisms after the originators of the analysis [33][34]. The result is that spin relaxation times are proportional to momentum relaxation times, and sometimes orders of magnitude larger (recent work has illuminated

[5]We note that in the work of Johnson and Silsbee τ_{sf} is written as T_2, as in electron spin resonance experiments (in the limit of zero external magnetic field, $T_1 = T_2$).

reasons for the large differences in spin relaxation times, for instance in Na and Al [32]). Thus, to maximize τ_{sf} in metals, one maximizes τ_e by going to low temperatures (eliminating phonons) and using high quality metallic films (as in the original Al spin devices). Note that these same spin scattering mechanisms are at work in low mobility semiconductors. Spin-dependent scattering by neutral impurities has, for instance, been measured in Si FETs [35].

In high mobility semiconductors the dominant spin scattering mechanisms are not the same. First, we note that the value we use for τ_{sf} in InAs was obtained from weak antilocalization experiments [24] which are very sensitive to phase coherence of electron spins. In our experiments we are not concerned with overall phase coherence, just in the preservation of an average spin polarization, so it is likely that the correct value for use here is somewhat larger.[6] In addition, the dominant mechanism for spin-dephasing in high mobility semiconductors is more accurately described as a spin precession process rather than as a spin-flip process. This is described below and in Chapter 7.

In Chapter 1 we mentioned that gate control for the spin-FET is based upon the premise that, by applying an electric field to an InAs quantum well, one can alter the rate of precession of the electron spins. But this can also be disadvantageous: in the III-V semiconductors, which lack inversion symmetry, there are always electric fields present. Similarly, in all heterostructures there are unavoidable fields due to asymmetries or band bending in the quantum well or 2DEG. Both of these constitute what are called D'yakonov-Perel', or DP, mechanisms [39]. The first of these, resulting from the intrinsic crystal field in a III-V semiconductor, is called the I term while the second, resulting from heterostructure asymmetries, is termed the Rashba effect, or R term [40]. In general the Rashba effect is larger in narrow bandgap semiconductors like InAs, while the I term may be larger in GaAs [41]. We can think of the Rashba effect in terms of an effective magnetic field in the quantum well, proportional to the cross product of the electric field (which is in the growth direction) and the velocity of the electron. Since the direction of the effective magnetic field is velocity-dependent, momentum scattering events that change or even reverse the axis of

[6] We can compare values in GaAs, for instance. The GaAs electron spin relaxation time is dependent both on magnetic field and material details: in 2DEGs it has been shown to be ~200 ps in zero magnetic field [36] and ~5 ns [37] at 2.6 T, while in bulk GaAs a value of 29 ns [20] has been measured at zero field (all of these are for optical pump/probe arrangements, where the electrons are hot and therefore spin relaxation mechanisms may be different from those for electrons at the Fermi surface). But in any case the spin relaxation time is much greater than the extracted value from weak antilocalization studies in a 2DEG: 25 ps [38].

precession tend, during an electron's propagation in space, to lessen the amount by which spins precess away from their initial direction. This phenomenon is similar to motional narrowing in electron spin resonance [42] and gives a spin-dephasing rate of

$$\tau_{so}^{-1} = \frac{\langle \Delta E_c^2 \rangle \tau_e}{4\hbar^2} \tag{2.12}$$

where $\langle \Delta E_c^2 \rangle$ is the Fermi-surface average of the square of the conduction band spin splitting and we write τ_{so} because the parameter, really a spin-dephasing time, does not describe spin-flip events directly.

Whether the I term or the R term is dominant in a given semiconductor heterostructure can be determined from the dependence of spin-dephasing phenomena on carrier density. For each term one can describe a spin-orbit field (which is not the same as the effective field mentioned above), given by $H_{so} = \hbar/(4De\tau_{so})$. For the I term this becomes

$$H_{so} = \eta n_s^2, \tag{2.13}$$

and for the R term,

$$H_{so} = \gamma \langle E_z \rangle^2, \tag{2.14}$$

where η and γ are material constants independent of carrier density, and $\langle E_z \rangle$ is the expectation value of the electric field perpendicular to the plane of the 2DEG. Thus, while the I term is quadratic in carrier density, the R term is independent of it. Antilocalization experiments on GaAs and InAs 2DEGs [24][38] confirm these dependencies and also verify that in InAs the R term is strongest.

2.3.1 Estimate of Rashba Precession

In this Section we roughly estimate the affect of Rashba precession on the ballistic electrons in the InAs quantum well. The Rashba Hamiltonian is usually written as

$$H_R = \alpha \left[\boldsymbol{\sigma} \times \mathbf{k} \right] \cdot \hat{z} \tag{2.15}$$

where the spin-orbit interaction parameter α is linearly dependent on $\langle E_z \rangle$ through the energy gap and the effective mass, $\boldsymbol{\sigma}$ represents the Pauli spin matrices, and $\widehat{z}$ is the direction of the electric field [40]. The total Hamiltonian, assuming that the Rashba effect dominates all other spin-coupled factors, is $H_{tot} = H_k + H_R$, where $H_k = \hbar^2 k^2 / 2m^*$ is the kinetic energy part of the Hamiltonian . The eigenstates for up and down spins are then [22]

$$E^{\pm}(k) = \frac{\hbar^2 k^2}{2m^*} \pm \alpha |k| . \tag{2.16}$$

So that the spin splitting energy, Δ_R, at zero magnetic field at the Fermi energy is

$$\Delta_R = 2\alpha k_F. \tag{2.17}$$

In traversing a distance L in the quantum well, an electron will precess an amount $\Delta\theta = \omega_L L / v_F$, where $\omega_L = (g^* \mu_B / \hbar) B_R$ is the Larmor frequency of precession for the electron in the effective Rashba magnetic field, B_R. But $B_R = \Delta_R / g^* \mu_B$ and $v_F = \hbar k_F / m^*$ so we obtain $\Delta\theta = \Delta_R m^* L / \hbar^2 k_F$. The angle through which an electron precesses in traversing a distance L is thus [43]

$$\Delta\theta = 2m^* \alpha L / \hbar^2. \tag{2.18}$$

Values for α given by Nitta *et al.* [21] and Heida *et al.*[22] range between 0.5 and 1×10^{-11} eVm, corresponding to an energy splitting $\Delta_R = 1.5$ to 6 meV. The material of Heida *et al.* is most similar to ours so we take the average values $\alpha = 0.55 \times 10^{-11}$ eVm and $\Delta_R = 2.5$ meV (this is similar to the value obtained by Chen *et al.* [24]). The spin of an electron thus precesses π radians after traveling $L = 0.86$ μm. We can put this another way by converting the energy splitting of the spin subbands into an effective field: $\Delta_R = g^* \mu_B B_R$. At $\Delta_R = 2.5$ meV, and using $|g^*| = 15$ for these InAs quantum wells [23], we obtain $B_R = 2.88$ T. The Fermi velocity of electrons in our structures is $v_F = \hbar / m^* \sqrt{2\pi n_s} = 1.24 \times 10^6$ m/s for $n_s = 1.15 \times 10^{12}$ cm^{-2}, hence they will precess at a frequency $\omega_L = \Delta_R / \hbar = 3.8 \times 10^{12}$ rad/s. This results in a propagation length, for π precession, of $L = v_F / \omega = 1.03$ μm, which is in relatively good agreement with the estimate of L given above.

This estimate does *not* necessarily mean that we have to build a device with contact separation less than 1 μm (although this is a good idea). There are three factors not

taken into account here; the first being elastic scattering, the second being scattering from device boundaries, and the third being the changing orientation of the effective field with respect to the spin. The first correction is likely not very significant in high mobility InAs because the elastic scattering time, approximately $\tau_e = 2.85$ ps for a typical InAs device after processing, allows ample time for precession: $\tau_e \omega_L >> 1$. (In fact we should not use Eqn. 2.12 because it assumes that $\tau_{so} > \tau_e$.) The second correction, the exact influence of sidewall scattering (both specular and diffusive), is at this time unknown, although future computer simulations, as discussed in Chapter 7, will illuminate the issue. However, assuming specular scattering, an electron feels opposite Rashba fields before and after each bounce against a device boundary. These effects tend to average out and not contribute to a loss of spin polarization. Diffuse boundary scattering may tend to enhance this loss of spin polarization, but the amount of diffuse boundary scattering needed before this becomes important is unclear (preliminary results of computer simulations suggests that boundary scattering in our devices may be at least 80-90% specular, but the exact value is yet unknown). The third correction is by far the most significant. The above estimate for L assumes that the electron velocity is directed such that the effective magnetic field is perpendicular to the electron spin, thus producing a maximum spin precession. If the spin and velocity are perpendicular, then, since the effective field is proportional to the cross product of the electric field ($\hat{z}$-direction) and the electron velocity, the effective field will actually lie parallel to the spin direction and no precession will result. Of course, the electrons have a distribution of velocities as they propagate down the channel so the velocity will never be perfectly perpendicular to spin (at least for our devices, in which the conduction channels are not quite one-dimensional[7]). Nevertheless, as we pointed out above, contributions to precession from specular reflections at sidewalls have a tendency to average out, so precession for the case of a channel oriented perpendicular to the spin direction (the magnetization direction of the ferromagnets) will be much less than estimated above. This geometry is precisely that of many of our spin devices, so we conclude that the above estimate for L is a worst case scenario not directly applicable to our devices.

The real influence of Rashba precession in our devices is, from experiments, unclear. Modeling efforts currently in progress are aimed at obtaining a more detailed understanding

[7] The number of occupied subbands in a 2DEG wire of width w is $N = k_F w/\pi$. Using a typical value of $n_s = 1.15 \times 10^{12}$ cm^{-2} and $k_F = \sqrt{2\pi n_s}$ we then obtain $N \approx 68$ for a wire of width 800 nm, as in our smaller devices.

of ballistic spin transport. Initial theoretical results will be discussed briefly in Chapter 7 and Appendix C. We note, though, that these results indeed confirm the above qualitative interpretations.

2.3.2 Estimate of Hanle Precession

We now consider the case in which a transverse magnetic field, $B_\perp$, is intentionally applied (the Hanle effect) to induce precession of the spins. The Larmor precession frequency is $\omega_L = \gamma B_\perp = (g^* \mu_B/\hbar) B_\perp$ and, in general, electrons propagating from one contact to another travel along different trajectories, hence involving different path lengths. This variance in path lengths, in turn, results in a variance in spin precession over the electrons' traversals through the device. Since the integrated contributions of these different amounts of accumulated precession determine the non-equilibrium magnetization detected at F2, this magnetization is attenuated more the greater the variance in spin precession of the electrons.. The injected magnetization is destroyed on a characteristic field scale $B_\perp \approx \pi(\gamma \delta t_{TR})^{-1}$, where $\delta t_{TR} = \langle t_{TR}^2 - \langle t_{TR}^2 \rangle \rangle^{1/2}$ is the variance in path lengths followed through the device. This field value, corresponding to π radians of spin precession, determines when the magnetization is decreased to half its zero field value [8]. From the above discussion (second estimate for L) the time it takes for a spin to precess 1 rad is 0.83 ps—electrons that take more than this time to reach the detector are considered scattered and thus are part of the non spin-coupled background resistance. With the precession frequency of $\omega = 1.32 \times 10^{12}$ rad/s, per Tesla, we then obtain a characteristic field of 1.1 T. This estimate is intended only as a guide to the field scale we may be dealing with. Due to the ballistic nature of our devices the actual value could be substantially different, and in fact the correct value can only be predicted by considering the detailed electron trajectories. Again, preliminary modeling results are discussed in Chapter 7.

There are certainly quantitative unknowns in the expectations for our ballistic spin devices. Nonetheless, the above discussion indicates that, at least for devices with channel lengths on the order of a micron (and perhaps significantly larger than this) spin-coupled transport in a properly designed InAs device should be observable, provided that the ferromagnet/InAs interfaces allow injection of spin-polarization in the first place. Our aim has been to highlight key issues involved in the design and implementation of such a spin device. Within this framework we are prepared to discuss requirements succinctly.

2.4 Requirements for a Spin-FET

The basic requirements for successful implementation of a spin-FET fall into three categories. With the fulfillment of these stipulations, one should be able to build a spin device with on-chip injection, detection, and control. The implementation is complicated however, due to the fact that the requirements are often sensitive to material parameters that are difficult to control and may not even be well understood.

2.4.1 Control of the Ferromagnets

Control over the magnetic properties of the injector and detector ferromagnets is essential to the performance of any magnetoelectronic device, but in the case of a spin device this is even more critical. For polarize/analyze experiments, one first needs to be able to switch the injector and detector independently. Coercivities of the two magnets must therefore be distinct enough to allow this. Better device performance will occur if the two magnets have well defined stable states (remanent magnetizations) at zero field bias, so that parallel and antiparallel transport properties can be probed without worrying about the volatility of the device state. In keeping with this, the micromagnetic details of the magnets are important. Magnet edges, which often have closure domains, should be removed from the injection region as much as possible. The surface underneath the magnet should be smooth enough not to cause perturbations to the magnetization. For instance, even if a magnet is 90% magnetized in one direction, if some of the remaining 10% of randomly oriented domains are positioned on top of the injection region they could dominate the injected current and result in no spin polarization induced in P. Control of ferromagnets was eventually achieved to a high degree. This is discussed in detail in Chapter 5.

2.4.2 Control of the InAs

The growth of InAs quantum wells with good transport properties (high mobility and carrier density, no magnetic impurities, no parallel conduction paths, good uniformity) is not addressed here, although it is obviously crucial to building a device [44][45]. We will, however, discuss in detail the patterning of the heterostructure material. InAs and the associated compounds GaSb and AlSb that provide the quantum well confinement are not easy materials to work with. Besides issues of fragility one must be able to surmount

difficulties intrinsic in fabricating a multilayer semiconductor device without destroying it in the process. For example, any dry etch recipe must work at low enough voltages not to damage the thin conducting layer [49]. These restrictions may seem self-evident, but they are by no means trivial in the design and construction of a device. Fabrication challenges in this work were for the most part successfully addressed. Details provided in Chapters 3 and 6, and in Appendix A.

2.4.3 Control of the Ferromagnet/InAs Interface

The first challenge in designing on-chip injection of spin-polarized electrons into a semiconductor is to determine a way to achieve ohmic contacts (operative at low temperature) directly to the semiconductor. Both GaAs and Si devices typically require some degenerately doped region underneath a metallic contact in order to avoid rectification. In the case of buried 2DEGs this is even harder, and, at least in the case of GaAs, one normally diffuses in some combination of metals at high temperature to achieve proper contact. This requirement does not exist for InAs, which has the remarkable property that small ohmic contacts can easily be made to it with, apparently, any metal (as far as we can tell), without alloying. Besides the possibility of gate control of spin precession in InAs, it is thus also useful because planar metallic ohmic contacts can be formed easily. The magnetic quality of the ferromagnet/InAs interface appears to be a much more difficult problem however. As describe in Section 2.2.3, mixing of metal and semiconductor species at the interface results in a layer of ambiguous magnetization whose spin-flip scattering properties are unknown. Moreover, subtle band alignment issues could play an important role in spin injection. These issues are still unresolved, and will be discussed again in Chapter 7.

Chapter 3 InAs Device Fabrication

In this Chapter we discuss the basic steps required for making InAs spin devices. The basic components of either photolithography (PL) or electron beam lithography (ebeam) recipes are: 1) etch through cap layers to InAs, 2) deposit ferromagnets over InAs contact areas, 3) etch through cap layers and through InAs for device isolation, 4) deposit metal for interconnects and wirebonding. We used Microposit 1813 photoresist for most of the photolithography work, with liftoff steps accomplished by a brief chlorobenzene soak. Although no PL spin devices took advantage of it, later photolithography for liftoff was accomplished with negative AZ5214-E resist, without chlorobenzene. Ebeam lithography for liftoff was typically achieved with a bilayer of polymethyl methacrylate (PMMA) and subsequent develop in a 3:1 solution of isopropyl alcohol:4-methyl 2-pentanone. A detailed listing of some recipes is given in Appendix A.

3.1 InAs Contact Etch

A typical heterostructure used in these experiments is shown in Figure 3.1. Reasons for the different layers [44] will not be discussed, but we note that in all of the heterostructures used in this work, the 15 nm thick InAs quantum well was confined between AlSb, and a thin cap layer of GaSb prevented oxidation of the AlSb. Total thickness of cap layers was either 15 nm or 20 nm. Also note that the material is undoped. Such 'not-intentionally doped' InAs heterostructures are common because Fermi level pinning [45] results in n-type conduction through even bare InAs.

3.1.1 Wet Etching

Fragility of the heterostructures was most evident in attempting to reproducibly etch contact windows and subsequently deposit the magnets on top of them. Both GaSb and AlSb are sensitive to a wide variety of bases, including photoresist developers. In addition, AlSb is known to be a relatively volatile compound that oxidizes and, in some cases, forms amorphous Sb by-products that impede etching, even under continuous agitation [46]. In

GaSb cap layer 10nm
GaSb 2.5nm
AlSb 2.5nm } x 2
InAs quantum well 15nm
AlSb 2.5nm
GaSb 2.5nm } x 3
AlSb 100nm
GaSb 2.5nm
AlSb 2.5nm } x 10
GaSb 1.2μm
AlSb 2.5nm
GaSb 2.5nm } x 10
AlSb 80nm
GaAs substrate

Figure 3.1: A representative InAs quantum well heterostructure. This was the structure used almost exclusively in the ebeam experiments.

contrast to the antimonides, InAs is a relatively stable compound that withstands the effects of many bases and is not readily oxidized. Selective wet etches are therefore possible. Most of the wet etching for our spin devices was accomplished using a solution of NH_4OH: H_2O (1:5), a highly selective etch between the antimonides and InAs. Our photoresist served as an adequate mask for this wet etch. We found that the NH_4OH:H_2O mixture degraded somewhat with time so that etch times became longer as we used a solution over the span of a few days. We encountered a variability in etch times, likely related to the volatility of AlSb and changing ambient conditions, that was never characterized because the photolithography tolerances did not demand tight control. Between 90 s and 4 min. were required to etch down to the InAs layer, at which point etching seemed to stop. Rough calibration of the etch was accomplished simply by watching for color changes—a green color was in most cases indicative of exposed InAs. Finer calibration was achieved at first by using a Tencor Alphastep that could measure step heights of 200 Å fairly reliably with one scan (which took several seconds), with somewhat better resolution attainable by averaging several scans. Later a Digital Instruments Nanoscope 3100 AFM was available and two-dimensional scans with vertical resolution of a few Å could easily be measured.

During the course of this work we tried other recipes for etching the antimonides. An example of this is Shipley MF319 photoresist developer, which other groups have used as a selective etch for similar heterostructures [46][47]. We found however that prolonged (few

minutes) InAs exposure to MF319 would in fact cause holes to develop in the InAs. Using our AFM to characterize the roughness of etched regions, we also found that even after a few minutes of etching, during which most of the cap was removed, there were still small spires of cap material left behind. These remnants were stubborn and required more etching, significantly increasing the InAs exposure to the developer solution. MF319 was therefore never used in the fabrication of a device (we note that some of our problems with this etch could be dependent on the specifics of our heterostructure).

We also attempted to find a photoresist developer that would not attack our GaSb, since initially we did not want removal of the cap material in all regions underneath the ferromagnets in our PL devices. Brief tests with CD30 and AZ developers were unsuccessful. We found that in the case of the CD30 developer, the etching rate was slower than for MF319, but we did not pursue this further.

Finally we mention that some effort was given to wet etching of devices patterned by ebeam lithography. We encountered difficulty, however, controlling the undercut beneath the PMMA (which served as the etch mask). In these runs we prepared a new NH_4OH: H_2O solution before each etch and etch times were relatively stable around 90 s. Contact windows were typically less than 1 μm wide so color changes, which had been a useful guide in PL devices, were relatively useless simply because we could not see clearly into the windows, even after good developing and etching. If an etch was perfectly executed, undercuts could still be on the scale of 200 nm or so. Note that this seems anomalously long: for an isotropic etch one would predict that the etch depth, 20 nm, would also be the scale of the undercut. The probable explanation is that AlSb is harder to remove than GaSb, so an etch can laterally eat through a large amount of GaSb before the thin AlSb layers are removed, in the vertical direction. This was not deemed acceptable (although some wet etched ebeam devices were made) in conjunction with the problem of residual spires of cap material (which happened to some degree with the NH_4OH: H_2O solution as well as with MF319 developer). Some researchers have found wet etches for GaSb that do not have a similar undercut problem [48], but in this case the etch does not remove AlSb.

3.1.2 Dry Etching

Even before the switch to ebeam lithography, we experimented with dry etching of contact windows for both the contact and isolation etches. The process utilized in a great number

of devices was Ar ion milling with an acceleration voltage of 150 V, a beam voltage of 150 V, and a beam current of 10 mA. Neutralization of the ion beam was achieved by discharge of electrons from a hot tungsten filament. Calibrated first by Alphastep and later by AFM, this etch was found to be very reproducible: a 2 minute and 30 second etch would remove 20 nm of cap material, to within 1 nm or so. This reproducibility was essential, because in this case there is almost no difference in etch rates between the antimonides and InAs. Unlike the wet etches, ion milling proved to result in very smooth surfaces. Damage from the ion beam was not characterized in detail, although there is evidence for a mobility reduction in the InAs underneath the contact windows. In this regard InAs is more robust than GaAs 2DEGs, where ion energies of a few hundred eV are known to destroy the 2DEG [49]. In PL devices, where the photoresist was the etch mask, we encountered some problems in the removal of the photoresist. In regions exposed to the beam, the photoresist formed a tough film that was not removable in room temperature acetone. Usually some combination of heating the acetone and placing the beaker in an ultrasonic bath would eventually remove the photoresist in these regions.

Ion milling for the contact etch was used extensively in the fabrication of ebeam devices. Although beam damage also occurred for PMMA, we found that we could etch and then deposit the ferromagnets and still have successful liftoffs most of the time. Residual bits of PMMA were in some case left in the contact windows, but the majority of the time the process looked clean. Removal of PMMA in acetone after ion milling was more difficult than removal of damaged photoresist. If no residual PMMA was present near devices, we would ignore the remnants. If removal was necessary, heating the acetone and ultrasonication would sometimes help, but the only reproducible solution was oxygen plasma stripping. This was undesirable, though, because it left behind a layer of oxide on the chip that interfered with later isolation etching. Removal of the oxide layer could be achieved by a brief dip in an acid solution (HCl:H_2O 1:10 was often used), but then possible damage was inflicted to the GaSb cap. These difficulties were irritating but usually did not result in the destruction of a chip. Nevertheless the move to SiO_2 etch masks was a significant improvement.

The addition of an SiO_2 mask step increased the number of ebeam layers in the fabrication of a chip but resulted in more reproducible processing. Typically we deposited SiO_2 in a pattern that left exposed all areas of the chip intended for either contact or isolation

etches. We then left the SiO_2 alone for the remainder of processing (attempts at removal with buffered oxide etch, an HF-based solution, were found to damage the antimonides and the InAs.) The SiO_2 was deposited by electron beam evaporation, in thicknesses of approximately 1200 Å-1400 Å. We found this to serve as an excellent mask for both Ar ion milling and later electron-cyclotron-resonance (ECR) recipes that involved both Ar and Cl_2. The actual deposition process was relatively tricky because SiO_2 is a poor thermal conductor and was prone to forming hot spots in the crucible. These would then cause uncontrolled surges in the evaporation rate. When this happened film quality would sometimes suffer and liftoff would fail because the SiO_2, evidently strained, would pull up from the GaSb. Such difficulties almost never occurred when the evaporation rate was kept low (< 2 Å/s). After deposition of SiO_2 the contact etch proceeded as before, with a 2:30 minute ion mill. We then carried out another round of ebeam lithography to define contact windows for deposition of the ferromagnets.

Recent construction of an ECR system has allowed finer control of etching. The literature mentions two prominent recipes for ECR etching of InAs heterostructures. The first, which utilizes a combination of H_2 and CH_4, is not a good etch for AlSb [50]. The second possibility uses He and Cl_2 with flow rates in a ratio of 9:1 [51]. (Pure Cl_2 etches the antimonides, but He is added to help with the physical removal of etch by-products.) We tested extensively the etch timing while varying chamber pressure and rf bias, normally while flowing 18 sccm of Ar and 2 sccm of Cl_2. For unknown reasons, etch timing was not as reproducible as in ion milling. We typically etched at pressures ranging from 1.5 mTorr to 2 mTorr, with whatever rf bias resulted in a dc self-bias of 50V. (We used rf biasing to avoid problems with static charging at the chip's surface.) Etch times, calibrated by measuring step heights with our AFM, were usually around 3:15 minutes. Again, etch depths could be controlled to within 1 nm by doing a calibration run just before the real etch. Etched surfaces were very smooth. Somewhat surprisingly, the etch was not very selective with respect to InAs. The antimonide cap layer was removed about twice as quickly as a comparable thickness of InAs. In some cases we therefore ran without Cl_2 and obtained good results with slightly longer etch times. ECR etching is preferable, in principle, to ion milling because the ion voltage is substantially less (here about 50V vs. 300V). We did not detect, however, any significant difference in ECR-etched device performance compared with that of ion milled devices.

3.2 Ferromagnetic Contact Deposition

The deposition of our ferromagnetic contacts, whether composed of NiFe or Co, was essentially the same for both PL and ebeam devices. Early on (in most of the PL devices) we experimented with sputtering of ferromagnets, but this was abandoned due to concern over possible damage to InAs from the high self-biases (> 800 V for our targets) encountered in rf magnetron sputtering. (Similar sputtering completely destroys GaAs 2DEGs, and while the InAs devices remained conductive after sputtering, we did not want to risk any damage.) For PL devices, thermal evaporation was the primary means of deposition, while for ebeam devices ebeam evaporation was more extensively used. This division is the result of historical circumstance. Thicknesses of the ferromagnets varied from around 800 Å for PL devices to 500 Å for most ebeam devices to 200 Å for ECR-etched ebeam devices. Thinner magnets in general gave better performance because the magnetizations were then better confined in-plane (this is discussed more in Chapter 5). In all but the ECR devices, the chips were mounted, before deposition, on top of a rectangular block of AlNiCo (a ferromagnet) so that the long axis of the magnets would lie along the direction of the magnetic field provided by the AlNiCo. This was done to aid in the establishment of an easy axis of magnetization in the deposited magnets. Although this helped with larger magnets, for the thin ebeam-defined magnets the step was unnecessary. Shape anisotropy proved to be a key ingredient in realizing good magnetic characteristics. After evaporation of the ferromagnetic material, we deposited a few hundred Å of Au to prevent oxidation of the ferromagnets. Base pressures for all evaporations were less than 10^{-6} Torr.

For PL devices there was a possible source of damage in this step due to the fact that the MF 319 developer, which we used to define the ferromagnet windows in the photoresist, attacked the cap layer materials. We attempted to minimize this by carefully timing develop times, but slight damage was unavoidable. In some cases adhesion of the ferromagnets would suffer due to this. The quantitative effect of this slight etch damage is unknown, however.

In the case of ion milled ebeam devices using PMMA as the contact etch mask, there was no intervening lithography between contact etch and magnet deposition. Upon removal of samples from the ion mill vacuum chamber they were loaded into the thermal evaporator as soon as possible. Nonetheless, an interval of about 5 minutes during which the InAs windows were exposed to air was unavoidable. Since this allows for adsorption of water

vapor or other contaminants on the InAs surface it is preferable to deposit magnets on top of a clean InAs surface, without breaking vacuum.

For ECR-etched devices this *in situ* contact formation was possible. After performing the contact etch (which could be done by any dry etch, but in this work was always ECR) we ebeam-wrote the contact windows and then loaded the sample into the ECR chamber. We then executed a brief (3-10 s) Ar ECR etch at 50 V bias in order to remove any surface contaminants from the InAs in the just-developed windows. Next we transferred the sample to the adjoining vacuum chamber, which had 3 sputter guns and a simple one-boat thermal evaporator port. The evaporator port also had its own gate valve so that different materials could be sequentially loaded and deposited without breaking vacuum on the sample. This process yielded the cleanest devices discussed in this work.

Finally we mention that not all InAs contacts in our devices are ferromagnetic. Besides the injector and detector, each device has two large, normal, contacts far from the ferromagnets. These contacts, in all cases defined by photolithography, are simple squares of thermally evaporated Cr/Au over bare InAs.

3.3 Device Isolation Etch

As with the contact etch, the device isolation step was accomplished in various ways depending on the size of devices and the equipment available.

3.3.1 Wet Etching

For PL devices, isolation was achieved by first wet etching down to the InAs with the same NH_4OH:H_2O solution used for the contact etch, using photoresist as the mask. After the cap materials were etched away, the samples were thoroughly rinsed in deionized water and then submerged in a solution of CH_3COOH:H_2O_2:H_2O (5:1:5) which selectively removed the InAs. This step was more reproducible than the antimonide etch and was normally over within 12 s. Again color changes were visible as the etch proceeded. Characterization of step heights by Alphastep and AFM confirmed the removal of the InAs. Though the InAs etch is faster than the antimonide etch, it did not seem to result in significant undercut problems. After removal of the InAs there would sometimes be changes in the appearance of the surface of the chip in the exposed regions, most likely due to some oxidation of exposed

AlSb. When storing chips, we thus left photoresist or PMMA spun on to reduce exposure to air. Transport measurements on completed chips left unprotected over intervals of a few months revealed no significant degradation.

Wet etching for both PL and ebeam transfer resistance (discussed in Appendix C and Refs. [52][53]) devices was also carried out. These devices, which are simple one-layer patterns, were used to characterize the degree to which transport was ballistic. The degree to which boundary scattering (the scattering at channel edges or sidewalls) was specular could also be probed in this manner. Results showed that the isolation etch resulted in high-quality InAs channels with mean free paths on the order of a few microns. Experiments with such devices provided a useful check on the impact of our etching recipes on the heterostructure.

3.3.2 Dry Etching

Before construction of the ECR system, all dry isolation etches were carried out with Ar ion milling, as in the contact etching, but for longer times. Initial results at 5:15-5:30 minute etch times, at which point the InAs was just barely removed, looked promising in that the surface color and measured step heights were consistent with InAs removal. Characterization of the degree to which devices were isolated, however, via independent measurements on transfer resistance devices, showed that supposedly separated devices were connected by resistances of as little as 10 kΩ at 4.2 K. Since device resistances were often on the scale of a few thousand ohms or more this was unacceptable. Increasing etch times to 6 minutes increased the likelihood for device isolation, but did not solve the problem entirely. There were two reasons for the difficulty in achieving good isolation.

The first challenge concerns the nature of the InAs heterostructure itself, in that a series of devices that are well isolated at 4.2 K may not show such isolation at room temperature. Moreover, this lack of isolation can persist down to 77 K. Parallel conduction must provide this strange behavior, which may be related to the fact that these InAs quantum wells have relatively high carrier densities (10^{12} cm^{-2}) even without doping. (We point out that leakage problems of electrical gates for InAs/AlSb heterostructures are discussed in the literature [54].) Effective calibration of isolation etches was thus possible only by testing devices at 4.2 K. This isolation difficulty was not so evident in wet-etched devices. In that case, simple etching of the InAs with the acetic acid solution normally yielded good

isolation. Why the dry etches seemed to be less effective at turning the InAs off is unclear and was not investigated further, once a successful recipe using SiO_2 and longer etch times was achieved.

The second challenge results from the use of PMMA as an etch mask. Measurements of transfer resistance devices showed that even when all PMMA was apparently removed in the desired regions and the ion milling proceeded as intended, device isolation was irreproducible. This problem was solved by using SiO_2 as the etch mask and etching for 6 minutes. Measurements on transfer resistance devices then showed good isolation ($\gtrsim$ 1MΩ) at 4.2 K (although not necessarily at 77K).

For SiO_2-masked devices, only small areas needed to be protected for the isolation etch, since the previous deposition of SiO_2 (for the contact etch) already covered the device in all areas but the contacts. ECR etch times were again found to be slightly variable, and a dc self-bias of 100 V was found to remove the InAs, and the layers just beneath it, more reliably than a 50 V bias. Etching times of approximately 3:30 minutes resulted in smooth etches that went past the InAs layer. Often one side of the chip would be etched slightly faster than the other, perhaps due to irregularities in the ion flux, but this was easily fixed by briefly removing the chip, changing its orientation on the sample stage, and then etching again. Electrical characterization of both magnets and InAs after dry etching, both by ECR and ion mill, showed that performance was not significantly degraded due to properly executed etching.

3.4 Metal Interconnects, Wirebonding, and Chip Mounting

Device connections to ground pads were made with thermally evaporated Cr/Au lines (usually about 80 Å Cr and 1500 Å Au). For both PL and ebeam devices this step was straightforward. Before wirebonding, the chips were mounted in 28-pin chip carriers with either silver paint or superglue (silver paint was predominantly used because even though it would sometimes fail to hold the chips after a few cooldowns, superglue had the tendency to crack the samples when cooled, unless very little of it was used). Chips mounted with silver paint were placed under a hair dryer for a few minutes to dry the paint. Wirebonding was usually done with 1 mil Al wire (1 % Si). At the beginning of the work, Au wire was used, but it was later found that unless adhesion of the Cr/Au pads was extremely good, the Au wire

had a tendency to lift off the pads. With practice, Al wirebonds could be made with high success rates and relatively quickly (one chip per half hour). After wirebonding, the chips were ready for measurement.

Chapter 4 Measurement of Photolithographically-Defined InAs Spin Devices

In this chapter we discuss our measurements of photolithographically defined (PL) devices [55]. These devices are large, with channel widths of 3 μm or 6 μm and lengths varying from 6 μm to 64 μm, reflecting a certain level of optimism regarding the potential size of spin-coupled phenomena, based on results from Johnson's Au spin devices. The measurements discussed here were made, for the most part, between late 1994 and late 1996. We discuss the different device geometries, followed by a description of the experimental setup and probe configurations. We then discuss results and possible interpretations for the large hysteretic signals measured in numerous devices. We conclude with a discussion of possible improvements, many of which were implemented in later ebeam devices.

4.1 Device Layout

Schematic diagrams of the four types of PL device geometries are shown in Figure 4.1. We implemented several device geometries in order to maximize the likelihood of detection of a spin-coupled signal. In (a), (b), and (c) the ferromagnets are curved in order to distance their edges from the conducting channel. This concern is a valid one, but was not well served by the curved magnets, as will be discussed later. In these devices the small magnet is 10 μm wide by 46 μm long (straight across from magnet corner to magnet corner) while the large magnet is 10 μm wide by 107 μm long. Different sizes were used in the hope that the shape anisotropy would result in different coercivities for the two magnets. In all but the first geometry, conducting channel widths of both 3 μm and 6 μm were fabricated. In (a) we display a 'type I' device, which features slightly larger contacts than other devices (4 x 8 μm^2 vs. 4 x 4 μm^2). More importantly, in this device type the InAs is not patterned into a thin channel, as in the other devices. That is, the entire semiconductor region between injector and detector is active, giving a large injection area (bad for spin signal strength), with the trade-off that device boundaries should not play an important role. There are four

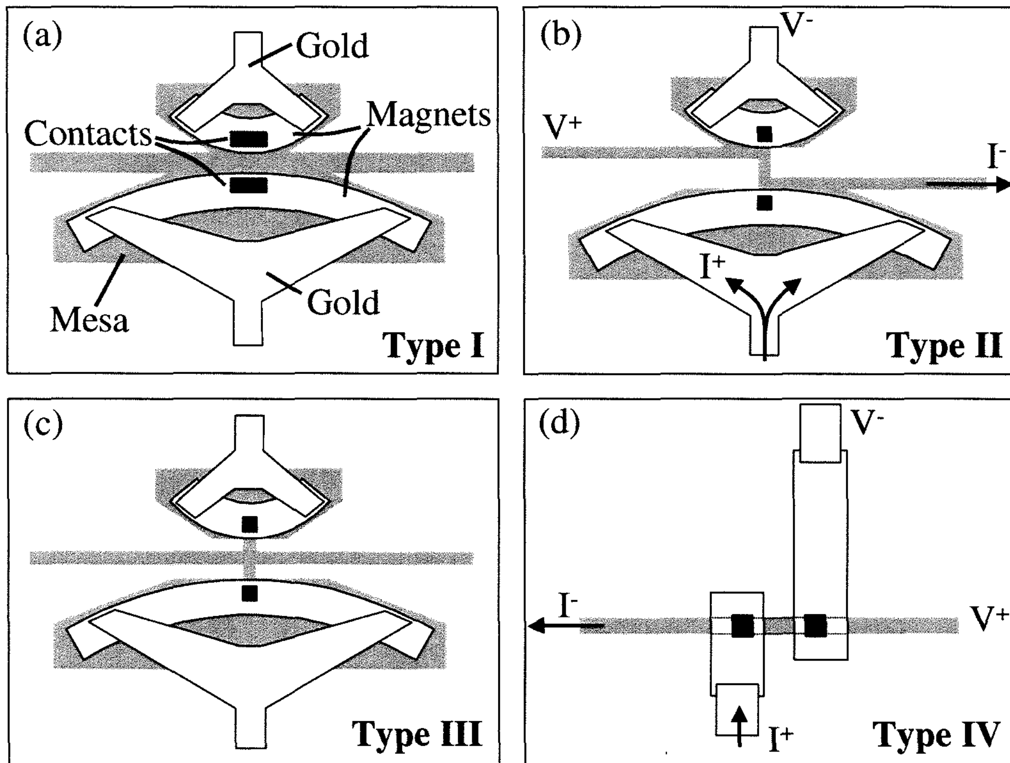

Figure 4.1: The four PL device geometries. The black regions denote InAs contacts, the gray areas show the active device areas, and the white areas are the ferromagnets and gold interconnects.

type I devices, with injector-detector separations, d, of 8, 16, 32, and 64 μm.

Type II devices, shown in (b), have 4 x 4 μm^2 contacts and a zig-zag channel. In these devices d varies from 10 to 128 μm. (The type II device with $w = 6$ μm and $d = 10$ μm is really more like a type I device and is referenced as such below.) These devices highlight the nonlocal character of the measurement. The type III devices of (c) are very similar to II but have a simple cross channel, as in the transfer resistance devices discussed in Appendix C. Type III contact separations vary from 11 to 128 μm. Finally the type IV devices in (d) are different in that the contacts are placed directly in the channel. This geometry is most similar to the Al metallic spin devices, with magnet dimensions of 10 x 20 μm^2 and 10 x 40 μm^2, and d varied from 6 to 64 μm.

Scanning electron micrographs of each type of device are shown in Figures 4.2-4.5. Many of these micrographs show early examples of devices, in order to highlight improvements made in processing. The (a) devices in Figures 4.2 and 4.5 are contrasted directly with

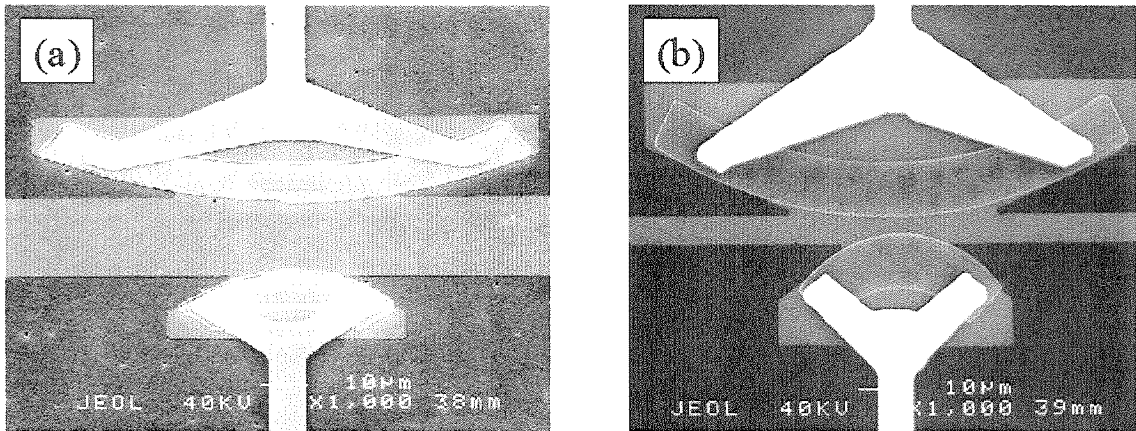

Figure 4.2: Micrographs of two type I devices. Improvements in processing are obvious in the device in (b). Note that the sputtered magnets in (a) have much rougher edges than the evaporated magnets in (b).

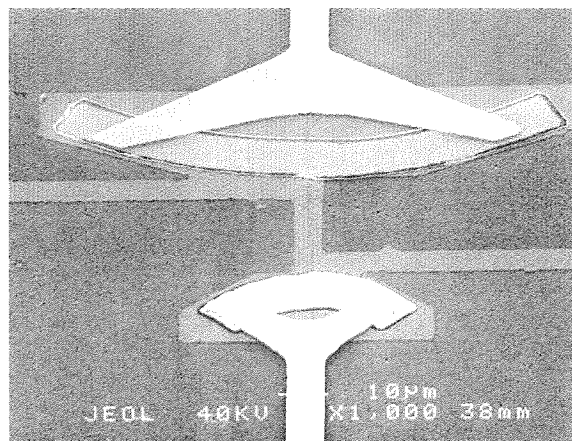

Figure 4.3: Micrograph of a type II device with sputtered contacts. Note here the difference in brightness between the two contacts, indicating that the smaller contact is composed only of Au (hence this device has only one ferromagnetic contact). This is a control device.

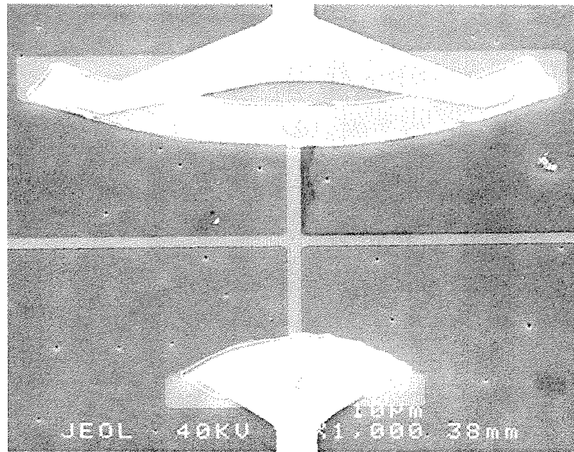

Figure 4.4: Micrograph of a type III device with sputtered contacts.

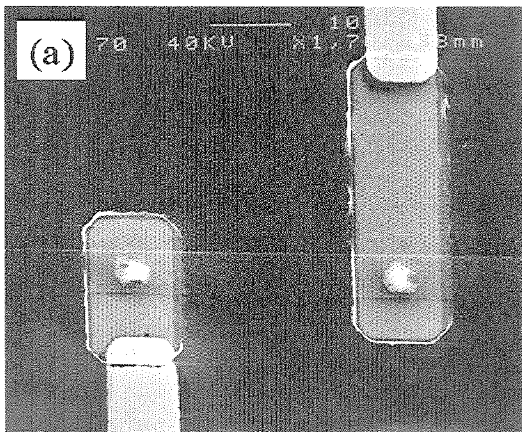

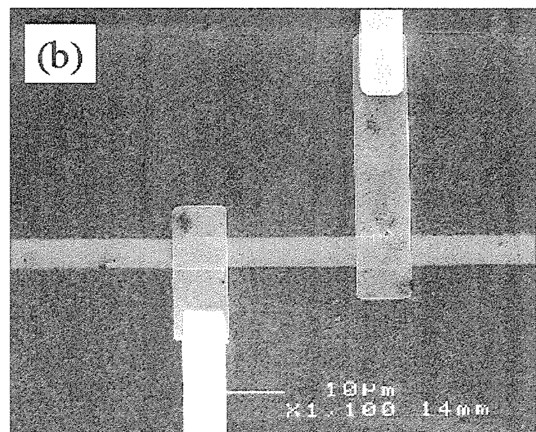

Figure 4.5: Again the contrast between earlier and later processing, in type IV devices. The device in (a) represents an early attempt to make GaAs spin devices, hence the bubbly (alloyed) contacts. The (b) device, an InAs device, is much cleaner.

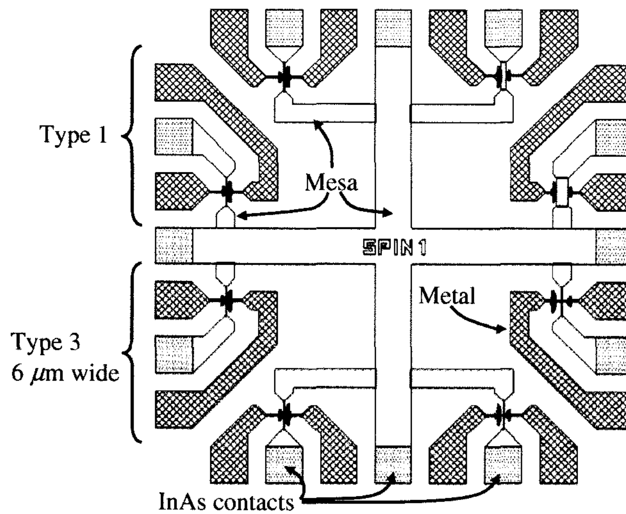

Figure 4.6: The layout of the first spin chip, with type I and III devices (6 μm wide channels). Type I contact separations are 8, 16, 32, and 64 μm, while for type III they are 11, 16, 32, and 64 μm.

later devices in (b). Note that contact windows in these devices, as in the device of Figure 4.4, have obviously rounded edges. This detail, though perhaps not very significant, was improved upon in later devices. The device shown in Figure 4.3 is a control device: only one of the contacts is made from a ferromagnet. Note that the ferromagnetic contacts in the devices discussed here were sputtered, often contributing to ragged edges in liftoff that are not apparent in the pictures of later test devices which were fabricated with a mix of photolithography and ebeam lithography (evaporated contacts were fully implemented in the ebeam devices of Chapter 6).

Eight devices fit onto one 28-pin chip (although there are 4 leads per device, one ground was shared). The overall chip layouts are shown in Figures 4.6-4.9. In each case the types of devices are noted and the channel widths and contact separations given. Although we fabricated each type of device at least a few times, as experiments progressed some devices were measured more frequently because they yielded more interesting results. In particular, the second spin chip (with the highest separation devices) was rarely made, but is included for completeness.

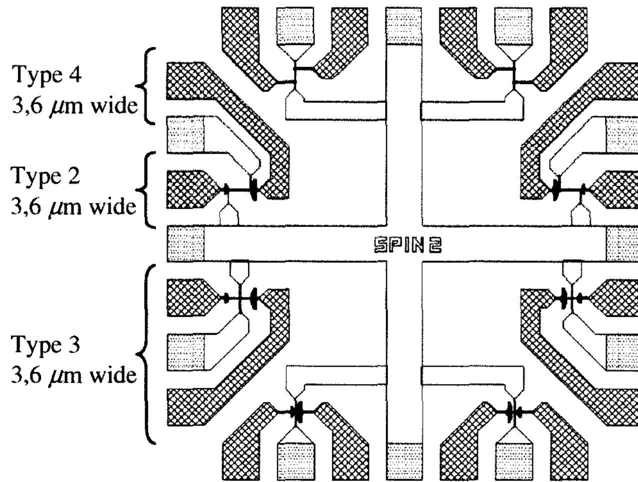

Figure 4.7: The layout of the second spin chip, with type II (3 and 6 μm $\times$ 128 μm), type III (3 μm $\times$ 128 μm and 6 μm $\times$ 6, 16, and 32 μm), and type IV devices (3 and 6 μm $\times$ 64 μm).

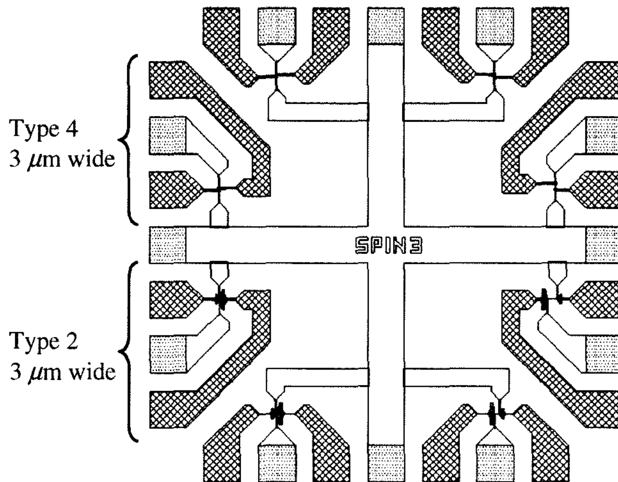

Figure 4.8: The layout of the third spin chip, with type II and IV devices, all with 3 μm wide channels. Type II separations are 10, 16, 32, and 64 μm and type IV separations are 6, 10, 16, and 32 μm.

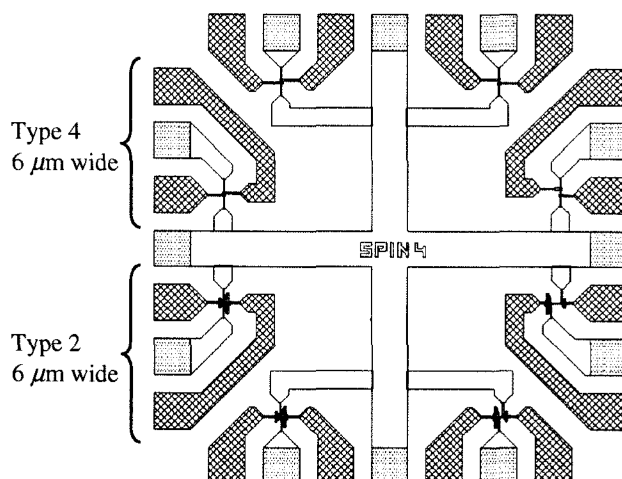

Figure 4.9: The layout of the fourth spin chip, again with type II and IV devices, with 6 μm channels widths. The type II separations are 10, 16, 32, and 64 μm and the type IV separations are 6, 10, 16, and 32 μm.

4.2 Measurement Setup

Measurements of spin devices were made exclusively at 4.2 K. Chips were mounted into a chip carrier inside a leak-tight brass can attached to a stainless steel tube (a 'dipper') for insertion into the helium bath. Connections to the chip carrier were provided via wires running up the inside of the dipper to connectors at its top. These connectors were then wired to a patch panel on our equipment rack. Current was sent to a device by taking the sine wave voltage output of a signal generator, usually at a frequency of 14 Hz, and feeding it into an opto-isolator, mounted in an electrically isolated panel, powered by ± 18 V batteries. The basic electronics setup is shown in Figure 4.10. The voltage waveform at the output of the opto-isolator was thus reference to battery ground, in order to minimize noise from fluctuations in the line ground. This voltage was then applied across the series combination of a ballast resistor of 100 kΩ or 1 MΩ, the device (through the patch panel), and a fixed 10 Ω resistor for current sampling. Since device resistances were usually less than a few thousand ohms the ballast resistance effectively converted the voltage source to a constant (ac) current source. The voltage across the fixed resistor was sent to a differential preamplifier with a gain of 1000 and then to a lock-in amplifier referenced to the signal generator. By continuously monitoring this voltage with a computer we detected

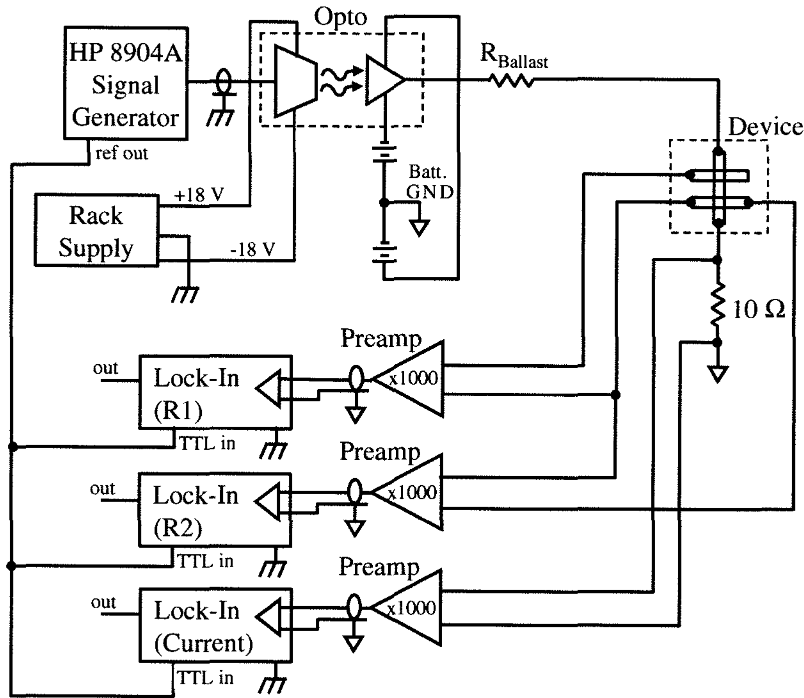

Figure 4.10: Schematic drawing of the measurement electronics, with the device shown, for pedagogical purposes, as a Hall bar.

any significant deviation in the r.m.s. value of the source current sent to the sample.

Magnetic field was varied by stepping the current sent from our computer-controlled magnet power supply to the superconducting solenoid in the liquid helium bath. Depending on the size of the step, a varying pause was inserted between the setting of a new field value and the measuring of voltage at the device. Although in principle the applied magnetic field could be measured directly from the output of a Hall probe mounted in our dipper, usually we simply trusted the output of the magnet power supply and corrected for any inductive lag (usually small) later during data analysis. In the beginning of this work we used a simple 8 T superconducting solenoid to provide the bias field. A significant improvement in our measurement ability was provided by the acquisition of a 3-axis superconducting magnet, consisting of one solenoid for the vertical, or perpendicular-to-sample, field and two split coils for the lateral, in-plane, fields. Each of these magnets could be operated alone, providing up to 1 T, or they could be operated together to provide a 1 T field in any direction. This enabled us, in our later work, to apply an in-plane field to saturate our

ferromagnets, and then to apply a perpendicular field to probe for Hanle phenomena.

Measured voltage was taken from the patch panel, through another 1000× differential preamplifier, and to another lock-in. In some cases a substantial background resistance made the measured voltage large enough that the lock-in was insensitive to smaller fluctuations. In these cases we nulled the lock-in input with a waveform of comparable size provided either by another signal generator, synchronized with the first, or by a voltage-divided component split off from the original waveform. The lock-in voltage was sampled by computer, after an appropriate pause (usually 1-2 s), at each new field value. By dividing out the source current our program then generated a listing of the sample resistances at each magnetic field. Enough lock-ins were available to allow measurement of 2 or 3 devices simultaneously, provided the chip design allowed it (as in the local Hall work discussed in the next Chapter). In the spin device measurements, however, we always measured one device at a time.

4.3 Probe Configuration

The importance of probe configuration was discussed somewhat in Chapter 2. In previous metallic Al devices, nonlocal detection of the spin-coupled signal was employed in order to minimize background resistance. As applied to our devices, this nonlocal scheme is depicted in Figures 4.1(b) and (d), where we show how voltage and current paths do not overlap in this method. We call this configuration the 'R_m' configuration, in reference to the nonlocal 'mutual' resistances that can contribute to the measurement of a nonzero voltage in this scheme. Note that with the other two device types there is no similar nonlocal configuration.

In the limit of diffusive transport, detection of a spin-coupled signal relies on the diffusion of the non-equilibrium spin population. We therefore expect the same size spin signal no matter how we arrange our leads, provided one of the two current leads is ferromagnetic, and one of the two voltage leads is ferromagnetic (although only the nonlocal, or R_m, configuration gives this signal without a conventional resistive background signal). The mean free path of electrons in our highest mobility devices is a few microns, so the PL devices described here are quasi-ballistic. Predictions for this regime are not clear so, in general, we attempted to measure the spin-coupled resistance R_s in more than one probe configuration. For instance, if we interchange the I^+ and V^- leads in Figure 4.1(b) or Figure 4.1(d) we have a crossed probe geometry which we call 'R_x.' With this setup we now have

more direct transfer of the current from one ferromagnetic contact to the other. However, we also have a background resistive drop which may need to be nulled out in order to maximize detectability of R_s. We can also arrange the leads, in all four device types, so that both current leads are ferromagnetic and thus both voltage leads are normal (or vice versa). In such a configuration, which we call simply the 'R' configuration, it is not apparent that the detector path (or injector path) is spin-sensitive, since one normally requires at least one ferromagnetic contact to act as a spin filter and provide a spin-coupled resistance. However, the ferromagnetic contacts still have a spin-dependent interfacial resistance and we cannot rule out a spin-coupled component in a measurement in the R configuration (although the magnitude of such a spin-coupled resistance in this configuration would likely be less than the R_s measured in one of the other configurations). To reiterate: in the remainder of this thesis we will refer to different probe configurations using the labels R_m, R_x, and R—these are *not* resistances, just configuration labels. The results of spin-transport measurements will usually, except in R_m measurements, have a background resistance, in addition to the actual spin-coupled resistance (or 'transresistance') R_s.

4.4 Measurement Results

A total of 20 chips, labeled IA1 through IA20, were measured using basic photolithography. Two sets of controls were made within this set: IA7 and IA8 had only normal contacts while IA9 and IA10 had one NiFe contact and one normal contact. In addition, for IA11 through IA16 the large ferromagnet was NiFe and the small ferromagnet was Co, in an attempt to more substantially separate the coercivities of the two contacts. Two heterostructures were used, both with densities of about $n_s = 1.8 \times 10^{12}$ cm^{-2}, but with different mobilities: $\mu = 5.6 \times 10^5$ cm^2/Vs and 1.6×10^5 cm^2/Vs. We used the higher mobility structure for chips IA1 through IA12, and IA17 and IA19; the lower mobility structure was used for the other 6 chips. In the discussion below a device is high mobility unless otherwise specified. All devices did not always work at 4.2 K, either due to contact problems or channel problems (depletion, undercutting, or faulty masking), but about 2/3 of devices were operational at least electrically (meaning that current could be sent through each of their contacts, and this current was linear with applied voltage). Of the 20 chips, some kind of magnetic field-dependent feature was seen On 15, usually in several devices on each chip. This includes both

hysteretic features, which are interesting for this work, and 'zero-field' features (meaning non-hysteretic features centered around zero magnetic field), which were not investigated further but will be described briefly below.

4.4.1 Zero-Field Features

We divide the zero-field features into two classes: those observed while ramping an in-plane magnetic field, and those observed with a perpendicular field. We start by describing the in-plane zero-field feature, which we denote ZF1. We observed this feature in all types of early devices, with probe configurations as described in the caption of Figure 4.11, in each case at contact separations of up to 32 μm. The type III devices, however, seemed to exhibit this feature most often. The polarity and structure (peak, dip, double peak, double dip, etc.) of ZF1 was somewhat variable. The feature was not present in later processing rounds, in part because we then concentrated on type II and IV devices, but there may also be some dependence of ZF1 on contact details—ZF1 was never observed in ebeam devices with evaporated contacts. Examples of ZF1 traces for each device type are shown in Figure 4.11. Note that the field scale of the features is tens of Oe. In no case was any hysteresis present in ZF1 traces and, moreover, the feature was seen in devices with only one ferromagnet and in devices with no ferromagnets. At times the details of a given ZF1 trace seemed to be sensitive to probe configuration, but in any case the signals were repeatable. Since this feature apparently has no relevance to spin injection, we did not investigate it further. Finally we note that in Figure 4.11, especially (a) and (d), the background signals are not flat but, either due to some small perpendicular field component, or due to idiosyncrasies in the devices themselves, they have slope and sometimes curvature. These magnetoresistive backgrounds (that is, any background that varies with applied field) were more bothersome when looking at perpendicular field sweeps.

The importance of perpendicular field sweeps, in connection with the Hanle effect, was explained in Chapter 2. As mentioned there, the Hanle effect, which relies on spin precession, is an important check on the validity of a spin-coupled signal. In several cases we attempted to find a Hanle signal, but this was complicated by the magnetoresistive behavior of the low density 2DEG subjected to the strong magnetic field. Two types of magnetoresistive behaviors in ballistic or quasi-ballistic devices are well known: transfer resistance phenomena [52], and boundary scattering phenomena [56]. The first of these

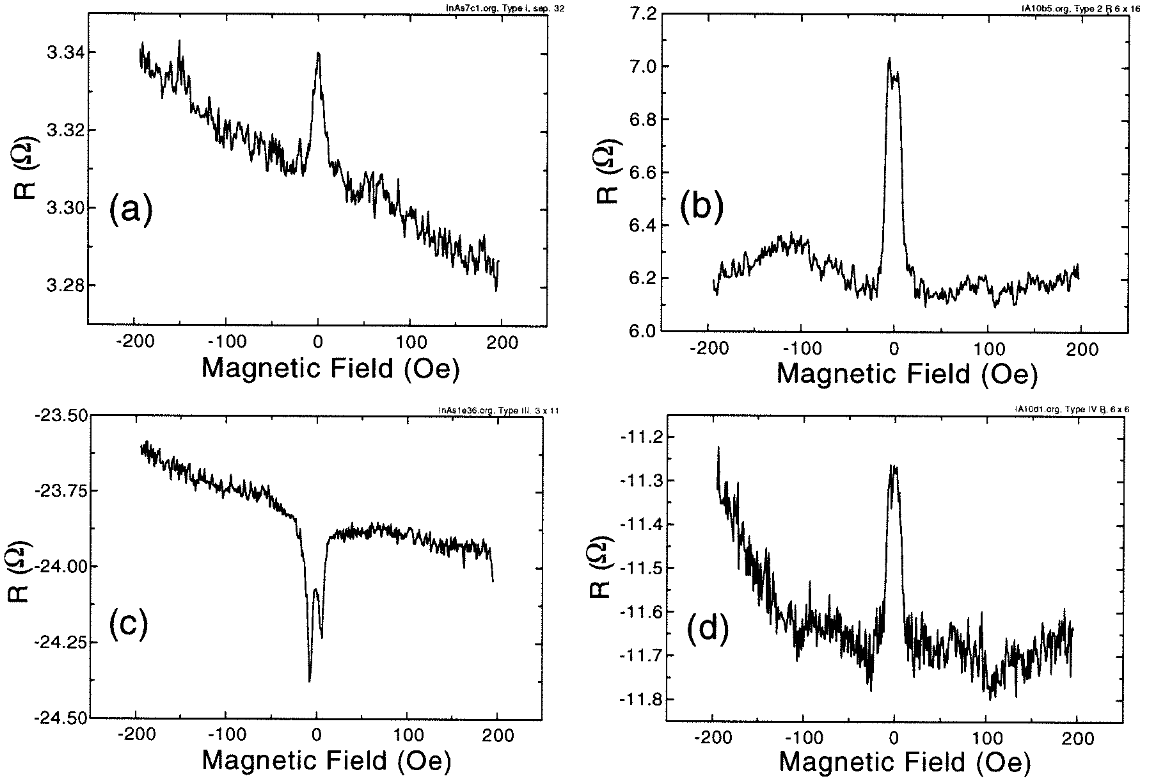

Figure 4.11: Data showing the ZF1 feature from each of the four device types: (a) type I with $d = 32$ μm; (b) type II, R_x config., $w = 6$ μm, $d = 16$ μm; (c) type III, $w = 3$ μm, $d = 11$ μm; (d) type IV, R_m config., $w = 6$ μm, $d = 6$ μm. The (a) device had two normal contacts, the (b) and (d) devices had one NiFe contact, and the (c) device had two NiFe contacts.

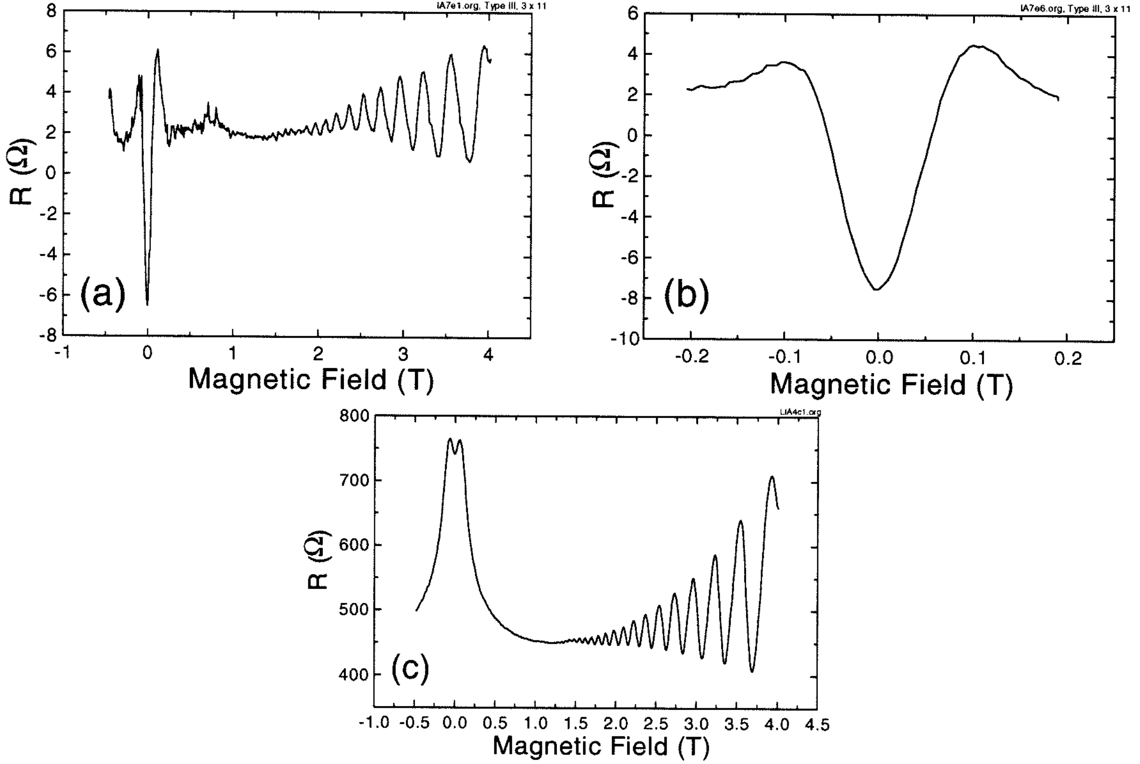

Figure 4.12: Examples of known magnetoresistive phenomena. The traces in (a) and (b) are for the same type III device with 3 μm channel width; they illustrate the relevant field scales of the transfer resistance phenomena. The trace in (c) is a 4-terminal resistance measurement of a wet etched InAs channel nominally 3 μm wide. In both (a) and (c) the high-field Shubnikov de-Haas oscillations are present.

is explained in Appendix C and occurs strongly in cross-junctions. The second, whose manifestation reflects the interplay between bulk and sidewall scattering, occurs in simple 4-terminal measurements. Examples of these are shown in Figure 4.12. The field scale of the transfer resistance is about 1000 Oe, whereas for the boundary scattering phenomenon it is closer to 2500 Oe. These figures are shown in order to illustrate that we should not be surprised by the presence of large magnetoresistive backgrounds in our devices when varying perpendicular magnetic field.

To elucidate the variety of magnetoresistive backgrounds present in our devices, we show examples in Figure 4.13. Note that in (d) and (e) the same device is measured with different probe configuration, changing the background significantly. These traces will not be analyzed further, but are included to highlight the difficulty in attempting to observe the Hanle phenomenon. Ideally we would like to be able to subtract away such backgrounds

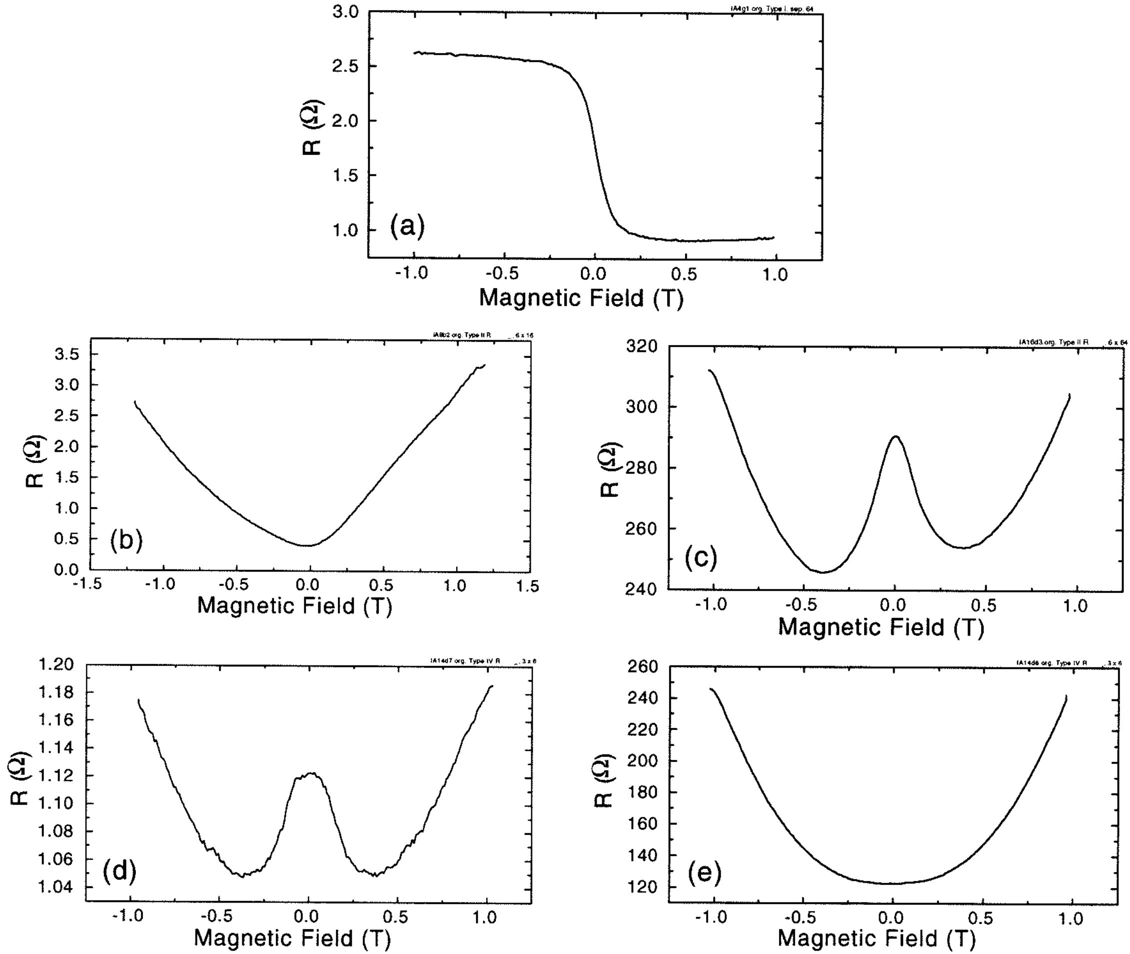

Figure 4.13: Five example magnetoresistive backgrounds found in InAs PL devices, in perpendicular magnetic field. The device in (a) is type I with $d = 64$ μm. In (b) the device is type II, R_m config., $w = 6$ μm, $d = 16$ μm; and in (c) type II, R_x config., $w = 6$ μm, $d = 64$ μm. The same type IV device with $w = 3$ μm, $d = 6$ μm is shown in the R_m config. in (d) and in the R_x config. in (e). In addition the devices in (c), (d) and (e) are made from the lower mobility InAs structure.

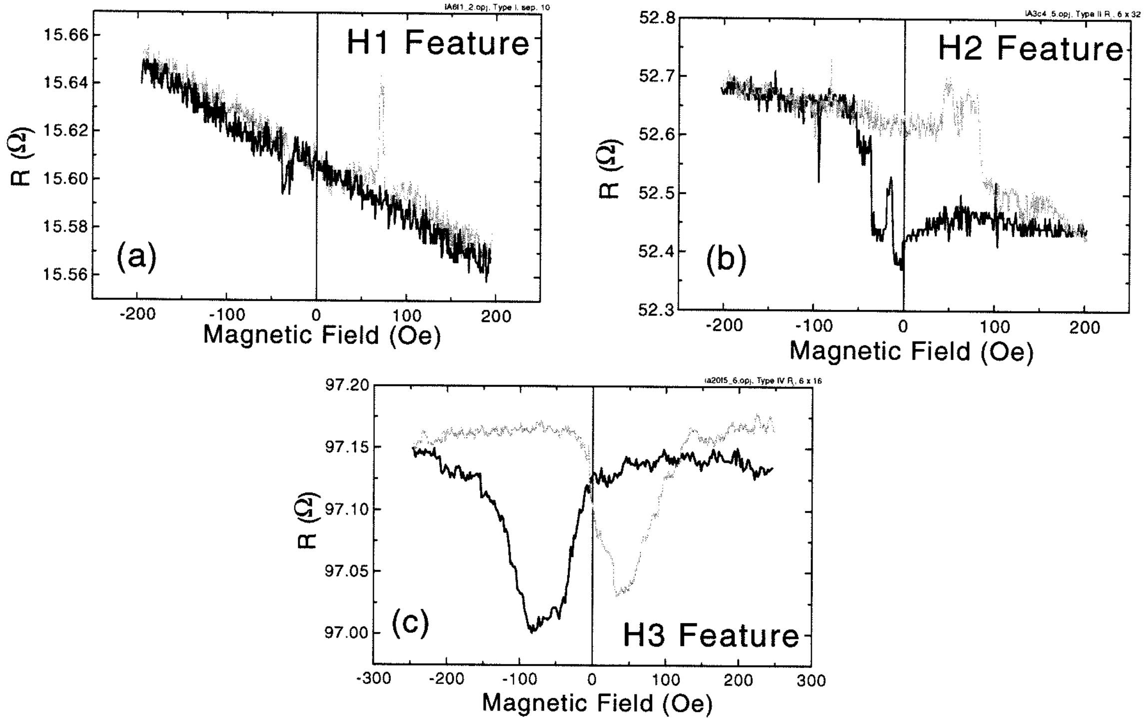

Figure 4.14: The three basic hysteretic signals observed in InAs PL devices, in parallel magnetic field. The dark traces are sweeping down, the light sweeping up. In (a) we show an 'H1' feature for a type I device with $d = 10\ \mu$m; in (b) an 'H2' feature for a type II device, R_x config., with $w = 6\ \mu$m and $d = 32\ \mu$m; and in (c) an 'H3' feature for a type IV device, R_x config., $w = 6\ \mu$m, $d = 16\ \mu$m.

and see if any spin-coupled signal is present. To do this, however, we would need to know in detail what background to expect. This information can be obtained in such quasi-ballistic systems by computer modeling (see Appendix C).

4.4.2 Hysteretic Features

We detected three basic hysteretic signals through the course of our measurement of PL devices, on many different chips. As one would expect, no hysteretic phenomena were observed in the devices with two normal contacts. Also, no hysteretic feature was ever detected in a type III device. Examples of the three hysteretic signals are shown in Figure 4.14. In the first example, which we call H1, we observe a dip and peak, each about 10 Oe wide, on either side of zero field (the background slope exhibited in Figure 4.14(a) is incidental, the result of a Hall component of resistance probably stemming from misalignment of the chip in the superconducting solenoid). At times this type of feature was observed instead

in the form of two dips or two peaks as well: the defining feature of H1 we take to be the fact that the up and down sweeps have the same zero-field value, with narrow hysteretic features on either side of zero field. The case of two zero-field states is shown in (b), where there are step-like transitions on either side of zero field. We call this feature H2. Finally in (c) we display a hysteretic signal, dubbed H3, that features two broad dips. This signal, most prevalent in type IV devices, could be two peaks as well, but was never a dip and a peak and is distinguished from H1 by its broadness: the transitions commence before zero field is reached in each sweep direction. The H1 and H2 signals were often intermingled to some degree in different devices. Below we discuss each of the device types I, II, and IV in turn.

Type I Devices

Both H1 and H2 features were present in type I devices up to $d = 16\ \mu$m. The most tantalizing signals, because they agree with the qualitative expectations for spin-coupled transport in the polarize/analyze geometry, are those of type H1 with two dips or two peaks—the polarity can be changed just by switching a pair of leads, so we are concerned more with whether the features are both up or both down. Examples of this kind of data are shown in Figure 4.15 for a device with $d = 10\ \mu$m. Current was, as usual, sent through one of the ferromagnets while voltage was measured at the other ferromagnet, but in type I devices since there is no channel definition, the measurement is not completely nonlocal (that is, the R_m and R_x configurations are the same). Features in trace (a) are wider than in the H1 example given above, but they are much sharper than what we call H3, and seem to start switching just after zero field. The trace in (a) is very tantalizing, so we investigated it further. One property that a polarize/analyze signal should have is that if one stops sweeping just after the first ferromagnetic transition (at which point the voltage switches from, say, a higher to a lower level) and then starts sweeping the other way, back to zero, the voltage state should not switch back up until the first ferromagnetic transition is reached on the other side of zero. We call this the 'memory' effect because it displays two zero field voltage states, like a nonvolatile memory element. Traces (b) and (c) in Figure 4.15 show our attempts to probe the memory effect in the same device as in (a), on both sides of zero field. We see that at zero field we do indeed have two states, although the transitions are not as sharp, or as 'square,' as we would like. Although attempts at verifying

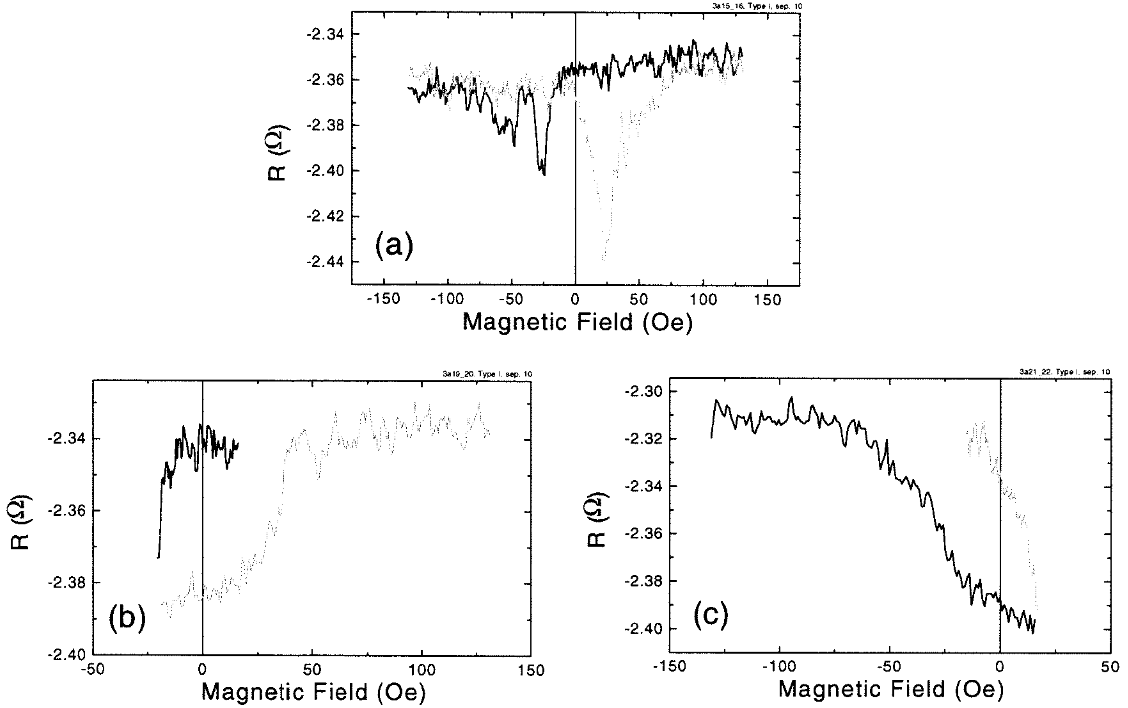

Figure 4.15: Plots of the H1 feature from one of our type I devices, with $d = 10\ \mu$m. Again, the dark traces are sweeping down in field and the light traces are sweeping up.

this signal with the Hanle effect were unsuccessful, such data are possible evidence for spin injection.

We found that the type of signal observed could be entirely dependent on probe configuration, and at times sensitive to measurement technique. We show this in Figure 4.16. In (a) is a plot from the same device that produced the data of Figure 4.15 but with current flowing straight through the InAs channel and voltage measured between the two ferromagnetic contacts. In this R configuration (which is loosely similar to a Hall geometry where voltage is measured transverse to current flow) there is no spin selection of the injected electrons. Any hysteretic phenomenon must then result either from some residual interaction between the current and the spin-sensitive interfaces underneath F1 and F2 (this interaction we expect to be very small, except perhaps in type IV devices where the ferromagnets are not spatially separated from the main current path) or from magnetoelectronic interactions not based on spin transport. The observed waveform is a mix of H1 and H2 traces, and is substantially different from the plot in Figure 4.15(a). In Figure 4.16(b) and (c) we show data from the same type I device, in the same R_m probe configuration each

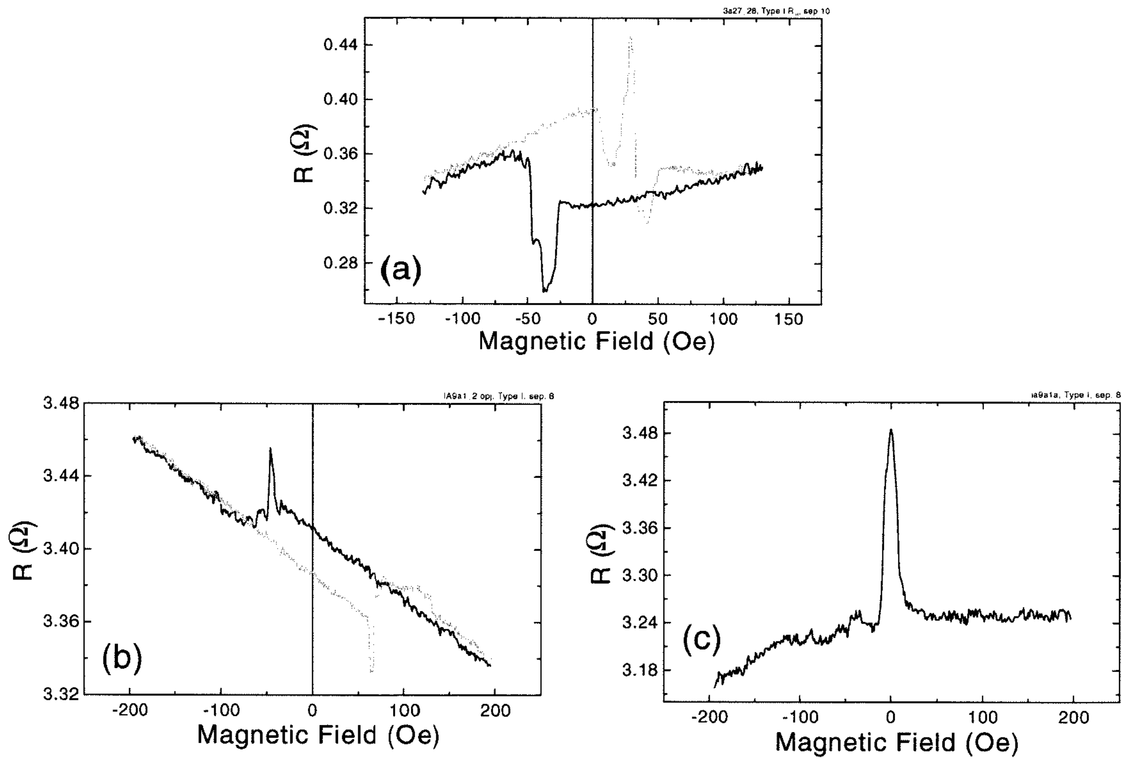

Figure 4.16: An example of the probe configuration dependence of measured phenomena in type I devices. In (a) is the same device as in the previous figure, but in a Hall geometry. In (b) and (c) we show data from a type I device with $d = 8$ μm in the R_m config.

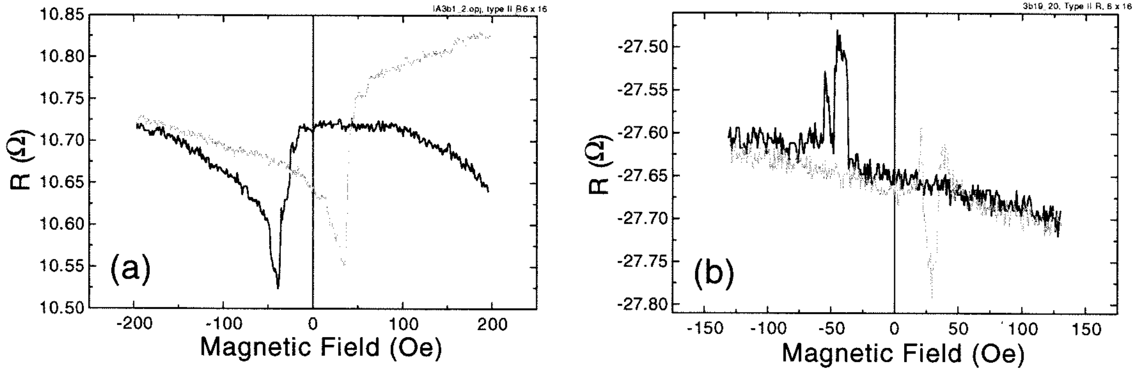

Figure 4.17: An example of the probe configuration dependence of hysteretic features in a type II device. Both plots are from a device with $w = 6$ μm and $d = 16$ μm but (a) is in the R_x config. and (b) is in the R config.

time. Here there was nominally no difference in the measurements, yet in (b) we see an H1/H2 signature and in (c) we see ZF1. Between these two acquisitions we changed some of our circuit connections (a different preamp, and we measured other devices), none of which should have damaged the device, but it is possible that some static discharge altered the details of the conduction path. Except for this case, the presence or absence of different features in our devices was reproducible within a given cooldown.

To summarize results from type I devices, we saw hysteretic features in several devices and at times these features were suggestive of spin-coupled transport. However, the lack of such phenomena in different probe configurations, combined with the inability to verify such signals by inducing spin precession via an external perpendicular field (i.e. the absence of the Hanle effect), make it impossible to prove the case for spin injection in these devices.

Type II Devices

Type II devices yielded the greatest amount of hysteretic data, in the largest number of devices, up to $d = 64$ μm. As with type I devices, the appearance of these features was dependent on probe configuration. In Figure 4.17 we show an example of this for a device with $w = 6$ μm, $d = 16$ μm. In (a) the R_x scheme was used and the result is a double dip H1 trace, with perhaps a slight broadness reminiscent of H3. This is again a tantalizing piece of data. In (b) the current was sent straight through the InAs channel (not through either ferromagnet) and voltage was detected between the ferromagnets—the R configuration (which, in this device geometry, means a mix between a Hall resistance, and a 4-terminal

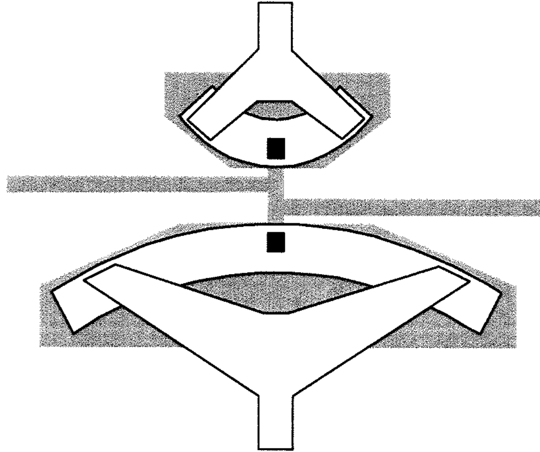

Figure 4.18: The modified type II device geometry. The device is a mix of the geometries shown in Figures 4.1(b) and (c).

longitudinal resistance measurement). The injected current in (b) is thus not spin-filtered and, once again, must be the result either of a residual interaction between the current and the spin-sensitive interfaces underneath F1 and F2 or of non spin transport based magnetoelectronic phenomena. The magnitude of the hysteretic features in (b) is similar to that found in (a), casting some doubt on the validity of a spin-based interpretation of the (a) trace. The case for spin transport is further weakened when we note that no hysteretic signal was observable when measuring in the R_m configuration. The mean free path for electrons in these devices is a few microns, so at 16 μm we should be significantly diffusive. This lack of a hysteretic signal in the R_m configuration was cause for concern because a diffusive spin signal should surely be present in either R_m or R_x schemes. In fact, hysteretic features were very rarely present in any device in the R_m configuration.

Having seen evidence for non-spin-based magnetoelectronic phenomena in numerous type II devices we implemented a slight design change in our lithography masks. Referring to Figure 4.1, we see that the InAs channel runs along each ferromagnet, leaving open the possibility of interaction between fringe magnetic fields and the electrons in the low density semiconductor. In an attempt to lessen any potential interaction we separated the channel from the magnet by 2 μm (except in the case of the smallest type II device, with $w = 3$ μm and $d = 10$ μm, where the channel-magnet separation was limited to 1 μm). This makes the devices, shown in 4.18 and dubbed type 'IImod,' somewhat similar to the type III devices, where no hysteretic phenomena were seen.

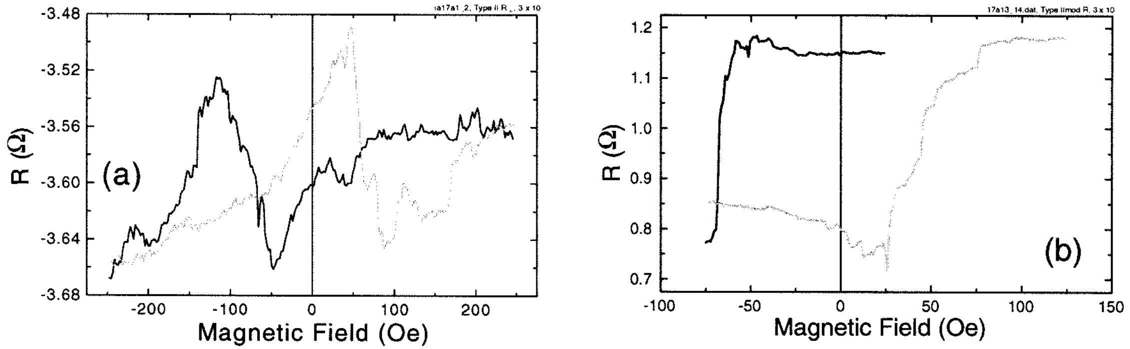

Figure 4.19: The one example of hysteresis in a type II (mod or not) device in the R_m probe configuration, in (a). The pronounced hysteresis in (b) is for the same device in the R config. The device here is type IImod with $w = 3$ μm and $d = 10$ μm.

Despite this modification, which was implemented on chips IA17 through IA20, hysteretic features were still commonly observed. Once again, these phenomena are ambiguous evidence of spin transport phenomena, since they depend on probe configuration in unexpected ways. Examples of hysteresis in type IImod devices is seen in Figures 4.19, 4.20, and 4.21. In Figure 4.19(a) we show the only example of hysteretic phenomena in an R_m configuration (type II or IImod). The trace in this case is somewhat ugly, but looks similar to H3. In (b) the same device, measured in the R configuration, displays a very strong memory effect. Since we expect residual spin transport effects to be small in a type IImod device measured in the R configuration, the hysteresis in (b) indicates that, at least with 1 μm channel-magnet spacing, magnetoelectronic phenomena not based on spin transport are still strong in type IImod devices.

As shown in Figure 4.20, hysteretic features could also be observed in devices made with one Co magnet, or devices made from the low mobility InAs, and in devices with separations of 64 μm. In (a), for a NiFe/Co device with $w = 6$ μm and $d = 16$ μm, we see an H2 feature spread out over a larger field scale, probably due to the fact that Co has a larger coercivity (thus implying that the Co magnet, and not the NiFe magnet, is setting the field scale). This device was fabricated from the lower mobility InAs. In (b) we display another H2 trace from a type IImod device with $w = 6$ μm and $d = 64$ μm. Both (a) and (b) traces were taken in the R_x geometry. A spin-coupled signal should decrease as contact separation increases and spin relaxation becomes more prevalent. A magnetoelectronic effect in the R_x geometry would not decrease however, since only the channel-magnet spacing should

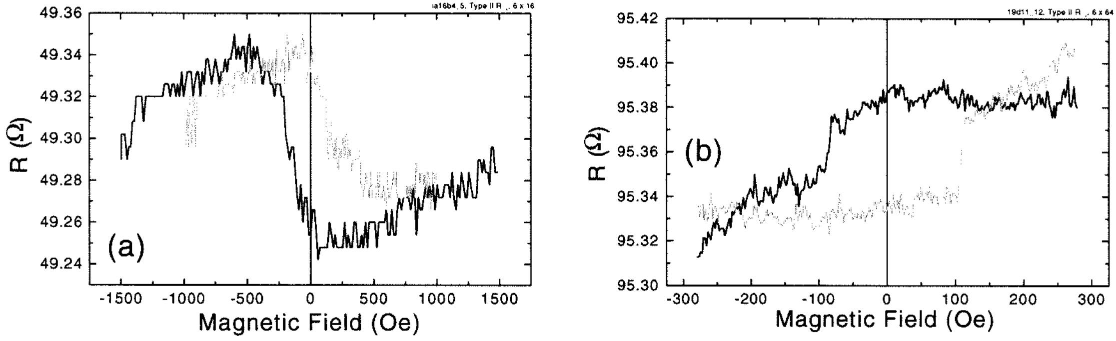

Figure 4.20: More examples of hysteresis in type II devices. The (a) device here has $w = 6$ μm and $d = 16$ μm and is made from the lower mobility InAs. In addition it has one NiFe and one Co magnet. The (b) device is high mobility type IImod with NiFe/NiFe magnets and $w = 6$ μm and $d = 64$ μm. Both traces result from the R_x config.

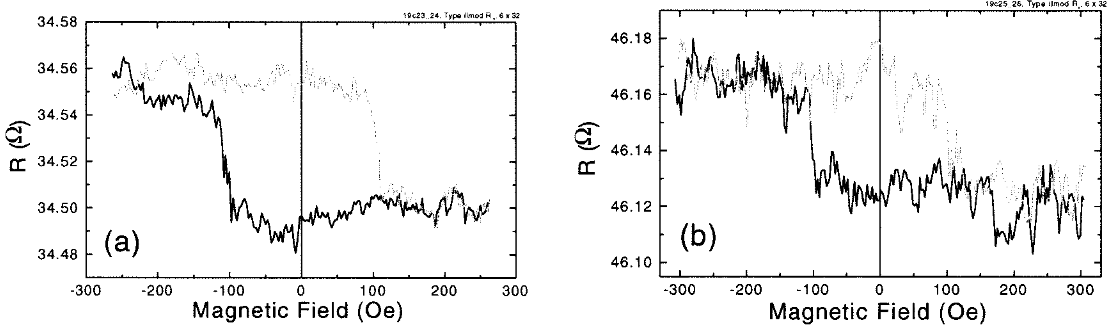

Figure 4.21: Temperature dependence of the R_x signal in a type IImod device with $w = 6$ μm and $d = 32$ μm: (a) is a measurement at 45 K and (b) is at 90 K.

matter. The (b) trace is thus another implication that our hysteretic phenomena have a strong non-spin component.

A final way we can investigate these hysteretic features is through their temperature dependence. Plots of R_x for a type IImod device with $w = 6$ μm and $d = 32$ μm at 45 K and 90 K are shown in Figure 4.21. The signal is still quite strong at 90 K, but higher temperatures were not achievable because the device isolation of the sample broke down. In the diffusive limit one expects that a spin-coupled signal should decrease in size as temperature is increased and both the momentum relaxation time and the spin relaxation time shorten. For ballistic electrons, subject to DP mechanisms, the picture is not as clear because a smaller momentum relaxation time could actually result in a longer spin relaxation time (however, raising the temperature also introduces spin scattering phenomena mediated by phonons). An empirical characterization of such competing mechanisms would

be interesting but would first require detection of an unambiguous spin signal. In any case, the point is moot because the device in Figure 4.21 has a contact separation of 32 μm, and should be well into the diffusive transport regime, especially at 90 K. We note, moreover, that certain magnetoelectronic phenomena not based on spin transport, such as the Hall effect, are relatively temperature insensitive, since the carrier density of 2DEGs is not a strong function of temperature.

We summarize the results from our type II devices simply by emphasizing the great variety of hysteretic phenomena observed. In some cases the form of these phenomena suggest spin-coupled transport, but there are numerous inconsistencies between signals obtained from different probe configurations, so that it is difficult to draw a clear conclusion. The pervasiveness, though, of these hysteretic features, whether spin-based or otherwise, is interesting, as they persist to both long separations and high temperature.

Type IV Devices

Type IV devices are significantly different in their geometry and this is reflected, to some extent, in the appearance of the hysteretic phenomena measured in them. Type IV devices did not yield hysteretic signals as frequently as type II devices, but this is likely due to the fact that they were less often functional. Perhaps due to the placement of the InAs contact windows directly in the channel, type IV devices failed more frequently, and even when they did work, often exhibited anomalous behavior in terms of their background resistance: devices with d = 32 μm did not necessarily have a 4-terminal resistance twice as big as a device with d = 16 μm, and the extrapolation of the resistances to zero separation did not yield zero resistance, likely due to problems with the contacts. Nevertheless, hysteretic phenomena were often observed. Device yield was later improved in ebeam spin devices patterned with SiO_2-masking and dry etching.

Probe configuration dependence of the observed hysteresis is shown in Figure 4.22 for two different devices with w = 6 μm and d = 32 μm. In all cases the hysteresis is of the type H3 variety. In (a) we display the one example of hysteresis in the R_m configuration. This should be compared with the (b) trace (R configuration), in which the current was sent through both of the ferromagnetic contacts, and voltage was detected across the channel. In this case neither voltage contact is a ferromagnetic spin filter. It is possible, however, that some spin-dependent signal may arise from the spin-dependent interfacial resistances

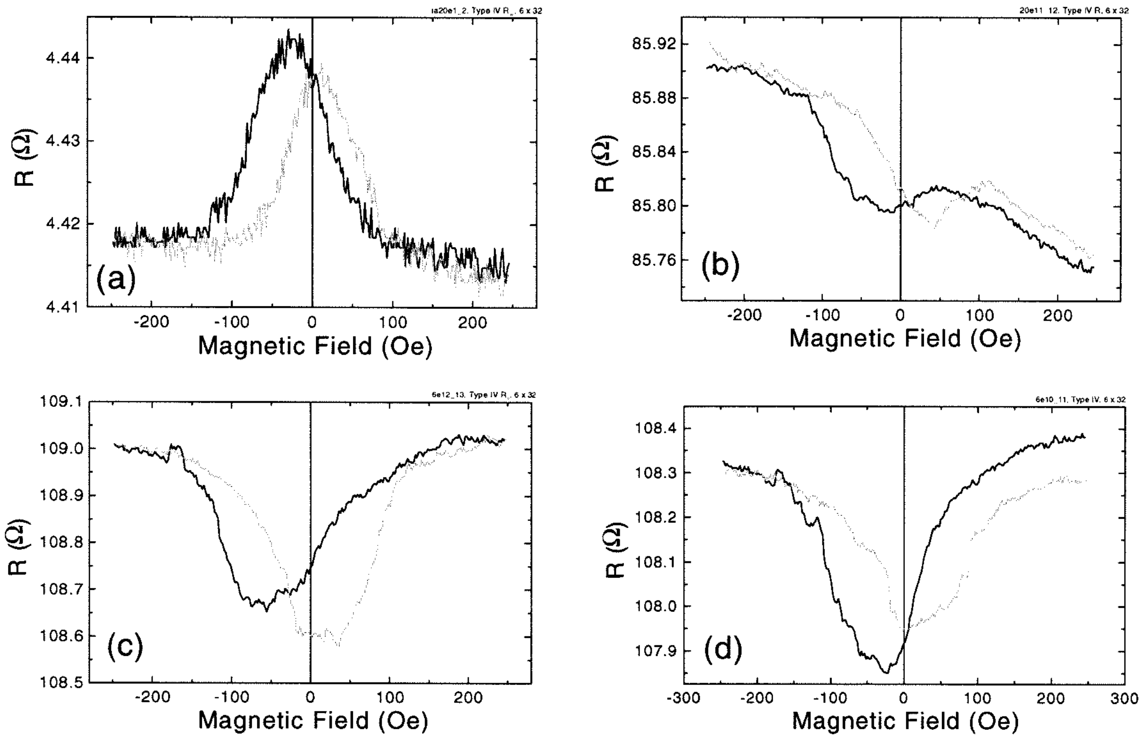

Figure 4.22: Type IV hysteretic phenomena. The device in (a) and (b), made from low mobility InAs, has $w = 6$ μm and $d = 32$ μm. The measurement is in the R_m config. in (a) and R in (b). In (c) and (d) the high mobility device has $w = 6$ μm and $d = 32$ μm as well. The measurement is in the R_x config. in (c) and R in (d).

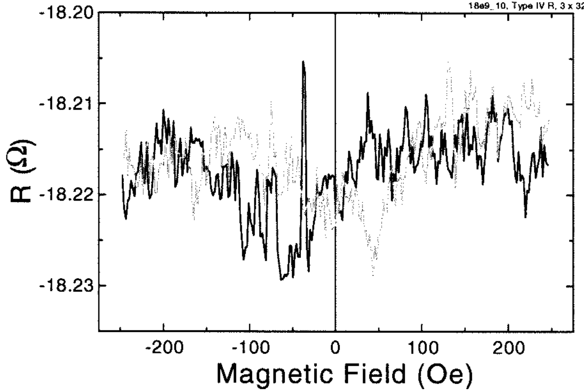

Figure 4.23: Data from another type IV device, fabricated from the low mobility InAs, with $w = 3$ μm and $d = 32$ μm.

underneath F1 and F2 (the current leads in this case). The magnitude of such a signal is unclear, but it is certain that if a spin-coupled signal is detected in the R configuration, it should also be detectable in R_x or R_m. We also point out that the R_x configuration in this device gave a plot very similar to that in (b). In (c) the signal, now from a different device, is from the R_x scheme, and in (d) the same device is probed in the R scheme. Finally we note that the offset in background observed in the right side of the trace in (d) was not uncommon. Possible inconsistencies in the contacts may have been the cause of this.

Hysteretic features were also observed, though not as often, at the narrower channel width of 3 μm, as depicted in Figure 4.23. (Type IV devices with 3 μm channel widths were often not functional.) Though difficult to qualify due to the small scale of the signal, this signal also appears to be H3. The difference between the hysteresis measured in type IV devices and that observed in types I and II is likely the result of different magnet shapes and placements. The shape of a hysteretic signal, whether it has its origins in spin injection or not, will be dependent on the switching characteristics of the ferromagnets. These characteristics are in turn dependent on magnet shape, as discussed in the next Chapter. Finally, we point out that hysteresis in type IV devices was observable from $d = 6$ μm to $d = 32$ μm, with apparently no attenuation at larger separations. This fact, and the lack of a hysteretic R_m signal in almost all of the devices, suggests again the prevalence of magnetoelectronic phenomena not based on spin transport.

Chip #	μ[a]	Device Types[b]	w (μm)	Contacts	ZF1?[c]	Hysteresis?[c]
1	high	I and III	3	2 NiFe	I16; III11	I8: H1,H2; I32: H2
3	high	II and IV	6	2 NiFe	I10	I10: H1,H2; II16,II32 :H1/H2; II64: H1
4	high	I and III	3	2 NiFe	III11,16,32	I16: H1
6	high	II and IV	6	2 NiFe	IV6,16,32	I10: H1; II16: H2 IV6,16,32: H3
7	high	I and III	3	2 Au	I8,32; III11,16	-
9	high	I and III	3	1 NiFe, 1 Au	I8,16; III11,32	I8: H2; I16: H1
10	high	II and IV	6	1 NiFe, 1 Au	I10; II16,32; IV6	-
11	high	II and IV	3	1 NiFe, 1 Co	—	II32: H2,H3; II64: H2
13	low	I and III	3	1 NiFe, 1 Co	—	I16: H2
14	low	II and IV	3	1 NiFe, 1 Co	—	I10: H1,H2; II16,32: H2
16	low	II and IV	6	1 NiFe, 1 Co	—	II16,32,64: H2
17	high	IImod and IV	3	2 NiFe	—	II10: H1,H2
18	low	IImod and IV	3	2 NiFe	—	II10: H2; IV32: H3
19	high	IImod and IV	6	2 NiFe	—	I10: H1,H2 II16,32: H1,H2; II64: H2
20	low	IImod and IV	6	2 NiFe	—	I10: H2; II32: H2 IV10,16,32 :H3

[a]'High' and 'Low' mobilities refer to $\mu = 5.8 \times 10^5$ cm^2/Vs and 1.6×10^5 cm^2/Vs, respectively.
[b]Type II and IImod devices with $w = 6$ μm are really type I devices and are referenced as such in categorizing the measured phenomena.
[c]The listings here are by roman numeral for device type, followed immediately by a number which is the contact separation d.

Table 4.1: A listing of the magnetic field-dependent features found in PL devices

4.5 Summary

A listing of the operational chips, their parameters, and the features observed in them is given in Table 4.1. In Chapter 2 we gave a list of requirements for detecting a spin-coupled signal, assuming an appropriately long spin relaxation length, and it is informative now to revisit that list. The first requirement, control over the switching properties and micromagnetic domain structure in the ferromagnetic contacts, was not directly addressed in our early PL devices. In the next chapter we show that better control of our ferromagnetic contacts is needed to maximize the possibility of observing a spin-coupled signal. The second requirement, control of the transport properties of narrow InAs 2DEG conduction channels, is not so problematical. Device isolation in PL devices was good and results of measurements of wet-etched transfer resistance devices (not discussed here) indicate preservation of high mobility and carrier density.

We were unable to verify whether the final requirement, control of the ferromagnet/InAs interface, was attained in our devices. Problems with anomalous backgrounds and irreproducibility of some traces may be evidence for such contact problems. In all the PL devices, ferromagnets were sputtered on InAs windows that had been exposed to air. This was improved in later ebeam devices. The fact that our photoresist developer etched the cap material was also a problem; this was also later solved by moving to ebeam lithography. In general, the diversity of the signals found in PL devices clearly indicated that better device designs, and more reliable processing conditions, were necessitated. Moreover, the large size of many of the signals led us to look for the origin of these magnetoelectronic phenomena, useful and interesting in their own right.

Chapter 5 The Local Hall Effect

The indications of magnetoelectronic phenomena not based on spin transport in our measurements of PL devices led us to the investigation of possible interactions between our ferromagnets and the conduction electrons in the InAs. One possible interaction results from the fringe magnetic field close to the edge of the ferromagnet. In NiFe ferromagnets this field can be of order 1 T near the ferromagnet, and it is reasonable to assume that such a field, though it dies off quickly away from the ferromagnet, can induce sizable local Hall voltages in the low density InAs. In this Chapter, we show that these local Hall voltages can indeed be large. We first discuss early work with photolithography and then move on to ebeam devices, which demonstrate not only that the local Hall effect (LHE) is a very sensitive probe of magnetization, but that it may have device potential as a simple nonvolatile memory element.

5.1 Early Devices

To probe the extent of interaction between local magnetic fields and the InAs we made some simple devices as shown in Figure 5.1. In these devices the ferromagnet is very similar to the large magnets in the PL spin device types I, II, and III, but it is not electrically connected to the conducting channel. Before the ferromagnet deposition the InAs is etched into a cross, or distorted cross as in Figure 5.1(b), with 3 μm channel width. The amount of offset, d, between legs in the distorted crosses is either 2 or 4 μm. This offset simulates the type II geometry of the PL devices. External magnetic field is applied in-plane, either parallel or perpendicular to the magnet's long axis, and voltage is measured transverse to the current flow. Typical source current levels were 1 to 10 μA.

Measurement results for both InAs and GaAs local Hall devices at $d = 2$ μm are displayed in Figure 5.2. In each device the NiFe magnet was 800 Å thick with a thin Au cap and was sputtered in the presence of a magnetic field along the magnet's long axis. The material in (a) is InAs, similar to the high mobility material used in the PL spin devices. The material in (b) and (c) is a GaAs 2DEG with $n_s = 1.5 \times 10^{11}$ cm^2 and $\mu = 10^6$ cm^2/Vs

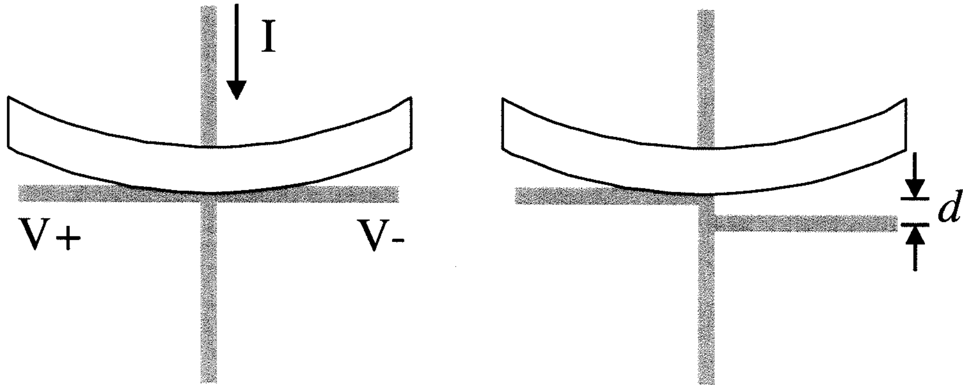

Figure 5.1: Drawings of simple devices for characterization of local Hall voltages.

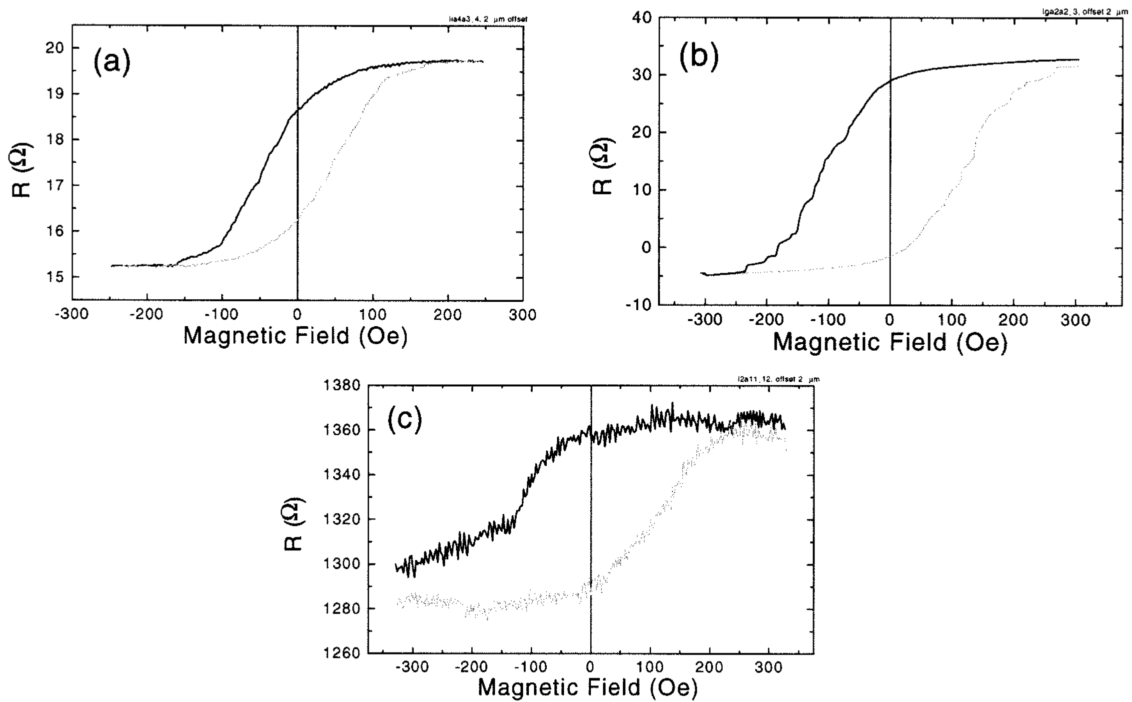

Figure 5.2: Data from early local Hall devices. InAs data in (a) and GaAs data in (b) and (c). (a) and (b) are at 4.2 K, and (c) is at 210 K. All are for $d = 2\ \mu$m.

at 4.2 K (no illumination), showing that the phenomenon is not peculiar to InAs. Hysteresis was also observed in plain crosses ($d = 0$ μm), but not appreciably for separation of 4 μm (though few good devices were measured at this separation). For the InAs device, external field was directed transverse to the magnet, while for the GaAs device the field was parallel to the magnet. The fact that the shape of the hysteresis loops is essentially the same in both cases implies that there is not a well defined easy axis of magnetization. Moreover, while the data in (a) and (b) are at 4.2 K the data in (c) are at 210 K. (We note that the data in (b) were obtained under LED illumination of the GaAs.)

To summarize, the data indicate strong local Hall phenomena for the magnet-channel geometry of our PL devices. The hysteresis loops indicate that the magnets switch gradually, over an interval of more than 100 Oe, which is not what we want for a spin device. Understanding the LHE was considered very important for the design of future spin devices because LHE signals vary when magnets switch just as spin-coupled signals do in the polarize/analyze geometry. Finally, we note that in (a) the full-scale variation of 4.5 Ω can be converted into a simple estimate of the magnitude of the average magnetic field in the InAs junction, at magnet saturation. The variation in resistance is $\Delta R = 2B_{avg}/n_s e$. For $n_s = 10^{12}$ cm^{-2} we obtain $B_{avg} = 36$ Oe. This is based on a cross geometry and homogeneous magnetic field, but nonetheless it gives some sense of scale; for an actual cross (rather than our distorted one) the average field would be larger. These early devices indicated that the LHE could be very large and, additionally, as one would expect, operative at high temperatures. More careful characterization of the field scale and decay was carried out in a next round of devices.

5.2 LHE Round 2

A second round of PL devices aimed at a more thorough measurement of the LHE were made on the same GaAs 2DEG structure discussed above. The results here are presented in detail in reference [57]. The basic shape of the device is shown in Figure 5.3(a), with a schematic view of the device and stray fields in (b). The magnet is 7×7 μm^2 and was deposited with one edge a distance s away from the center of a 3×5 μm^2 (lithographic size) cross. Magnets were thermally evaporated from a $Ni_{0.81}Fe_{0.19}$ source (sputtered NiFe was found to destroy the 2DEG), and were between 1000 and 1500 Å thick. Although

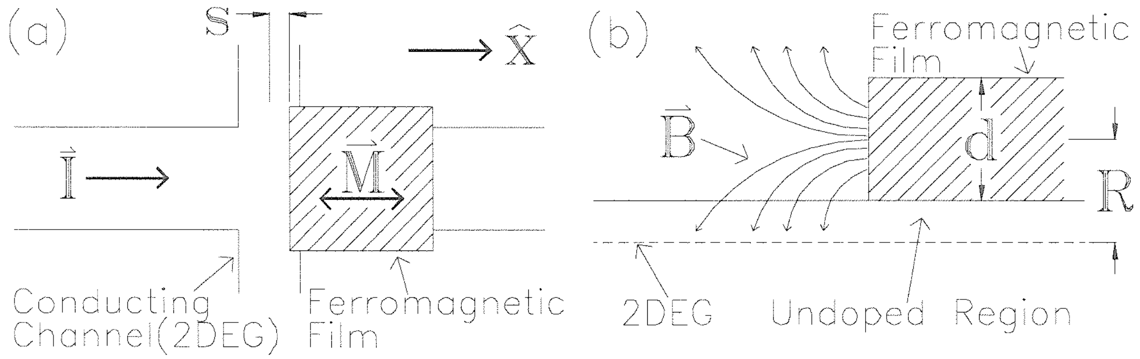

Figure 5.3: The layout (a) of 2nd generation LHE devices and a schematic representation (b) of the device cross section, with magnetic field profile.

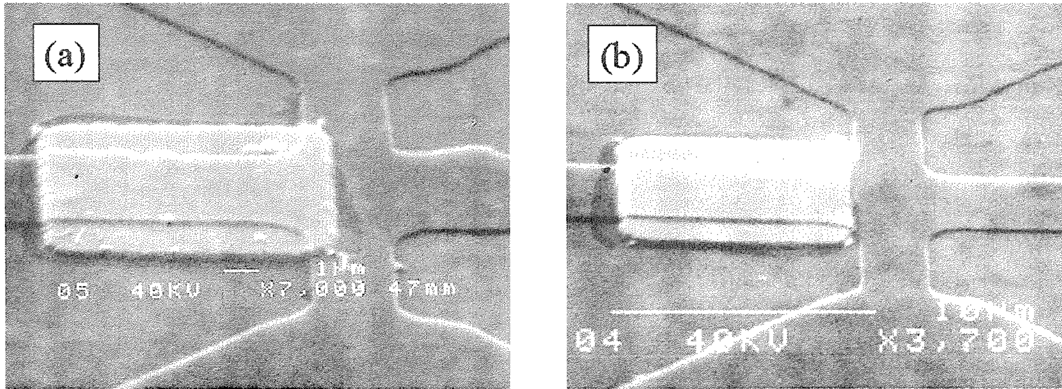

Figure 5.4: Micrographs of LHE devices. The (a) device has magnet offset $s = 0.5$ μm and the (b) device has $s = 1.2$ μm.

deposition by evaporation improved the raggedness of the liftoff edges it did not seem to improve squareness of the measured hysteresis loops.

5.2.1 Measurement Results

Images of devices are displayed in Figure 5.4. The Hall crosses were formed by wet etching in a solution of HF:HNO_3:H_2O_2:H_2O (1:1:1:10) for approximately 17 s. Ohmic contacts were formed, first, by depositing 430 Å Ge/$\sim$ 200 Å Ni /870 Å Au and then heating the sample in a homemade bell jar setup that could be pumped out and backfilled with N_2(85%)/H_2. Normally the alloying was performed at 450° C for 60 s, although a wider range of temperatures and times were also found to result in ohmic contacts. In a typical measurement run we swept an in-plane magnetic field over the range $\pm$400 Oe. Prior to each sweep a soak field of 500 Oe was applied to saturate the magnetization of the NiFe.

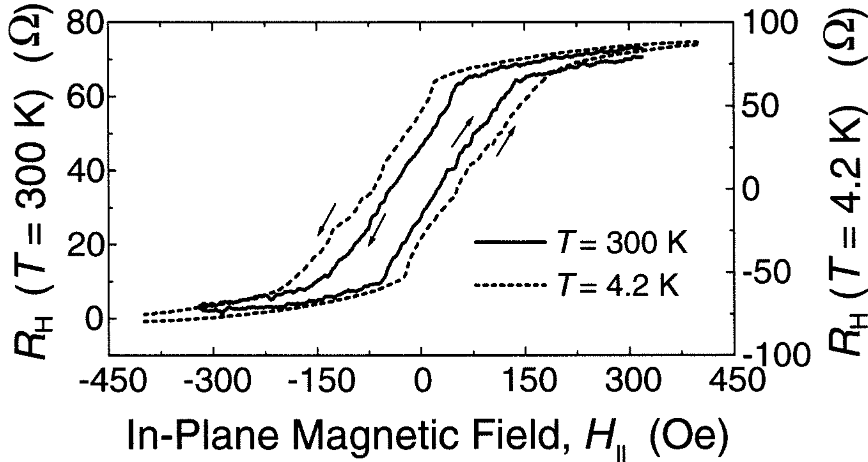

Figure 5.5: Data from a chip A device at 4.2 K (dashed) and 300 K (solid).

Current levels were between 0.3 and 1 μA and we measured Hall voltages at temperatures from 4.2 K to 300 K. In addition, the parameter s was varied from -1.5 μm to 6.5 μm to characterize the decay of induced local Hall voltage vs. distance away from the magnet.

We discuss representative data from devices on two chips, A and B, processed separately. Data for a typical device are shown in Figure 5.5. Note that at 4.2 K (the right axis) the data are nearly symmetric about $R_H = 0$ whereas at 300 K there is a substantial offset. This offset is due either to slight lithographic mismatch in the legs or to asymmetries in the electrical profile (depletion regions) of the Hall cross. At low temperature, when the mobility of the GaAs is high and therefore the sheet resistance, $R_\square = 1/(n_s e \mu) \approx 40\ \Omega$, is small, this asymmetry does not result in a large background resistance offset. At room temperature however, the sheet resistance is much larger ($R_\square \approx 3200\ \Omega$), so very careful control of junction definition would be necessary to tune the background offset. We note two further trends in the temperature dependence of the hysteresis loop. First, the loop is narrower at high temperature. From separate measurements of the magnetization **M** in larger, but otherwise identical films, we know this to be caused by decreasing NiFe coercivity with increasing temperature. Second, the overall magnitude of the Hall resistance change, ΔR_H, is smaller at high temperature. The saturation magnetization of NiFe changes only slightly with temperature between 4.2 K and 300 K, so we attribute the bulk of this temperature dependence to the carrier density increase in GaAs at higher temperatures.

In Figure 5.6 we show the dependence of ΔR_H on both magnet offset s and temperature. A negative value for s indicates that the ferromagnetic film F overlaps the center of the

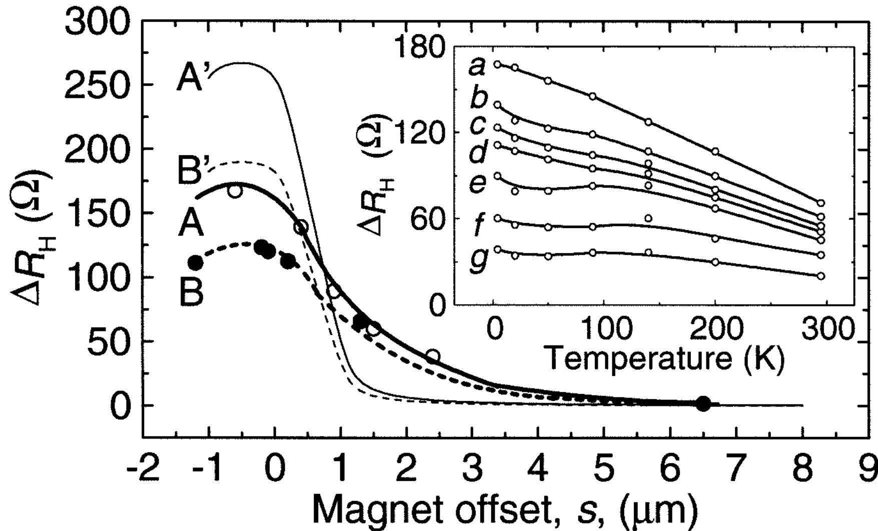

Figure 5.6: Measured dependence of ΔR_H on s for two chips A and B (A magnets were 50% thicker than B magnets). Theoretical results for the two samples are labeled A′ and B′ and chip B curves are dashed. *Inset*: temperature dependence of ΔR_H for devices with different values of s: (a) $s = -0.6$, (b) 0.4, (c) -1.2, (d) -0.2, (e) 0.9, (f) 1.5, (g) 2.4 μm. Curves (c) and (d) are from chip B devices, the rest from chip A.

cross junction whereas a positive value indicates that F is stepped back from the junction center. In each case s was measured by electron microscopy after fabrication. Both the peak in ΔR_H near $s = 0$ and the decay of ΔR_H over a couple microns are, qualitatively, as expected. Note that the point at $s = 6.5$ μm represents a control device: when the edge of F was removed far enough away from the Hall cross there was no local Hall voltage.

5.2.2 Analysis of the Dependence of ΔR_H on s

We can test our qualitative understanding of the LHE against the results of Figure 5.6 by making a simple estimate of the size of the perpendicular magnetic field, $B_\perp(\mathbf{r})$, in the cross junction, as in Ref. [58]. We start by assuming F to be comprised of a single magnetic domain with $\mathbf{M} = M_s\hat{x}$. The field outside the magnet can then be attributed to a magnetic surface charge density M_s (magnetic 'charge' per unit area) on the film's edge. The fringe field strength is then calculated at any point in the 2DEG by integrating field contributions from each element in this sheet of magnetization. Results for this computation are discussed below; here we further simplify the model in order to derive an analytical expression for the field profile. In this most basic approximation we collapse the sheet of magnetization

Chip	d	R	$B_\perp(x=0)$[a]	$B_\perp(x=0.1\ \mu\text{m})$	$B_\perp(x=1\ \mu\text{m})$	ΔR_H from model (expt.)
A	150 nm	152 nm	1650 Oe	1150 Oe	37 Oe	269 (171) Ω
B	105 nm	130 nm	1350 Oe	850 Oe	22 Oe	191 (128) Ω

[a] $B_\perp(x=0)$ is the maximum value for $B_\perp$ in the model, directly underneath the edge of F in the 2DEG.

Table 5.1: LHE chips A and B: Results from experiments and from the simple line charge model for the magnetic fringe field.

into an infinite line of charge at the edge of F, a distance $d/2$ above the GaAs surface (d is the thickness of F).[1] For this infinite line with magnetic charge density $\lambda_m = M_s d$ we have, in cylindrical coordinates, a radial magnetic field with magnitude $B_r(r) = 2\lambda_m/r$ (the origin $r = 0$ is defined along the line of charge). In the plane of the 2DEG this yields $B_\perp(x) = 2\lambda_m R/(x^2 + R^2)$, where now x is the lateral distance between the edge of F and the point r, and R is the depth of the 2DEG relative to the midpoint of F. The value of the saturation magnetization of our NiFe, measured on an independent film because it is known that evaporated NiFe films are Ni-poor [59], is $M_s \approx 838$ emu/cm^3. Other parameters, along with results for $B_\perp$ at different separations, and the predicted value for ΔR_H, are given in Table 5.1 (these data are not the theoretical results plotted in Figure 5.6, although they are similar).

In order to test our model against experiment we need to convert the calculated values for $B_\perp$ in the 2DEG into a Hall resistance. This is not necessarily straightforward because, in these LHE devices, the field $B_\perp(x)$ has a steep gradient $\partial B_\perp/\partial x$ on the scale of the electrical width w of the cross. As a rough approximation for ΔR_H in this inhomogeneous field we average $B_\perp(r)$ along x over a distance corresponding to the electrical width [60] of our junctions, estimated to be $w \approx 2.2\ \mu$m.[2] The full bipolar swing upon magnetization reversal is then $\Delta R_H = 2\langle B_\perp\rangle/n_s e$ where $\langle B_\perp\rangle$ is the averaged perpendicular field. Despite the assumptions of a magnetic line charge and the neglect of any nonuniform magnetization in F the predictions for ΔR_H are within a factor of two of experiment. This difference in magnitude is likely due to these assumptions, however: the magnet is almost surely not single domain, and in any case is less than a factor of two wider than the 2DEG channel,

[1] The assumption of an *infinite* line of charge is justified provided the width of F is significantly larger than the electrical width of the conduction channel. Here the two widths are 7 μm and just over 4 μm, respectively, and the justification is not immediately obvious, but we will proceed and then discuss the influence of our assumptions on the quantitative results.

[2] We account for the undercut of the mesa etch, $\sim 0.1 - 0.2\ \mu$m, and depletion at the channel edges, $\sim 0.3\ \mu$m.

so that edge effects can play an important role. More interesting than the discrepancy in ΔR_H is the finding that the model predicts a much faster decay of ΔR_H with increasing s than is found in the experiment. There are at least two explanations for this. The first, addressed below, is that our films are lithographically and/or magnetically rough, thus spreading the magnetization more dilutely over some volume back from the magnet's edge and resulting in a corresponding spreading out of ΔR_H. The second is that our averaging of the inhomogeneous magnetic field neglects possible equilibration, or electrical averaging, effects in the 2DEG. That is, since there is an inhomogeneous perpendicular field in the junction there can be inhomogeneous Hall voltages along the channel edge. But the 2DEG has a finite conductance that may not support this voltage drop along the channel edge, thus shorting out the inhomogeneity where it is greatest and redistributing charge so that the induced Hall voltage is decreased near the magnet's edge and increased farther away from it. Moreover, at low temperature our junctions are strongly ballistic, complicating the analysis of this correction. This was not pursued further in this work, but a more detailed analysis, which gives better agreement with the behavior of devices such as ours, is given in Ref. [61].

We can address the first issue from above relatively straightforwardly. Rather than assuming a magnetic line charge halfway up the film we distribute the charge evenly within F, up to a distance δ away from the film edge. Magnetic force microscopy performed on the edges of similar ferromagnetic films showed gradients, presumably due to closure domain structure, that decay on the scale of a few hundred nanometers. Roughness due to liftoff was also observed on this size scale. These are modeled by varying δ between 0.5 and 1.5 μm. Using this rectangular volume of magnetic charge we calculate $B_\perp(r)$ at each point in the 2DEG cross by integrating the field contributions from each differential element of magnetic charge in this volume. Averaging this in the same way as above we then arrive at ΔR_H. Results for this model are displayed in Figure 5.6 as solid A$'$ and dashed B$'$ traces for chips A and B, respectively. The value of n_s measured at 4.2 K is employed. Results from this model are not appreciably different from the results of the simple line charge model. We therefore conclude that the disparity between model and experiment in the slow decay of ΔR_H vs. s is due to the crude averaging we used to convert $B_\perp(r)$ into ΔR_H.

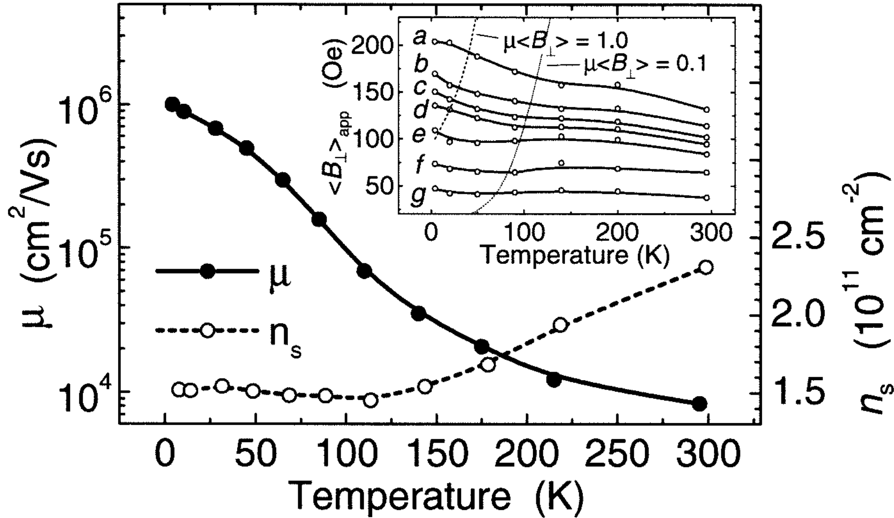

Figure 5.7: Carrier density n_s and mobility μ vs. temperature for our GaAs 2DEG (data from independent Hall bar measurements). *Inset*: the apparent field $\langle B_\perp \rangle_{app}$ extracted from ΔR_H by multiplying out $n_s e/2$ at each temperature.

5.2.3 Analysis of the temperature Dependence of ΔR_H

As mentioned previously, the temperature dependence of ΔR_H in the inset of Figure 5.6 does not stem from the magnetic properties of F. Separate measurements of $\mathbf{M}$ in larger, but otherwise identical, films confirmed that M_s was not temperature sensitive, decreasing by at most a few percent from 4.2 K to 300 K. Instead, an increase of n_s with increasing temperature, as shown in Figure 5.7, gives rise to a corresponding decrease in ΔR_H. To analyze this further we plot, in the inset of Figure 5.6, the apparent average field that generates R_H, $\langle B_\perp \rangle_{app} = \Delta R_H n_s e/2$, at each temperature.

If the temperature dependence of n_s were the only factor affecting the temperature dependence of ΔR_H, the plots of $\langle B_\perp \rangle_{app}$ vs. T would be flat lines, as is roughly the case for devices (e), (f), and (g). For devices with large $\langle B_\perp \rangle_{app}$ we see, however, that the lines are not flat, but rather have a pronounced negative slope, especially at low temperatures. We attribute this to a ballistic enhancement [62] of R_H at the higher values of $\langle B_\perp \rangle_{app}$ associated with small s. This enhancement occurs in cross-junctions where the cyclotron radius r_c of the electron orbits is on the same size scale, or smaller, than the electrical width of the channel. This gives us a characteristic field scale [63] $B_0 = p_F/ew$, where $p_F = \hbar\sqrt{2\pi n_s}$ is the Fermi momentum. In addition, the electron mean free path, $l_e = p_F \mu/e$, should be comparable with typical device dimensions: $l_e/w = \mu B_0 \approx 1$. In the plots of $\langle B_\perp \rangle_{app}$ vs.

T we show dotted contours signifying the regions where $\mu B_0 = 0.1$ and $\mu B_0 = 1$. These roughly demarcate the regimes where ballistic enhancement first sets in and then becomes fully developed.

5.2.4 Summary of PL LHE Devices

The large magnitude of the LHE, as demonstrated in these devices, was both interesting, as a possible memory device or field probe, and alarming, because it would likely swamp any potential spin-coupled signal in a spin device. The LHE devices here can be improved upon significantly, from the device perspective: the fact that one is controlling a ferromagnet's fringe field, which for NiFe is about 1 T at the magnet's surface, with a much smaller field determined by the magnet's coercivity means that the Hall resistance $R_H(\langle B_\perp \rangle_{app})$ can be much greater than that obtained in a standard Hall cross subject to a perpendicular field of the same magnitude as our parallel fields. In effect, these devices provide a magnetic field multiplication, although for our devices this is quite modest. At 300 K, the maximum Hall resistance obtained in our hybrid devices is $R_H(H_\parallel \approx 100$ Oe$) \approx 35\ \Omega$, whereas in a standard device with comparable perpendicular field we have $R_H(100$ Oe$) \approx 27\ \Omega$. We thus get a multiplication of only 1.3. This could be improved by using films with smaller coercivities and sharper hysteresis loops, and by using a semiconductor with a lower density conducting layer closer to the semiconductor surface.

Nevertheless, in light of their robust operation at room temperature, these LHE devices make interesting candidates as nonvolatile memory elements. One can envision switching the magnetizations of the ferromagnetic films with an on-chip write wire, eliminating the need for clumsy external biasing. In relation to our spin injection work, however, these devices, while providing proof that local Hall voltages are a serious issue, did not advance our need for better magnet performance. This goal was achieved in later work on ebeam LHE devices, discussed below.

5.3 LHE Devices with Nanoscale Ferromagnets

In later work with ebeam LHE devices we concentrated on characterizing the switching properties of different sizes of NiFe magnets. The work described here has been published elsewhere [64]. Similar work has also been discussed in Refs. [58] and [65]. Making the

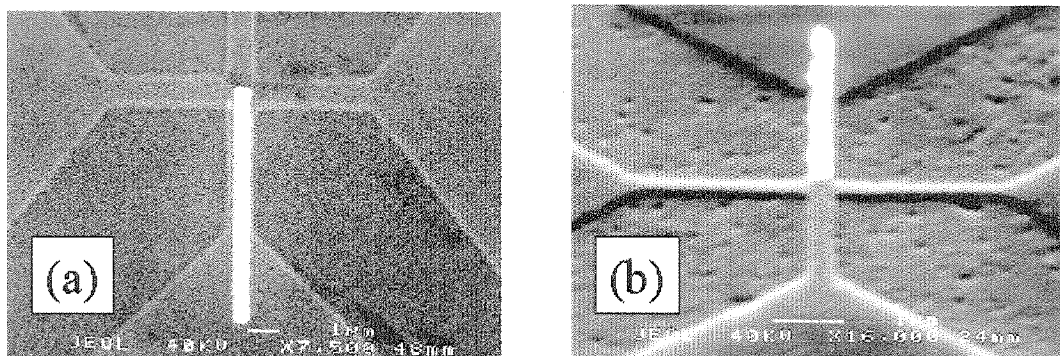

Figure 5.8: Micrographs of ebeam LHE devices with a 500 nm wide magnet in (a) and a 250 nm wide magnet in (b).

magnets smaller and more acicular (needlelike) in general gives better properties: squarer hysteresis loops with sharp coercive transitions and, in a given magnet, a remanent magnetization essentially equal to the saturation magnetization. In addition, the measurement of nanomagnets led us to calculate a surprisingly high ultimate sensitivity for local Hall devices as magnetic field probes.

5.3.1 Device Geometry

Ebeam devices differ from their PL counterparts in that the magnets do not spill over the edges of the Hall cross: the magnets are planar. Photos of two devices are shown in Figure 5.8. In most cases the ferromagnets were deposited by ebeam evaporation in the presence of a magnetic field (although this proved unnecessary for the smaller, narrower magnets). Sometimes a thin Ag underlayer, which seemed to promote adhesion, was deposited first. NiFe depositions were always followed by a thin Au deposition to prevent oxidation. As can be seen in (b) of Figure 5.8, liftoff did not always proceed smoothly. In later rounds of processing, however, good adhesion allowed us to briefly immerse our samples in an ultrasonic bath during liftoff. This often removed unwanted liftoff flags.

After deposition of the NiFe, a second layer of ebeam lithography defined the Hall cross. Early attempts at using PMMA as an etch mask were succeeded by SiO_2-masking, which was more reliable. Magnets as small as 75 nm wide could be fabricated with fairly good success. Some attempts at 50 nm widths, however, were relatively unsuccessful. Hall crosses

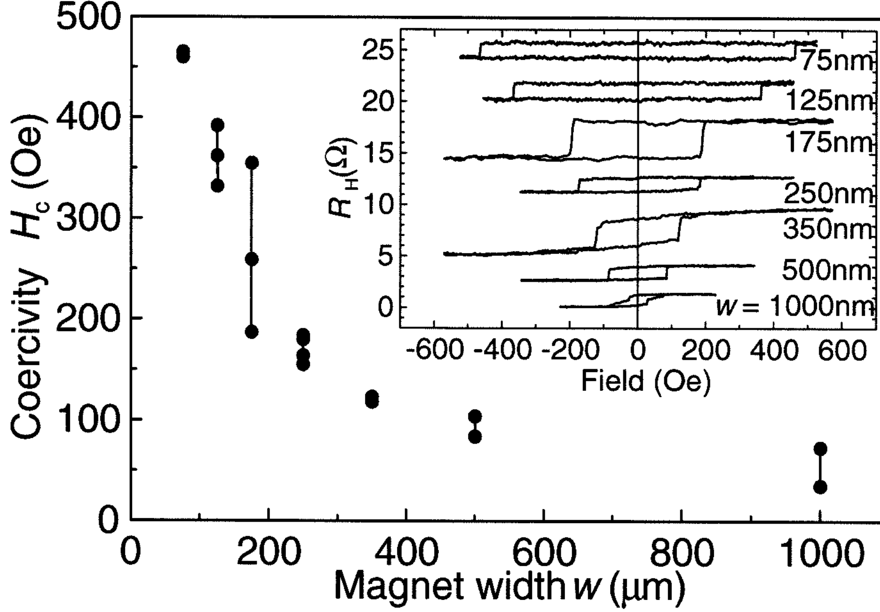

Figure 5.9: H_c vs. w for magnets with nominally the same deposition conditions and with aspect ratios of 10, at 300 K. Vertical lines connect data from magnets of the same width. *Inset*: Hysteresis loops for aspect ratio 10 magnets, again with varying widths. Traces are offset vertically.

were etched into 750 Å thick n+ GaAs on top of insulating GaAs by Ar ion milling at 500 V beam voltage for about 27 s. Carrier density of this material at room temperature was about 10^{18} cm^{-3}. Unless otherwise specified, all results discussed below are from room temperature measurements.

5.3.2 Measurement Results

Figure 5.9 shows typical data for a series of magnets of aspect ratio (AR) 10. Coercivity is defined as the amount of external field necessary to bring a particle's magnetization to zero, starting from saturation. Magnets having widths 500 nm or narrower almost always have sharp hysteresis loops at AR 10, with the apparent remanent magnetization, $M_r = M(H_{applied} = 0)$, equal to the saturation magnetization, M_s. We will address the question of whether such small magnets are single domain below; but in any case, the magnets in these measurements represent a great improvement over the magnets from PL spin devices or even over the magnets in the LHE devices discussed above. As with any local Hall device, the hysteresis loops, R_H vs. H, result from the magnetization at the end of the particle. Accordingly, we are sensitive to edge domains in this locale, but not to the detailed

micromagnetics within the entire particle. However, in a long thin magnetic particle with square or slightly rounded ends, magnetization reversal begins at the particle's ends and proceeds then toward the particle center [66][67]. Hence our sensitivity to edge domains and the nucleation of vortices can provide valuable insight into the switching dynamics of small ferromagnets.

Within a family of devices fabricated in the same processing run, H_c monotonically increased as magnet width decreased. This is in qualitative agreement with the expectation that, as magnetization rotates away from its easy axis, a thinner magnet has a larger magnetostatic energy barrier to overcome. However, as Figure 5.9 shows, H_c varied substantially for magnets of identical geometry patterned in different deposition runs, even though conditions were kept nominally identical. Possible sources of this sample-specific variation may include surface contaminants or edge roughness arising from irregular NiFe liftoff. The latter is a particularly salient issue; the engineering of systematic, tightly-controlled properties in nanomagnets may require exceedingly precise nanofabrication since geometric details on the scale of 10 nm may prove relevant in determining edge domain configuration [68].

We display results of another series of experiments, now varying aspect ratio instead of width, in Figure 5.10. In (a) we see that an aspect ratio of at least 5 is needed to obtain a relatively square loop for magnets of 500 nm width. In (b) the data for four 175 nm wide magnets (all patterned simultaneously on the same chip) show sharp transitions even at aspect ratio 2. We also see that H_c reaches a maximum near an aspect ratio of 5 and then decreases with increasing aspect ratio. Similar behavior has been previously reported for Ni and Co magnets[3] of width 100 nm and has been interpreted as evidence for a transition between coherent and incoherent switching dynamics[69][70]. Our larger data set suggests the experimental picture is more complicated: we find that magnets fabricated on different chips at different times need *not* show the same local maximum in H_c; this is demonstrated by the data of Figure 5.10(c) for 125 nm wide magnets. Again, this appears to indicate the crucial role that fine scale geometric details play in determining magnetization dynamics.

The temperature dependence of our magnets' coercive fields is reflected in Figure 5.11 in a comparison of results obtained at 300 K and 4.2 K. Both sets of data in the Figure

[3] A coherently switched magnet's coercivity should increase monotonically with increasing shape anisotropy. However, longer magnets must overcome a larger magnetostatic energy barrier when switching than short magnets. Thus at the same aspect ratio, longer magnets are more likely to switch by means of nucleation of vortices, decreasing the coercivity. Vortex states differ from essentially single domain states, such as the 'flower' state of Schabes [70], but the LHE may not be sensitive to the difference.

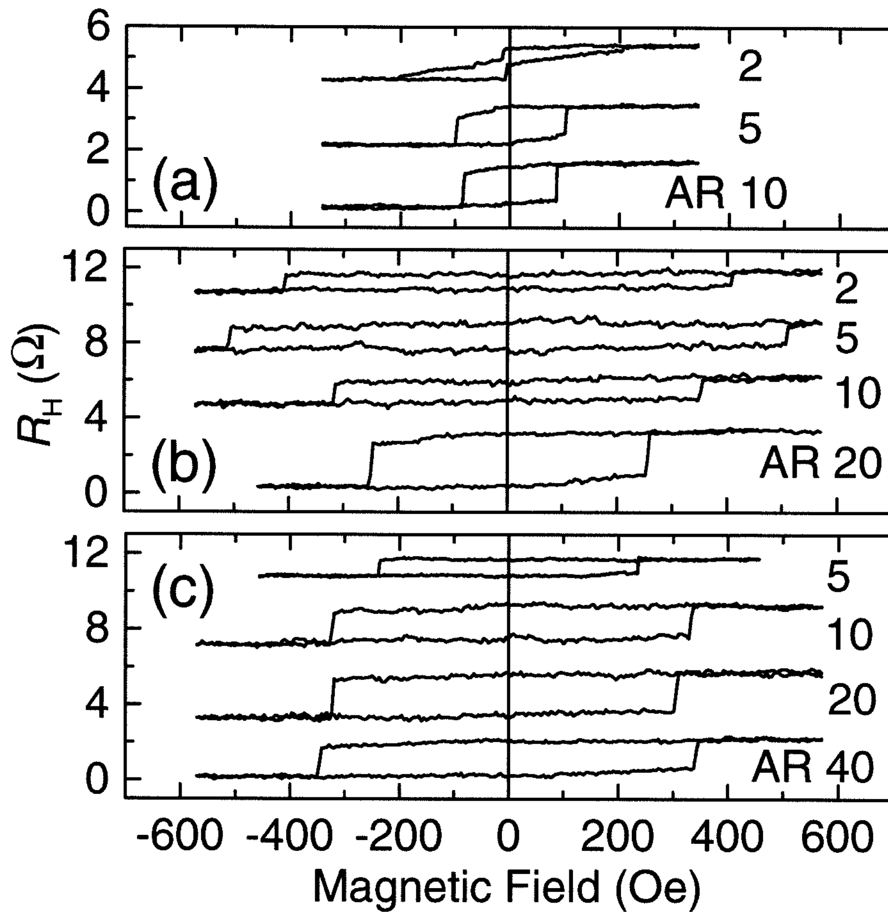

Figure 5.10: Hysteresis loops, at 300 K, for different aspect ratio (AR) magnets at the same width. Magnets in (a) are 500 nm wide, in (b) are 175 nm wide, and in (c) are 125 nm wide. Traces are offset vertically.

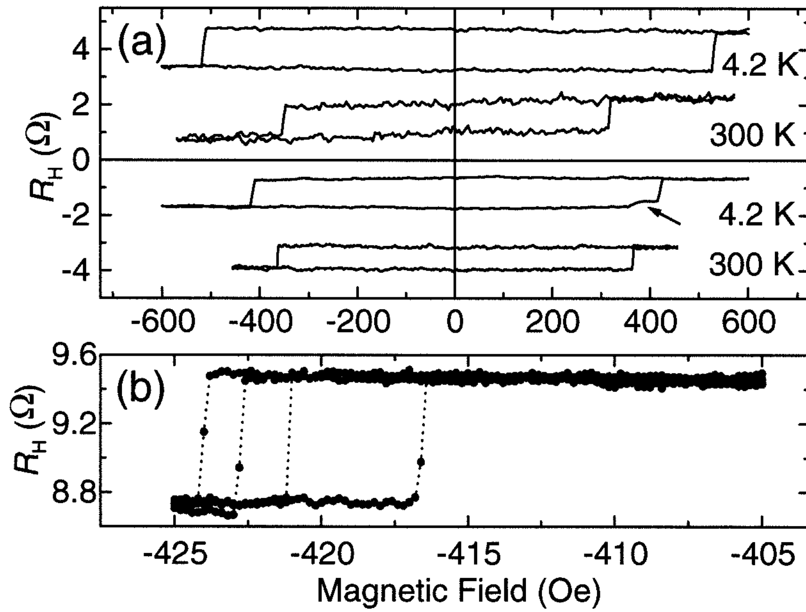

Figure 5.11: Hysteresis loops in (a) for 175 nm × 1.75 μm (top pair) and 125 nm × 5 μm (bottom pair) magnets. Despite the large AR of the 125 nm magnet, at 4.2 K it displays evidence for incoherent switching (indicated by the arrow). Hysteresis loops are offset vertically for clarity. (b) An enlargement of the transition region, at 4.2 K, of this 125 nm magnet, on the side that looks sharp in (a), shows that the transition occurs over a very narrow field range. Our field resolution was 0.1 Oe, and the sweep rate here was less than 0.2 Oe/s. Note the spread in coercivity which is evidence for the stochastic nature of the switching process. The vertical offset here was due to lithographic mismatch in the legs of the Hall cross.

(one for a 175 nm × 1.75 μm magnet and one for a 125 nm × 5 μm magnet) show the expected increase in H_c as temperature decreases. The 125 nm magnet also shows possible evidence of sequential switching of multiple domains on one side of the hysteresis loop at 4.2 K (the bump between 450 and 400 Oe), although no such indication is found at 300 K. Higher resolution traces in the region of the transition, obtained by decreasing the sweep rate from slightly greater than 2 Oe/s to less than 0.2 Oe/s, are shown in (b) of Figure 5.11. At this resolution the transition still looks very sharp. The points measured within the coercive transition (in 3 of the four traces in (b)) are most likely a measurement artifact relating to the finite lock-in time constant (usually 300 ms) used in sampling the points.

5.3.3 Single vs. Multidomain Magnets

Despite the square hysteresis loops of many of our nanomagnets, we generally expect that their magnetization reversal involves multiple domains. Within the literature there exist essentially two definitions of single domain behavior, static and dynamic [69][71]. The first is satisfied if all, or nearly all, of a particle's moments align with each other in zero applied field. It is important to note that, for magnetoelectronic devices that employ ferromagnets switched between static remanent states (like spin injection devices), this static criterion is most relevant—at least from the standpoint of quasi-static device characteristics. Magnets up to a few hundred nanometers in width and thickness can, operationally, satisfy this criterion[4] depending on the strength of their magnetocrystalline anisotropy (i.e., a larger uniaxial anisotropy allows single domain properties to be exhibited at a larger size scale in a monocrystalline sample, but for polycrystalline films this could actually be detrimental, as each grain attempts to align a different way). NiFe has a relatively small anisotropy constant[5] ($K \approx 1500$ ergs/cm^3 for 80% Ni [3]) so is a good choice when one wants shape anisotropy to dominate magnet energetics. Our work demonstrates that NiFe particles can have very square hysteretic behavior at widths of up to a few hundred nanometers. Other factors beside shape anisotropy, of course, assist in yielding square loops, such as deposition in an ambient field (which tends to directionally order the binary alloy), and a favorable

[4]The critical size for static single domain behavior is sometimes estimated to be approximately the thickness of a domain wall (about 100 nm in Ni or Fe). But apparently single domain behavior has been reported by several groups at larger sizes (see [69][70]) and indicates that for practical purposes one can go to several hundred nanometers in width and still have very square hysteresis loops, especially at 300 K.

[5]This decreases with decreasing Ni fraction until it passes through zero at 75% Ni.

exchange constant (which in NiFe is comparable to that in Ni, Fe, and Co). If a magnet is predominantly, but not strictly, single domain, the slight difference between the remanent and saturation magnetization may be virtually unresolvable.

The criterion of dynamic single domain behavior is much more stringent. It requires that moments within a magnetic particle align with each other even as the particle's magnetization reverses; i.e., all moments are required to coherently rotate with one another. This criterion, relevant for macroscopic quantum tunneling experiments, has been evaluated by fitting experimental switching data to the classical Néel-Brown theory of magnetization reversal. Measurements carried out at temperatures of a few hundred mK show that only particles with diameters of order 30 nm or smaller show such single domain dynamics [71]. The NiFe particles explored here are not in this regime. Despite the fact that at 4.2 K our smallest magnets often display abrupt transitions we do not interpret this as evidence for coherent switching for two reasons. First, the local fields that generate our hysteresis loops solely involve magnetization near the end of the particle. Even for a multi-domain vortex state, the process occurring at the magnet's end might evolve over an extremely small interval of the applied field. Second, once reversal is nucleated at the particle's ends, full reversal over the entire particle can occur very rapidly, on the scale of nanoseconds [72]. Hence, lack of coherence in switching dynamics may be unresolvable without special efforts to increase the temporal resolution of the measurements.

5.3.4 LHE Sensitivity

The ultimate sensitivity of the LHE deserves mention. For $M_s \approx 838$ emu/cm^3, the measurement of an individual 75 nm $\times$ 750 nm magnet (thickness 50 nm) implies a resolution of 2.36 $\times$ 10^{-12} emu, or 2.54 $\times$ 10^8 μ_B (Bohr magnetons). We expect that much weaker levels of magnetization are detectable. The n+ GaAs cross-junctions employed here have a room temperature Hall coefficient of $dR_H/dH \approx 80$ Ω/T. Hence at room temperature with a source current of $I_s = 0.5$ mA[6] and a room temperature voltage noise of $v_n = 10$ nV/Hz$^{1/2}$ (including amplifier noise and device thermal and shot noise), the ultimate field sensitivity is $B_n^{(rms)} = V_n/I_s \times (dR_H/dH)^{-1} = 2.5 \times 10^{-7}$ T/Hz$^{1/2}$.

Of course, the efficiency with which a Hall cross can sense the fringe field of a nanomagnet

[6]This level of current is chosen because it corresponds to modest (few mW) dissipation in a small device and a reasonable voltage drop across the device. (The typical series resistance of a device is 10 kΩ, so the resulting voltage drop is of order 5 V.)

depends on the relative alignment of the cross with the magnet. The optimal configuration is a thin disk ferromagnet of lateral dimensions slightly bigger than the cross-junction (to provide relatively uniform field through the cross), and situated directly above it, with magnetization perpendicular to the junction plane. For this calculation we assume a junction with electrically active area of radius 100 nm (similar to the smaller crosses discussed in these experiments) located underneath a disk that induces a field modulation of 2.5×10^{-7} T through the cross. The equivalent magnetic moment is given by $(V\Delta B)/(4\pi - N_d)$ where V is the particle volume, ΔB is the field modulation, and N_d, the demagnetization factor, is $4\pi\,[1-(\pi/2)(t/r)]$ for a thin (t/r small) disk of thickness t and radius r. With $r = 200$ nm (thickness drops out of the calculation) we then obtain a dipole sensitivity, per $\mathrm{Hz}^{1/2}$, of 3.17×10^{-18} emu, or 350 μ_B.

Geometrical considerations and noise are important in determining the precise value of this estimate, but the calculation clearly demonstrates the potentially great utility of the LHE as a magnetization probe. In addition, further optimization through the use of a lower noise amplifier and thinner conducting layers, allowing more effective coupling to strong magnetic fields present near the surface of the cross, is possible.

The spatial resolution of LHE magnetometry is ultimately limited by the smallest junction size attainable, which in turn is determined by edge depletion [60]. For an n+ electron gas as used here ($n \approx 10^{18}$ cm^{-3}) this is of order 10 or 20 nm, hence the smallest junction possible is, approximately, of area 4×10^{-16} m^2.[7] In techniques such as Kerr or magnetic force microscopy, the ultimate spatial resolution is limited by, respectively, the size of the laser spot (diffraction limit) or the field profile emanating from the cantilever tip. These are typically an order of magnitude larger. It is informative to consider the potential flux sensitivity of ultraminiature LHE devices. A 4×10^{-16} m^2 Hall junction fabricated as detailed above provides, when immersed in a uniform field, a flux sensitivity of 10^{-22} Wb/Hz$^{1/2}$, or 5×10^{-8} φ_0/Hz$^{1/2}$ where $\varphi_0 = h/2e$ is the flux quantum (2.07×10^{-15} Wb). Thus *room temperature* performance at the level of state-of-the-art cryogenically cooled thin film DC SQUIDs appears possible [73][74][75].

[7] Although a larger Hall coefficient results from the use of a lower density electron gas, the electrical depletion width then increases, and spatial resolution is degraded.

5.4 Summary

The LHE was investigated at first as a way of characterizing magnets for use in spin devices. The local Hall work soon became interesting in its own right as a novel way of characterizing the dependence of magnetic properties, such as coercivity and hysteresis loop squareness, on magnetic particle size and processing conditions. Understanding these properties, and being able to control them, is crucial to advancement in magnetic recording technologies such as GMR, spin-valve, and magnetic tunnel junctions. Individual micromagnets are not easily measured by conventional means, however—using a commercial SQUID susceptometer with typical sensitivity 10^{-7} emu, one would need 2300 NiFe particles of size 1 $\mu m^2 \times 50$ nm in order to reach the threshold of detectability. Information about individual particles, and the variation in properties among particles, is then left unknown.

As mentioned above, another method is placing single particles in the center of the pick-up coil of thin-film dc SQUIDs [74], but this approach has a much higher level of fabrication complexity and requires cryogenic temperatures. Alternative methods, based on electron microscopy [76], exist, including electron holography [77]; optical techniques based upon the Kerr effect [78]; and magnetic force microscopy [79][80]. These are excellent probes of the micromagnetic details of individual particles, but require specialized equipment and, except for the Kerr effect, are not readily adapted to the exploration of magnetization dynamics in swept fields (though we note that swept, high-field, techniques have recently been developed for MFM [81]). The work reported in this Chapter complements a previous demonstration of the utility of small Hall probes (without integrated nanomagnets) for characterization of magnetic surfaces [82]. This demonstration implemented a scanning probe arrangement yielding submicron spatial resolution.

There are four important virtues of the LHE. (1) It is an extremely *non-perturbative* technique: although improvements in MFM technology have allowed measurements on soft ferromagnetic films with seemingly minimal perturbation [79], progressively smaller tips with increasingly stronger gradient fields are required to obtain sufficient resolution for observing the smallest magnetic particles or domains. Coupling between the magnetic tip and sample can then become problematic in that it can perturb domain structure as scans are performed. By contrast, the LHE employs no additional magnetic materials and eliminates such concerns, though with the trade-off that one is sensitive only to one region of the

magnet. (2) The LHE provides *quantitative* information about local fields: the induced Hall resistance is directly proportional to the local field integrated over the cross-junction area; hence, with appropriate calibration, quantitative information can be extracted. (3) The LHE is readily applied to *swept-field* measurements whereas the application of external bias fields can cause complications in MFM or approaches based on electron microscopy. In the former case, the domain structure of the magnetic tip can be affected by H, and in the latter case electron trajectories can be shifted. No analogous issues arise with the LHE; any background Hall signal arising from the presence of a perpendicular component of H can be readily identified and subtracted. (4) The LHE has potential for true *dynamic* measurements because devices can be implemented in geometries providing very large bandwidths—measurements on sub-nanosecond time scales should be attainable through careful high-frequency design (employing leads formed as striplines or coplanar waveguides).

Finally, LHE devices are interesting as nonvolatile, radiation-hard, memory elements for magnetic random access memory (MRAM). The engineering issues relevant to such an application, such as power dissipation, large-scale integration, and timing, are not addressed in this work, but we note that the high sensitivity of LHE devices at room temperature, and their ease of fabrication, make a good case for future experimental efforts in this direction.

We conclude by considering the implications of our LHE work for spin devices, which was, of course, its original purpose. From the work described in this Chapter it is clear that thin film NiFe ferromagnets can be deposited with good control over their magnetic properties. The key characteristics of hysteresis loop squareness and coercivity are well understood and can be tailored to fabricate smaller spin devices whose properties should be much better understood than the comparatively crude PL devices discussed earlier. The integration of well behaved magnets with spin devices fabricated by electron beam lithography, and subsequent measurements, are the topics of Chapter 6.

Chapter 6 Spin Devices II: Electron-Beam Lithography

Having improved the magnetic characteristics of our NiFe ferromagnets using the local Hall effect, we next integrated the improved magnets into spin devices patterned by electron beam lithography (ebeam devices) [55]. These devices are much smaller than photolithographically patterned (PL) devices, and greatly increase the likelihood of successful spin injection and detection. We begin by discussing the devices and the key enhancements. We then move on to a discussion of measurement results and why there was a greatly reduced body of hysteretic phenomena. We conclude with a discussion of possible further improvements.

6.1 Ebeam Device Design and Implementation

Aside from enabling the fabrication of smaller devices, ebeam lithography is beneficial because the organic developer for the ebeam resist does not attack GaSb, AlSb, or InAs. Devices can therefore be processed with greater control. Before the move to full ebeam processing, we made some chips with a combination of photolithography and ebeam lithography, in an attempt to circumvent photoresist developer damage. These efforts were soon abandoned, however, because they were unreliable and, as the LHE work progressed, it became clear that the implementation of smaller, better controlled magnets was imperative. We then designed new masks, with the requirement that we be able to characterize the InAs and ferromagnet properties on-chip, so that any hysteretic behavior could be more easily interpreted.

A micrograph showing the basic chip layout is shown in Figure 6.1. The layout accommodates six 4-terminal spin devices and a multiprobe device (in the upper right corner) where Hall crosses, or other patterns, can be drawn for characterization purposes. Templates such as these were patterned by conventional photolithography techniques, usually in batches of 8 to 16 chips at a time. At least two steps were required: contact definition

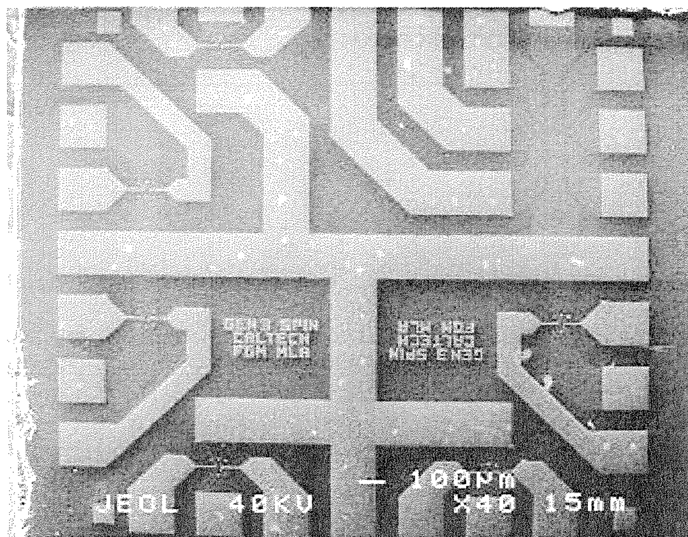

Figure 6.1: Micrograph of the chip layout for ebeam devices. There are 6 positions for spin devices while one corner, here in the upper-right, is devoted to material characterization.

(etch and metallization), and metallization for bond pads. A third step, the isolation etch, was also sometimes done, depending on the details of later processing. In such cases the regions on the chip intended for later ebeam patterning were intentionally left unetched.

Most ebeam patterning was carried out at a magnification of 1000×. At this level, the field of view was about 100 μm wide. Each spin device template has two metal lines, for connection to the ferromagnetic contacts, running horizontally into the field of view. The InAs channel is then patterned vertically so as to overlap with active InAs regions on the larger template. A low magnification view of two devices is shown in Figure 6.2. The metal lines, and their connection via smaller metal lines to the ferromagnets, are clearly visible. The crosses visible at the top and bottom of the pictures are alignment marks. Also visible are bright pairs of lines which mark the confinement of the InAs channel. The regions within each pair of lines was etched away, in principle isolating the InAs between the two pairs from the InAs outside them. The brightness results from residual bits of PMMA that were not removed by the acetone rinse. Such residual bits, also visible as dark streaks in other places in the micrographs, caused irreproducible results (isolation failure, bad contacts) at times.

Based on the results of our PL devices, we designed ebeam devices in two geometries, as shown in Figure 6.3. One design is essentially, at smallest contact separations, a cross-junction similar to the type III PL devices. For larger separations the cross is distorted,

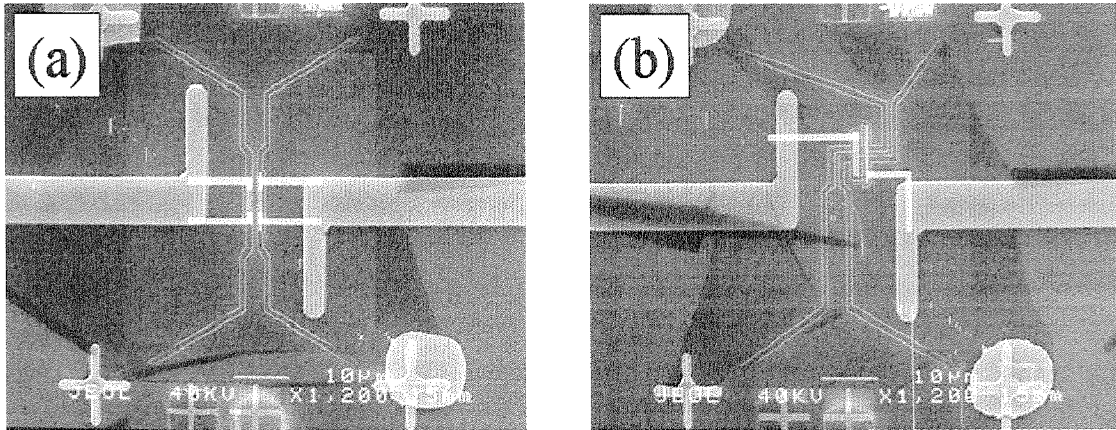

Figure 6.2: Two low magnification micrographs of spin devices. The large metal lines coming in from each side connect to the ferromagnetic contacts via smaller metal lines.

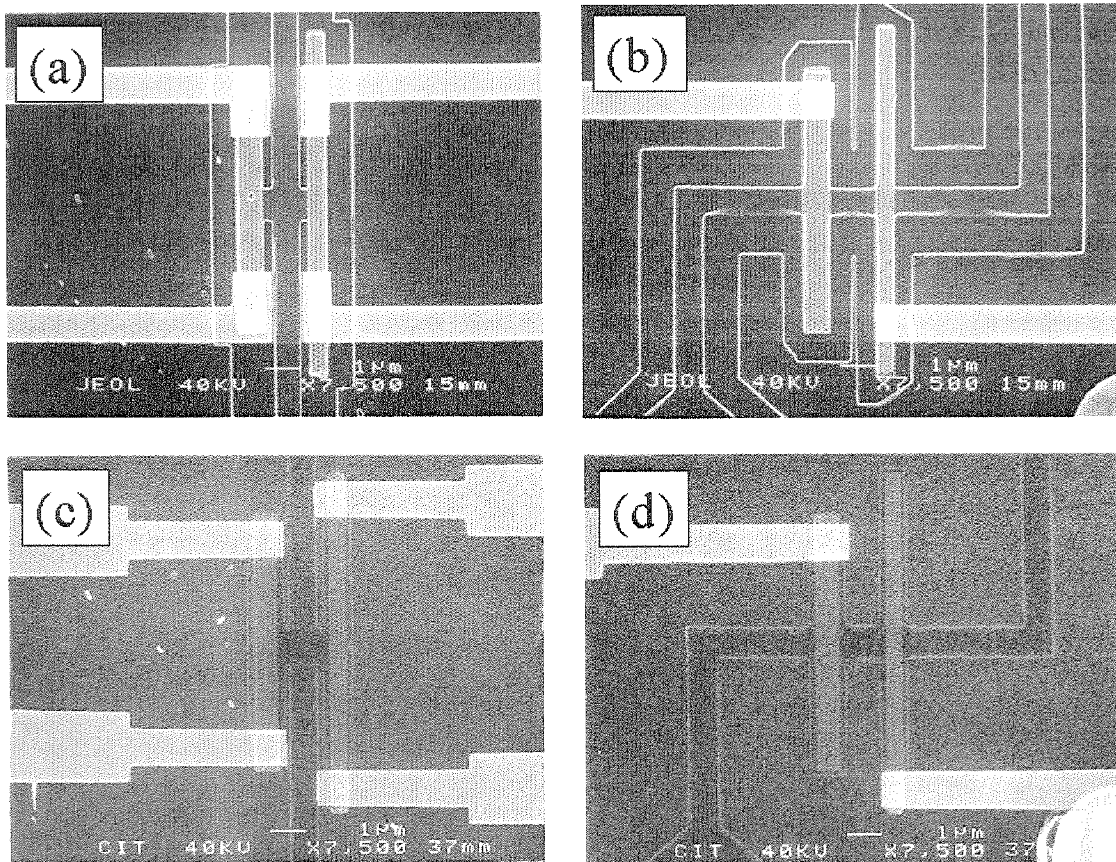

Figure 6.3: Four micrographs of ebeam spin devices. (a) and (b) are from early rounds of PMMA-masked devices. The active InAs channel is isolated from the surrounding chip by etching in parallel trenches on either side of the channel, so 4 lines are visible. (c) and (d) show later SiO_2-masked devices with ECR etching.

making the devices more similar to type II PL devices. Our other design is essentially the same as the type IV PL devices. The Figure shows devices from both early processing runs (using PMMA as a mask for Ar ion milling) where residual PMMA shows up as bright lines, and later processing runs (using SiO_2 as a mask for ECR etching). We will refer to (a) and (c) devices as 'nonlocal' devices from now on, in reference to the fact that contacts are offset from the main InAs channel. Likewise, (b) and (d) devices will be termed 'in-line' devices since their contacts are placed directly in the channel. In all of the ebeam devices the ferromagnets sit on top of an InAs window slightly bigger than the ferromagnets themselves, resulting in a planar interface that is superior to the interface in PL devices, where small windows where etched underneath a large magnet. The highest alignment precision attainable from one ebeam layer to the next was often better than 50 nm. As seen in the micrographs, channels were about 900 nm wide. Contact separations in nonlocal devices started around 1.5 μm and increased to a few microns. Similarly, separations in in-line devices started at 750 nm. Magnet dimensions varied slightly but for the most part were 750 nm $\times$ 7.5 μm and 500 nm $\times$ 10 μm. Slight roughness in the SiO_2 liftoff was sometimes present, likely due to less than perfect development of the PMMA.

Errors in fabrication of ebeam devices ranged from slight to potentially disastrous. Some examples of slight errors are shown in Figure 6.4 (SiO_2 process). In (a) the left magnet is distorted due to an error in the computer-generated pattern. Such errors were easily fixed. In (b) one can see a slight increase in channel width near the ferromagnets due to secondary electron exposure. This is not a serious problem, since such slight geometry changes should not appreciably change our expectations for spin-coupled transport. Such overexposure could be minimized by lowering exposure dosage in the SEM or by slightly compensating in the pattern design itself. In (c) a slight misalignment is apparent between the ferromagnets and the SiO_2 mask for the isolation etch. Such misalignment was sporadic and unavoidable. Assuming the misalignment was not too severe (the example in (c) is ok), devices were not adversely affected. The only case in which this may not be true is in the alignment of the ferromagnet layer to the previously defined contact windows. Misalignments here could cause the ferromagnets to run over steps, perturbing their magnetic properties. InAs windows were thus made somewhat larger than the ferromagnets (about 25 nm to 75 nm on each side), leaving a small region of exposed InAs, probably with reduced mobility, without ferromagnet coverage. This detail was unavoidable.

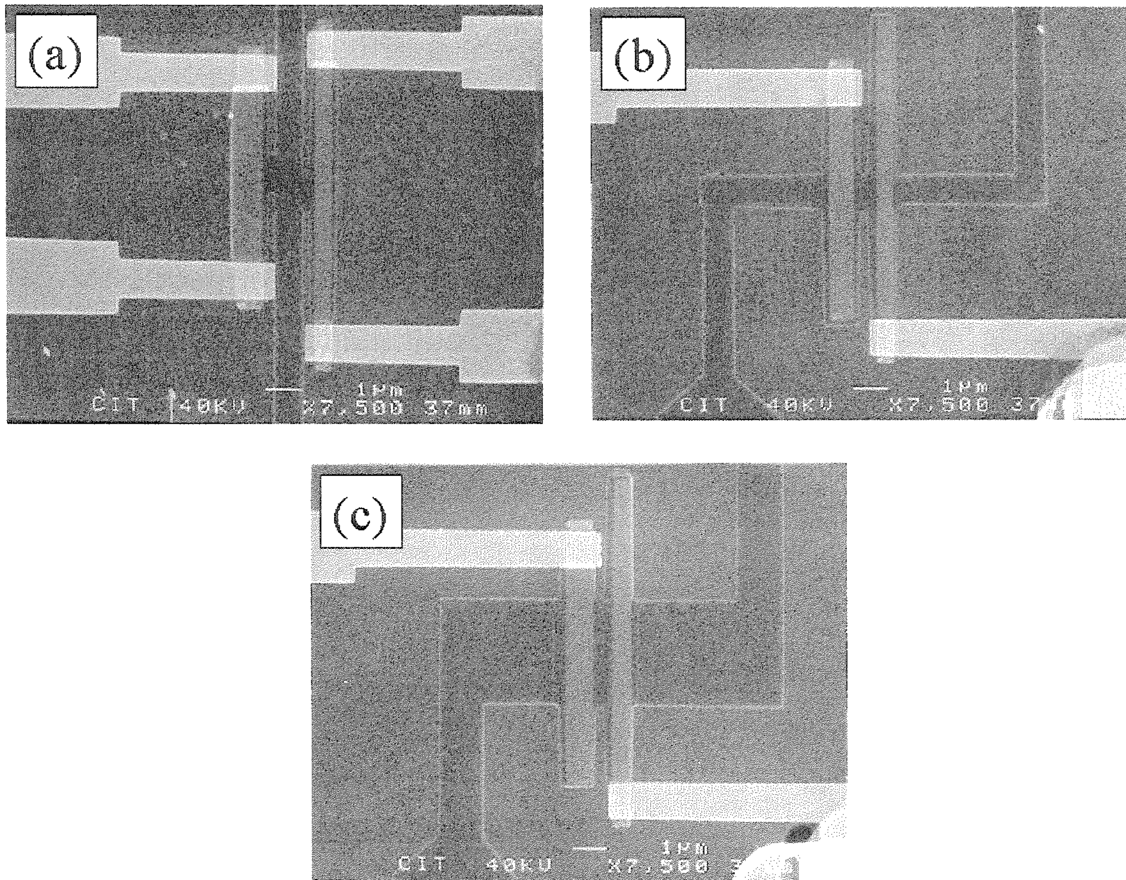

Figure 6.4: Micrographs showing slight errors in ebeam devices (SiO_2 series). The (a) device is an example of a nonlocal device with a distorted cross. The (b) device is an in-line device with 750 nm separation. The (c) is a slightly modified (wider channel) in-line device with 500 nm separation. See the text for a complete description.

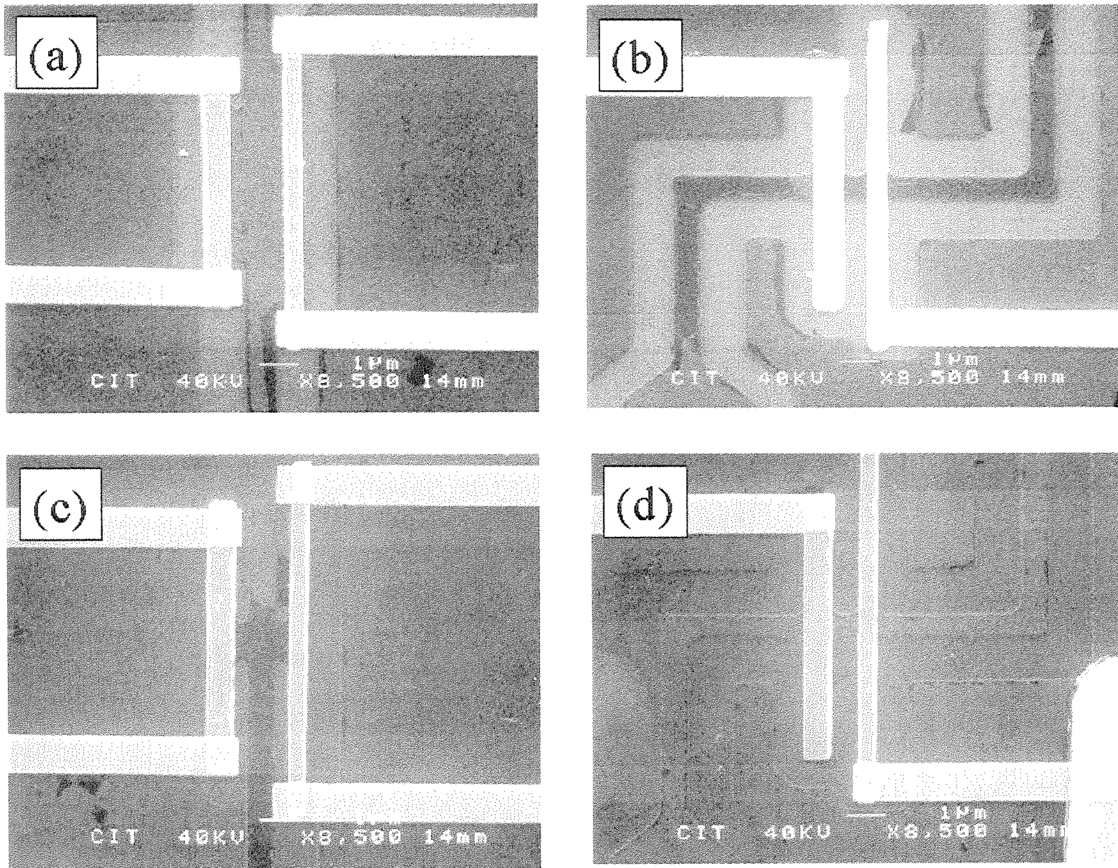

Figure 6.5: Micrographs showing more serious defects in ebeam devices (PMMA series). The four devices here are from two chips processed together, yet there are large variations in their appearance.

More serious defects are shown in Figure 6.5. All of the devices shown in the Figure were processed using PMMA as a mask for Ar ion milling. The (a) and (b) devices, both from chip IA40, show PMMA residue (dark regions) and evidence of overexposure. The (c) and (d) devices, both from IA41 which was processed in parallel with IA40, also show some amounts of residue, though (d) is fairly clean. The overexposure problem was related to overheating of the PMMA after developing and was easily avoided, but the problem of PMMA residue was never solved. Residue could be removed by O_2 plasma ashing, but only at the expense of oxidizing the chip surface. Due in part to these residue problems, approximately half of the PMMA-masked devices were not electrically sound—very high resistance contacts or nonlinear contacts being the common failure mechanisms. Note also that the magnets in the devices in Figure 6.5 have prominent liftoff flags. These could usually be removed by ultrasonication, assuming good adhesion of the NiFe.

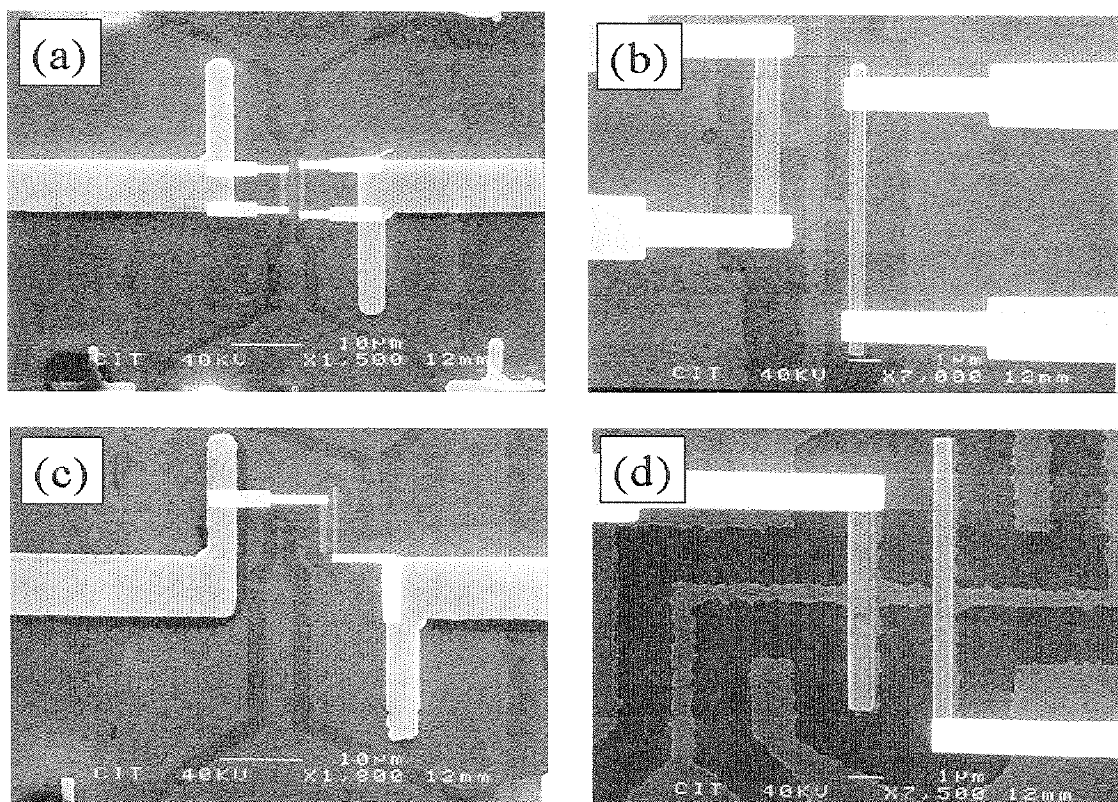

Figure 6.6: Micrographs of wet-etched ebeam devices. In (a) and (b) are nonlocal devices and in (c) and (d) in-line devices.

Processing with SiO_2-masking, though more complicated, was a great improvement to the appearance and reproducibility of ebeam spin device processing. Some attempts were also made, however, with PMMA masking and wet etching. In this case PMMA was an adequate mask, but the fabrication suffered from undercutting, which was very difficult to control, and etch roughness. Examples of this are shown in Figure 6.6. Though careful timing would sometimes avoid destruction of the devices by undercutting, in these cases the quality of device isolation or smoothness of the etches (see Chapter 3) was always unknown. These facts led to the abandonment of small scale wet etching.

As mentioned above, characterization of the InAs material and ferromagnet properties via the LHE was also possible with these spin chips. Normally, we patterned the multiprobe device area into a series of 3 Hall crosses. Often two ferromagnets, of the same dimensions as the ferromagnets in the spin devices, were then deposited, one on each cross. This is shown in Figure 6.7. The information obtained from these characterization devices was very useful in understanding the properties of the spin devices.

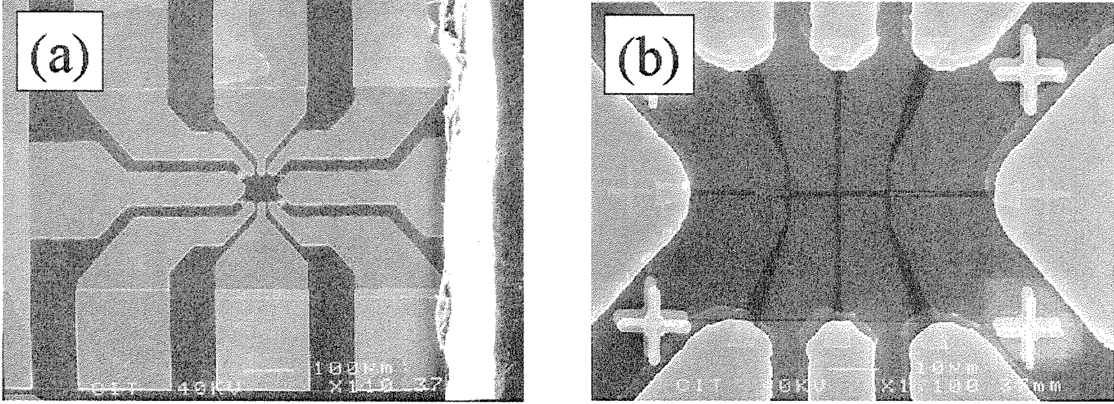

Figure 6.7: Micrographs of the multiprobe device that was part of each spin chip. The line of three crosses was used for InAs characterization. Ferromagnets, each positioned with one end over a cross, could also be analyzed by the LHE.

6.2 InAs Ebeam Spin Chip Measurements and Results

Although we measured many dozens of ebeam spin devices, hysteretic phenomena were extremely scarce, occurring on only a few devices. At times certain features would be observed for a few sweeps but not for others, suggesting perhaps a dependence on micromagnetic structure that was not reproduced exactly from sweep to sweep. We first discuss the results of the on-chip characterization of our InAs.

6.2.1 InAs Characterization

The vast majority of ebeam devices were fabricated from the same heterostructure, shown in Figure 3.1. One heterostructure was used because the results of etch times and processing conditions were then, in principle, reproducible. After growth this quantum well was reported to have a mobility and carrier density, at 12 K, of $\mu = 6.12 \times 10^5$ cm^2/Vs and $n_s = 1.08 \times 10^{12}$ cm^{-2} (values extracted from van der Pauw measurements). Our on-chip Hall bar characterizations agreed with the density estimate quite well, with values ranging between 0.95×10^{12} cm^{-2} and 1.33×10^{12} cm^{-2} (though there was one anomalous result of 1.6×10^{12} cm^{-2}). The mobility measured with our Hall bars was consistently low, however, ranging for the most part between 2.3×10^5 cm^2/Vs and 3.5×10^5 cm^2/Vs for a variety of etch techniques.

Plots for two spin devices are shown in Figure 6.8. An ion milled (PMMA-masked)

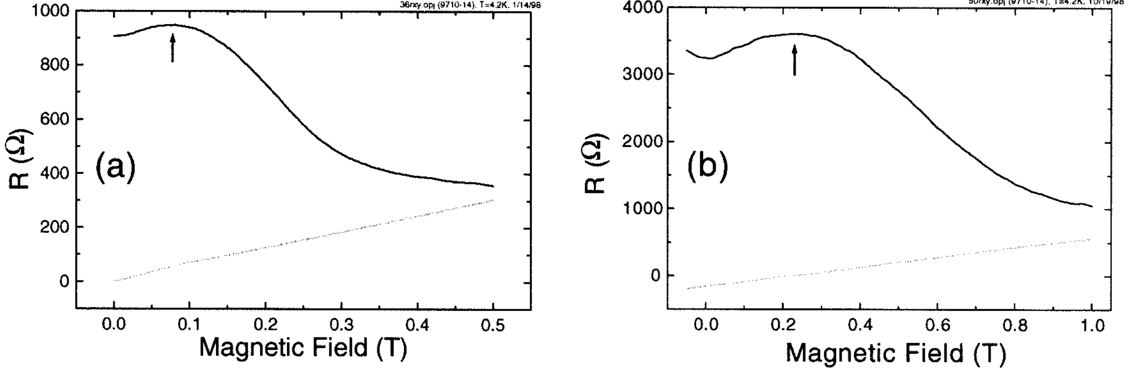

Figure 6.8: Longitudinal (R_{xx}, in black) and transverse or Hall (R_{xy}, in gray) resistances for two spin chips. The (a) device was PMMA-masked and ion-milled, while the (b) device was wet-etched.

device, IA36, is shown on the left and a wet etched device, IA50, on the right. The gray lines are Hall resistances and the black lines are longitudinal resistances through a channel 1.5 μm wide and 22.5 μm long, lithographically. Carrier densities are easily extracted from the Hall resistances, given that $R_H = H/n_s e$ where H is the external field. Mobilities are more difficult, because the actual electrical width of the channel is unknown and may be affected by etch conditions. We therefore use the boundary scattering peak, shown in the traces as a hump in R_{xx}, which results from the fact that scattering of electrons from the channel sidewalls usually has a non-specular, or diffusive, component [56]. This results in a magnetoresistive peak centered at a characteristic field $B_{\max} = 0.55\hbar k_F/ew$ where $k_F = \sqrt{2\pi n_s}$ is the 2D Fermi wavevector magnitude and w is the electrical width of the channel. This expression shows that $B_{\max}$ is larger for narrower channels. Having extracted the correct value for w, we can then obtain mobility from $R_{xx} = (n_s e\mu)^{-1}L/W$ where we use a value for $R_{xx}(H)$ at fields of several thousand Oe, where boundary scattering phenomena have died off but Shubnikov de Haas phenomena have not yet commenced (in this region the resistance simulates the bulk resistance one would obtain from van der Pauw measurements, without etching channels in the InAs). Values for a representative sampling of chips are given in Table 6.1.

Similar traces were also obtained from devices masked with SiO_2, although in several cases the boundary scattering peak was not clearly delineated and therefore an accurate determination of the electrical width could not be obtained. Example traces from SiO_2 devices are displayed in Figure 6.9 for an ion milled device, IA61, in (a) and ECR etched

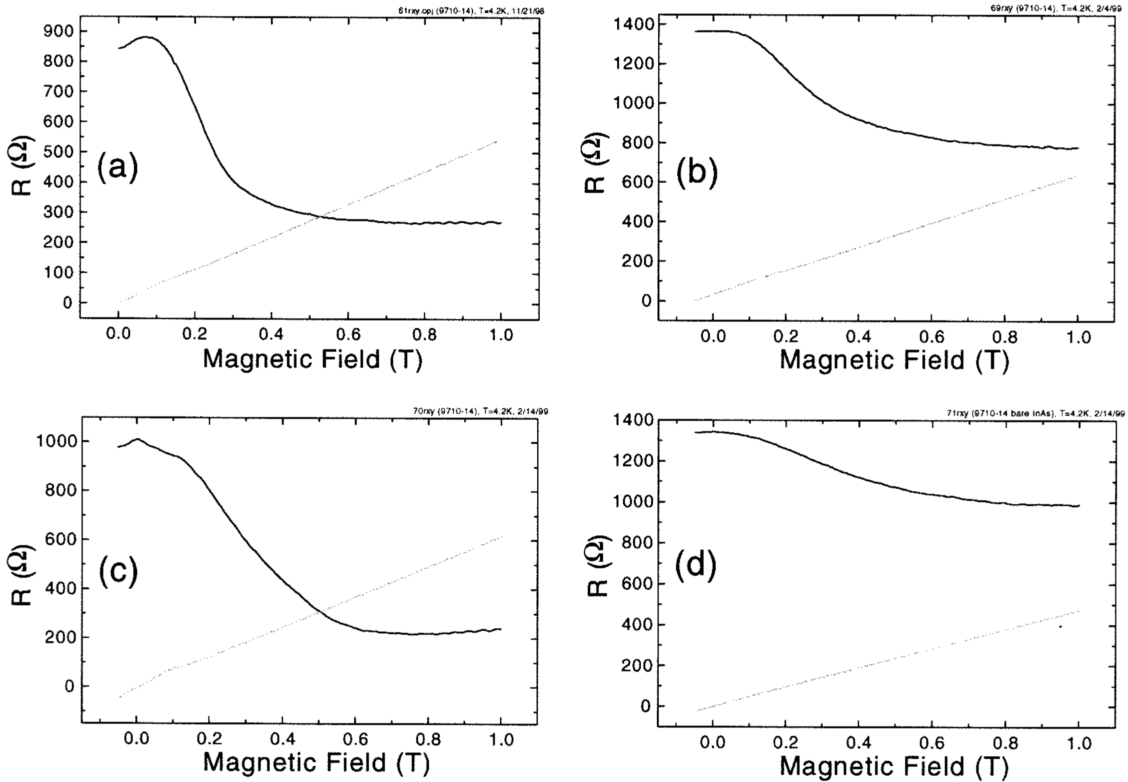

Figure 6.9: InAs characterization from four SiO_2-masked chips. In (a) an ion-milled device, in (b) an ECR-etched device without a clear boundary scattering peak, and in (c) another ECR device, with channel length 11.25 μm instead of 22.5 μ m, without a clear boundary scattering peak. In (d) the entire device was ECR etched down to bare InAs, so the mobility was lower (R_{xx} higher).

Chip #	Process	n_s ($\times 10^{12}$ cm^{-2})	w (μm)[a]	μ ($\times 10^5$ cm^2/Vs)
IA30	PMMA	1.28	1.26	2.54
IA33	PMMA	1.19	1.23	3.07
IA34	PMMA	1.02	? (use 1.2)	2.30
IA36	PMMA	1.04	1.17	3.30
IA37	PMMA	1.07	0.97	1.13
IA39	PMMA	1.03	1.35	2.47
IA49	wet etch	0.95	0.38	2.60
IA50	wet etch	1.25	0.44	2.44
IA61	SiO_2, ion mill	1.17	1.40	3.24
IA62	SiO_2, ion mill	1.10	1.52	3.56
IA66	SiO_2, ECR	? (use 1.15)	1.45	4.28
IA67	SiO_2, ECR	1.60	? (use 1.45)	1.20
IA69	SiO_2, ECR	1.04	? (use 1.45)	1.20
IA70	SiO_2, ECR	1.09	? (use 1.45)	2.03
IA71	SiO_2, ECR[b]	1.33	? (use 1.45)	0.74

[a]This is the electrical width as extracted from the boundary scattering peak, if possible. If not, a value for similar chips is used. Almost all channels were nominally 1.5 μm wide lithographically (although SiO_2-masked channels may have been larger due to slight overdevelopment of the PMMA).
[b]IA71 was etched down to bare InAs before the isolation etch.

Table 6.1: Carrier densities, electrical channel widths (out of 1.5 μm nominally), and mobilities for a sampling of ebeam spin devices.

devices (IA69, IA70, and IA71 respectively) in (b), (c), and (d). The ECR devices show broad, poorly defined, boundary scattering peaks. Also, the (d) device had its cap layer removed, so that mobility was reduced. Referring to Table 6.1 we see that the ECR devices have lower mobilities (there is some uncertainty in this, since the electrical width could not be determined). This is perhaps due to the fact that etching significantly beyond the InAs layer was necessary to achieve good device isolation (though this was observed in ion milled devices, it was more dramatic in ECR devices). The specifics of density and mobility in these InAs quantum wells are not easily predictable (they are not intentionally doped) but it is likely that removal of material behind the InAs layer contributes to changes in the electronic structure of the quantum well. We also note that the ECR etching was not as repeatable as we would have liked, either due to other gases introduced into the chamber or pump or vacuum gauge variations. This was circumvented by testing etch speed before doing the real etch on each spin chip, and by providing for step height characterization of the real etch on each spin chip.

In any case, we note that for a mobility of 3×10^5 cm^2/Vs and a carrier density of

1.15×10^{12} cm^{-2} the elastic mean free path for electrons in our InAs is 5.3 μm. So even for the reduced mobilities encountered here our smaller devices are strongly ballistic. The result for IA71 is also important because it shows the degree to which there is a mobility reduction when the cap material is etched away. This decreased mobility is unavoidable, but we still expect spin dephasing via the Rashba effect to be the dominant mechanism for relaxation of the injected magnetization.

We conclude from the results of our on-chip characterization that, while our processing clearly impacts the characteristics of the InAs quantum well, material parameters after processing are very reasonable for the fabrication of spin devices. Since InAs is intrinsically a material that conducts, with relatively high carrier density (due to Fermi level pinning), a greater concern is the achievement of device isolation. This was accomplished, if sometimes at the expense of lowering the device mobility. The goal in using a semiconductor quantum well is not, however, specifically to measure ballistic phenomena but to remove our devices from the regime of spin-impurity scattering (the diffusive spin scattering regime in metals). This is certainly achieved in even the lowest mobility devices. We now turn our attention to the characterization of our ferromagnets.

6.2.2 Ferromagnet Characterization

The characterization of our ferromagnetic contacts was accomplished by measuring the local Hall voltages induced by magnets deposited on our multiprobe device. Magnets were deposited at the same time as the magnets for the spin devices so should reflect the same switching characteristics. Examples of this characterization are shown in Figure 6.10. Both pairs of ferromagnets in the Figure are ebeam evaporated NiFe but the (a) magnets are approximately 400 Å thick while the (b) magnets are 600 Å thick. Perhaps for this reason the (b) magnets share a coercive transition almost identically for negative applied field, and therefore are not suitable for polarize/analyze experiments, whereas the (a) magnets have well separated coercivities. Information such as this was very useful in determining the right sizes for magnets.

Two later sets of magnets are shown in Figure 6.11. The problem of overlapping coercivities in NiFe magnets is easily overcome in (a) by making the magnets thinner, here approximately 160 Å. The (b) magnets are from the one spin chip that used CoFe magnets, 200 Å thick. The magnet dimensions in this case are 175 nm $\times$ 3.5 μm and 500 nm $\times$ 5

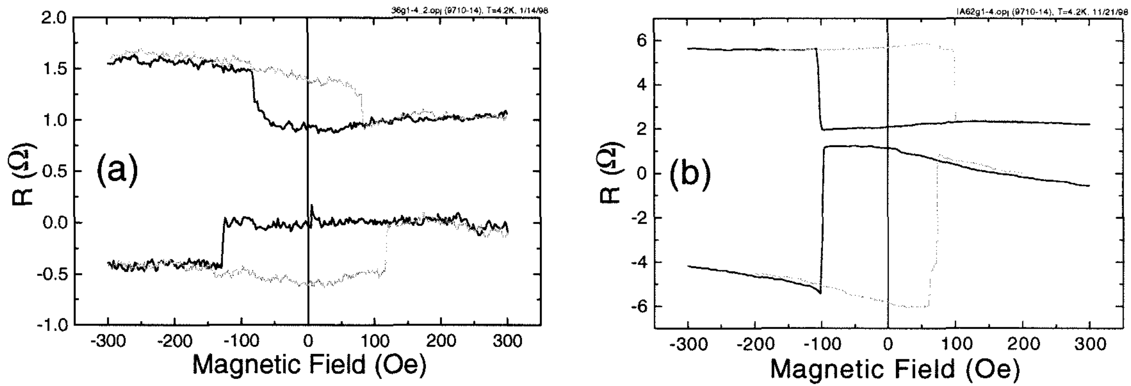

Figure 6.10: On-chip local Hall characterizations of two pairs of NiFe magnets. The pair in (a), from IA36, looks good but the (b) pair, from IA62, has nearly identical coercivities for negative applied field. The (a) traces have had a linear background subtracted away. In both cases the traces are offset for clarity.

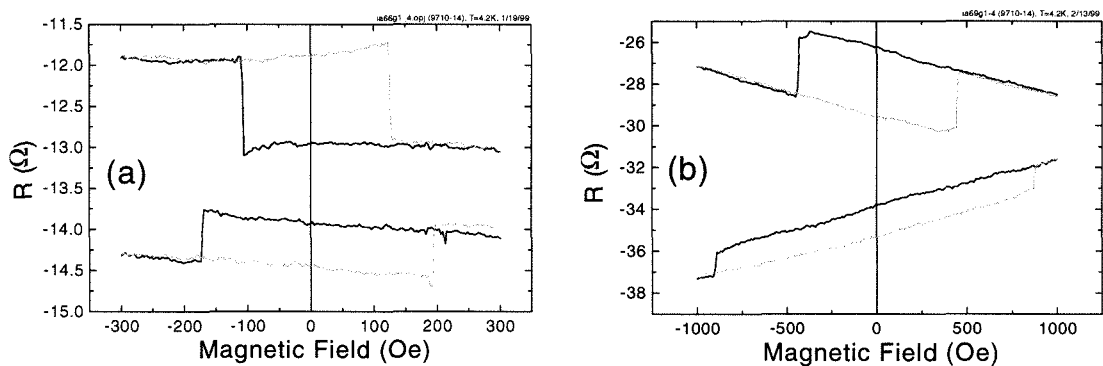

Figure 6.11: Two more local Hall characterizations of spin device magnets. Both sets were thermally evaporated after an Ar clean in the ECR. The (a) magnets, from IA66, are NiFe while the (b) magnets are CoFe. The traces are offset vertically.

μm. It is harder to control the coercivity of Co-based magnets, so we implemented smaller magnets. Even so, the CoFe magnets often did not perform as well as the pair shown. Both sets of magnets displayed in the Figure were thermally deposited after a brief Ar clean in the ECR. The linear background in (b) is probably due to some misalignment of the chip with respect to the applied field.

In summary, magnet characterization via the LHE was very useful as a guide to the performance of the magnets in our spin devices.. Switching characteristics for NiFe magnets were fairly reproducible, so that polarize/analyze experiments were not hindered by uncontrolled magnets. Though these magnets are almost surely not strictly single domain, as discussed in Chapter 5, hysteresis loops were for the most part square, implying that micromagnetic difficulties were kept to a minimum.

6.2.3 Spin Device Results

Polarize/analyze experiments were conducted on ebeam devices essentially in the same way as on PL devices. The major improvement was in the acquisition of the three-axis superconducting magnet. Whereas Hanle effect (that is, perpendicular field) measurements were hindered from the start in PL devices because only one field direction was accessible (and because the ferromagnets were not well controlled), for ebeam devices this was not a stumbling block. Ferromagnets could, in principle, be saturated in a given direction and then a perpendicular field turned on to effect precession of the spins. In practice, the presence of slowly varying magnetoresistive backgrounds confuses the interpretation of perpendicular field measurements. The alternative is sweeping magnetic field perpendicular to the magnets' easy axis (which is the spin direction) but *in-plane.* This should check for Hanle phenomena as well, while potentially removing the confusion of magnetoresistive backgrounds. Here the challenge is preventing the magnetization of the ferromagnetic contacts from changing in the strong field applied perpendicular to their easy axis. This would inevitably lead to the development of possible local Hall voltages in the InAs channel, again obscuring results. For our NiFe magnets we expect the magnetization to be affected above a thousand Oe, so this alternative has not been explored.

Some early hysteretic results are shown in Figure 6.12. An in-line device from IA36 with separation 750 nm is shown in (a) while nonlocal devices from IA41 are shown in (b), for a cross geometry, and (c) for a distorted cross with leg separation 1 μm (as in

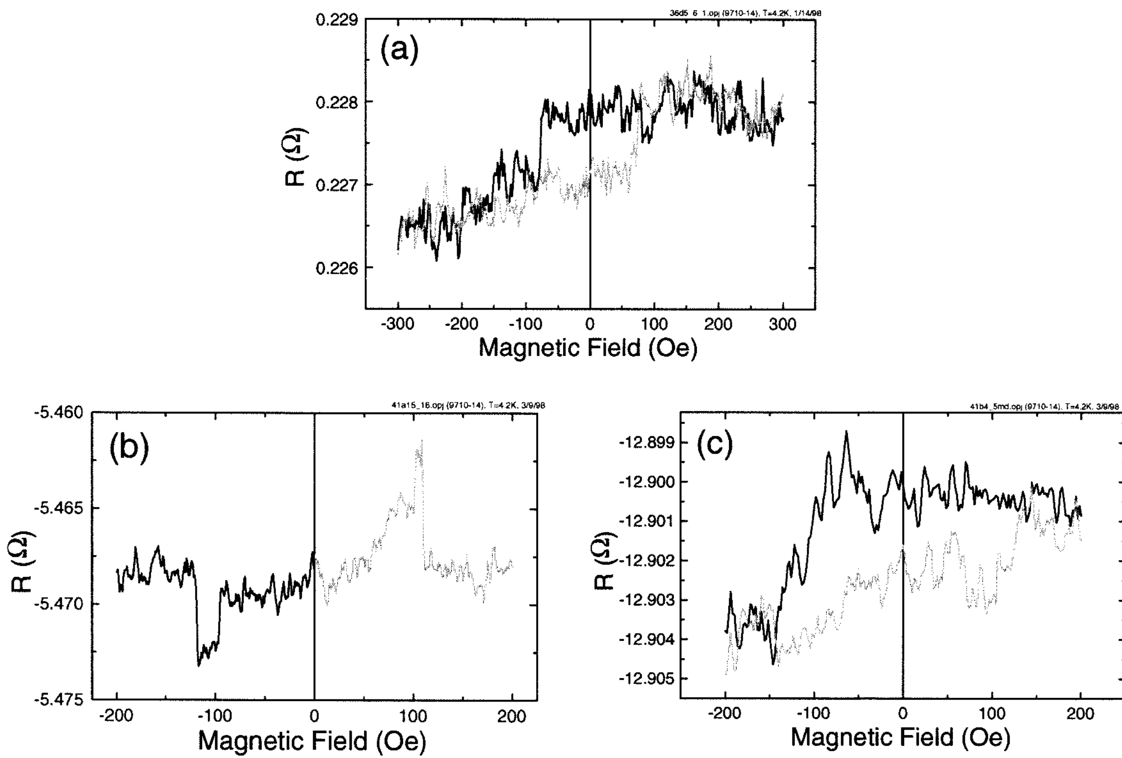

Figure 6.12: Hysteretic phenomena from three ebeam spin devices. The (a) device is in-line with contact separation 750 nm. The (b) device is nonlocal (cross geometry) with contact separation of 1.5 μm. In (c) the device is nonlocal (distorted cross where the legs are offset by 1 μm). In all cases the probe configuration is R_m. Linear backgrounds have been subtracted away in each case.

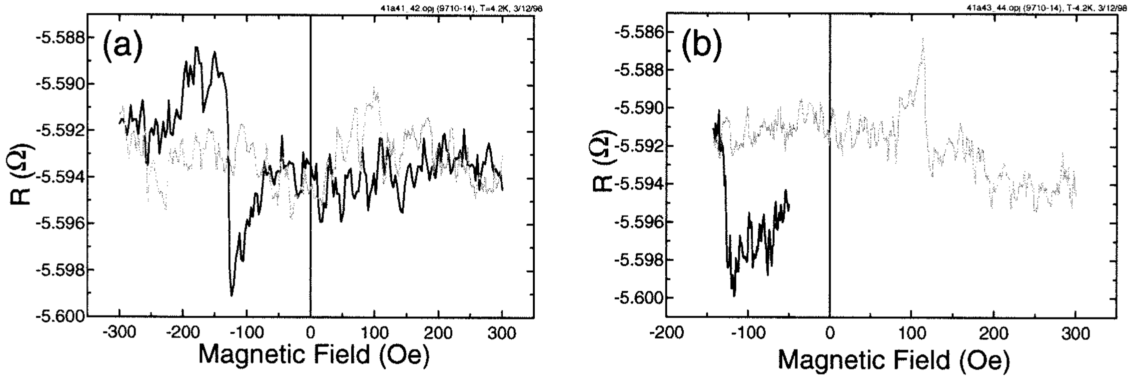

Figure 6.13: Two more sets of sweeps from the IA41 device of (b) in the previous Figure.

Figure 6.4(a)). Source current is 50 μA in each case. These results are especially interesting because they are all for the R_m probe configuration, which rarely showed hysteresis in PL devices, and which should be less susceptible to local Hall phenomena. Nevertheless the (a) trace looks very much like a hysteresis loop and we attribute it to the LHE. The trace in (c), similarly, looks like a loop, although there may be a dip/peak structure near the transitions. We further note that the scale of the local Hall signals here is hundreds of times smaller than in many of the PL devices, evidence of the superior design of ebeam devices. By moving the edges of the ferromagnets far from the conduction channel of the device (and by implementing quasi-single domain magnets) the role of magnetic fringe fields in device operation has been greatly reduced. The data in (b) are more intriguing. We would expect either two dips or two peaks in a spin-coupled signal, so that we hesitate to attribute the phenomenon to spin injection. However, the features are wider than we would expect for a signal whose origin is in local Hall voltages, since our small magnets typically switch over an interval of a few Oe. Micromagnetic phenomena, on the other hand, could also be playing a role.

Many measurements were made on the (b) device. Two more examples are shown in Figure 6.13 for a source current of 10 μA. In (a) the appearance of the hysteresis has changed slightly, so that perhaps two peaks, with a dip before the negative field peak, are visible. In (b) we show an example of the 'memory effect' where we attempt to demonstrate two zero-field states. This was successful in some cases but not in others. Finally we note that perpendicular field sweeps were executed on these devices, to search for precessional (Hanle) effects, but these were inconclusive.

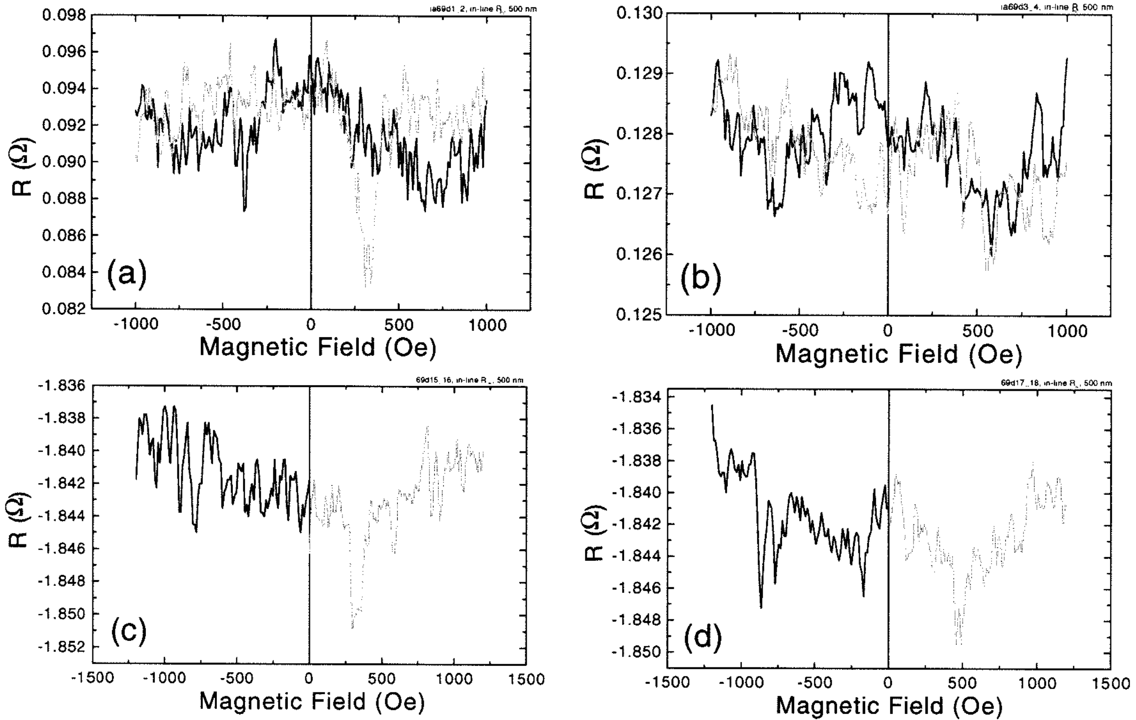

Figure 6.14: Data showing varied amounts of hysteresis in an in-line device with 500 nm contact separation and CoFe contacts.

The three devices in these examples illustrate the only fully reproducible examples of hysteresis we encountered in measurements of well over a hundred NiFe/InAs devices. In some devices, possible hysteretic phenomena were apparent in some sweeps but not in others, but even these cases were rare. One other InAs device, an in-line device with 500 nm contact separation and CoFe ferromagnets from IA69, demonstrated possible hysteresis as shown in Figure 6.14. In (a) the source current was 4 μA and two dips, the positive field one much more prominent, are visible. Immediately after this sweep the current was raised to 40 μA and the data in (b), which shows nothing discernible, were obtained. After measuring other devices, we returned to this device and acquired the data in (c) and (d) for 40 μA drive. Again the data are interesting but, without a clear confirmation of spin transport such as the Hanle effect, no firm conclusions are drawn.

Although perpendicular field measurements never proved useful, we show some examples of such sweeps on nonlocal devices in Figure 6.15. The (a) device, from IA66, is a cross geometry and the (b) device, from IA67, is a distorted cross with 2 μm leg separation. In both cases the source current was 4 μA and the probe configuration was R_m. In (a) the

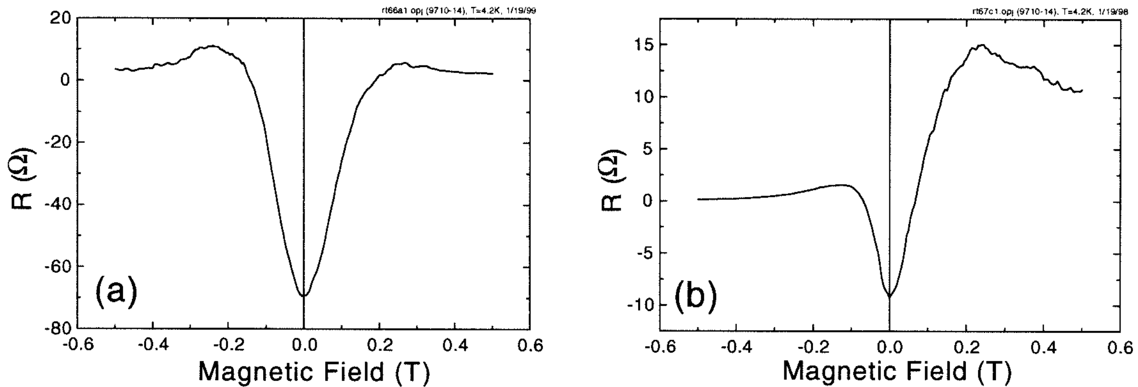

Figure 6.15: Perpendicular field sweeps of two nonlocal devices (R_m configuration) showing transfer resistance backgrounds.

data represent a very nice example of a transfer resistance (discussed more in Appendix C) while in (b) the trace is very asymmetric, though the transfer resistance is still recognizable. Data such as these, with varying amounts of asymmetry due either to contact or channel imperfections, were common in perpendicular sweeps on nonlocal devices.

Examples of perpendicular field measurements on in-line devices are given in Figure 6.16. In all cases the source current was 40 μA and the probe configuration was R_m. The (a) and (b) devices, from IA65 and IA67 respectively, have 750 nm contact separation while the (c) device, from IA69, has 500 nm separation (and CoFe contacts). The broad, symmetric, shapes displayed in the Figure are typical of perpendicular field measurements of in-line devices.

The field scale on which we would expect to see spin-coupled modulations in these perpendicular field sweeps deserves mention. The electrons that diffuse from one contact to another travel different path lengths due to scattering by channel sidewalls (or rare bulk scattering events), as discussed in Chapter 2. This variation in path lengths eventually leads to loss of spin polarization at distances farther removed from the injector contact. The field scale of this precessional polarization loss which, in the absence of appreciable spin-flip scattering, is the dominant mechanism of spin relaxation, is discussed more fully in Chapter 7, but for our material it is expected to be on the scale of a Tesla or more. In fact we anticipate that due to the lack of real spin-flip scattering in our material, oscillations should in principle be observable in the Hanle effect. While the period of such oscillations is shown in Chapter 7 to be dependent on injector-detector separation, it can easily be larger

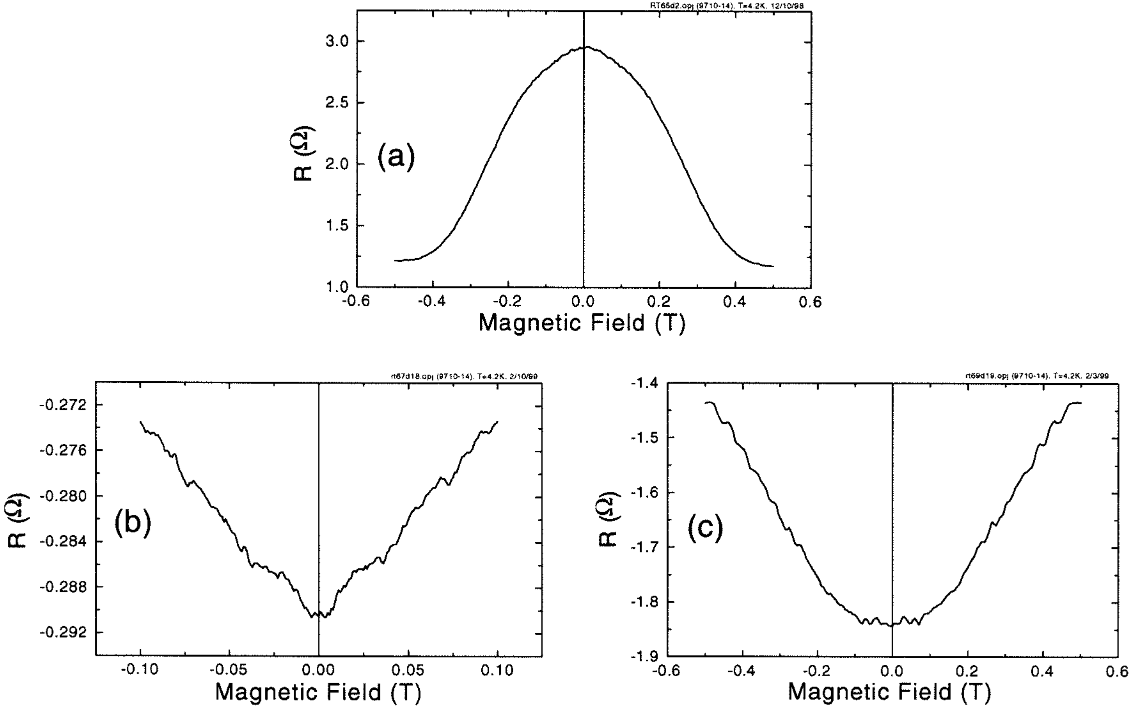

Figure 6.16: Perpendicular field sweeps of in-line devices (R_m config.). The broad, symmetric, backgrounds seen here were common in such sweeps.

than 1 Tesla.

As a final note, we point out that the magnitude (voltage or resistance) of any Hanle phenomena should be on the same scale as hysteretic phenomena in polarize/analyze experiments. Thus, even though some of the data in Figure 6.16 may look appealing, the absence of strong hysteretic dips or peaks in parallel magnetic field in these same devices essentially rules out Hanle phenomena as the interpretation for the magnetoresistances observed. To conclusively prove the existence of a spin-coupled signal, one would like to have a polarize/analyze result backed up by a demonstration of the Hanle effect. Furthermore, one should be able to show a change in this Hanle signal depending on whether the injector and detector are aligned or anti-aligned.

6.3 Summary: Inefficient Interfacial Spin Transfer

We conclude this chapter by applying Eqn. 2.8 to our ebeam device results. This equation was derived for the diffusive transport regime and therefore can only be used as an approx-

imation. Nevertheless in the limit of high resistance interfaces—which, from the discussion of Chapter 2, is likely the appropriate limit for our interfaces—corrections for ballistic transport are perhaps less significant since spin injection is dominated by spin dynamics at the interface rather than in the bulk. Assuming a spin polarization transfer across the ferromagnet/InAs interface of $\eta = 0.05$ we estimated a spin-coupled resistance of 175 mΩ. In many of the devices discussed here a signal of a few mΩ or greater would have been readily detected. To explain our experimental results within this model we would require $\eta \leq 0.005$, meaning that the current injected into the InAs must be less than 1% spin-polarized.

In light of the fact that spin-coupled signals should be stronger in smaller devices than in larger devices, the lack of hysteretic phenomena in ebeam spin devices is very significant. In comparison to the wealth of such phenomena in PL devices, these null results provide further indication that the hysteresis in PL devices did not likely have its origin in spin injection. In the rare cases where a hysteretic signal was evident in our ebeam devices, it was extremely difficult to prove whether it arose from a spin transport signal or not. The polarize/analyze experiment, while an excellent method of quickly determining whether magnetoelectronic phenomena are at work in a device, does not provide conclusive proof of spin injection. This is true even if demonstrations of a memory effect are successful.

The more rigorous demonstration provided by the Hanle effect is more convincing, since it is not susceptible to local Hall voltages. But it is also difficult to separate from magnetoresistive backgrounds arising from ballistic junction scattering phenomena (such as the transfer resistance signals explained in Chapter 7). This difficulty is intrinsic to low density semiconductor 2DEGs with soft ferromagnetic contacts. Either one sweeps field perpendicular to the sample surface, in which case the other magnetoresistive phenomena cause confusion; or one sweeps in the sample plane but transverse to the easy axis of the ferromagnets, in which case the ferromagnets' magnetizations can be influenced, and hence also the injected spin polarization. Without the clear demonstration of Hanle phenomena, any claim of spin-coupled transport must be treated with skepticism, because local Hall voltages will always be present (even in metals). We have shown that such spurious local Hall signals can arise from non-optimal device design (resulting in a high sensitivity to fringe fields from the ferromagnetic contacts) or from uncontrolled magnetic domains. The latter have the potential to compromise the homogeneity of the injected spin polarization, even in otherwise well behaved ferromagnets.

A large body of hysteretic phenomena in our ebeam devices, especially in the R_m probe configuration, would have been tantalizing evidence of spin injection. We fully expect to have seen such phenomena, especially in our in-line devices with contact separations less than 1 μm. This evidence is lacking, however, despite our control of (and on-chip characterization of) device parameters such as nanomagnet coercivity and domain structure; channel geometry, mobility and carrier density; and contact separation. This leads us to conclude that our devices suffer from the lack of a strong spin-polarized injection current. Our InAs processing seems adequate, as does the performance of our ferromagnets, but the ferromagnet/InAs interface is uncharacterized. Aside from the possibility of interdiffusion of materials at the interface, it may be that the band structures of NiFe and InAs are simply not very well matched. Such subtle issues are known to be important in the operation of GMR devices—even with a perfect interface, injection from the majority spin band in the NiFe may be inefficient due to a lack of available states in the InAs. Other magnetic materials might provide better matches to InAs, but in the absence of extensive theoretical calculations, this remains uncertain. We will describe possible ways to improve our ebeam spin devices, especially the ferromagnet/InAs interface, in Chapter 7.

Chapter 7 Conclusion

The experimental results of Chapters 4, 5, and 6 do not provide conclusive evidence for the existence of spin-coupled electronic transport in our devices. We believe that the many interesting results obtained with PL devices can be explained by the existence of strong local Hall voltages. In ebeam devices the influence of these Hall voltages was greatly reduced. However, although some of the results of polarize/analyze measurements of ebeam spin devices are not fully understood, the relative scarcity of hysteretic features in these small devices, coupled with the absence of a clear demonstration of the Hanle effect in our soft ferromagnet/low density 2DEG system, indicates that injection of a spin-polarized current from NiFe into InAs has not been reproducibly achieved. At the end of Chapter 2 we discussed the requirements for making a successful spin device: well behaved ferromagnets, spin-preserving InAs channels, and efficient transfer of a spin polarized current across the ferromagnet/InAs interfaces. The degree to which these requirements were met varied in our devices, as summarized below, but for the most part the first two points are well understood, whereas the last remains problematical.

Through the characterization of micro- and nanoscale ferromagnets using the local Hall effect, explained in Chapter 5, many of the shortcomings of early PL devices were rectified in later ebeam devices. These later devices contained planar magnets that switched sharply, at distinct coercivities, and that were also predominantly single-domain, as evidenced by the apparent equivalence of their remanent and saturation magnetizations. This implies that the role of micromagnetic domains, which could attenuate the spin-polarization of the injected current, is negligible, as there is essentially a single domain over the entire injection area. The intended reduction in the influence of local Hall phenomena was verified in the measurement results of Chapter 6. Unfortunately, the significant improvements to device properties greatly reduced the prevalence of hysteretic phenomena from their relative ubiquity in Chapter 4.

Assuming good injection of a spin-polarized current into InAs, the propagation of this spin-polarization through one of our patterned channels was addressed, in part, by the on-chip characterization, in ebeam devices, of our fabrication and by the separate measurement

of transfer resistance devices. These findings indicate that, while our fabrication may reduce the electron mobility of our channels, transport is still strongly ballistic for any device with contact separation on the scale of a few microns or less. Operation of devices at 4.2 K should therefore not suffer from spin-flip scattering. Addressing the other part of the question—whether spin polarization is preserved in our channels—involves an analysis of the Rashba precession mechanisms introduced in Chapter 2. Though this thesis is primarily a description of experimental work, later stages of the project have led to theoretical modeling of these precession phenomena. These are discussed in more detail below and in Appendix C. From the results of these modeling efforts we conclude that spin relaxation in our InAs channels should not destroy a signal, again given the assumption that appreciable spin-polarization is induced in the first place.

The nature of the ferromagnet/InAs contact is the least well understood part of this work. As discussed below, a good understanding of ferromagnet/normal metal interfaces (hence diffusive regime) exists in the literature. Also, ferromagnet/insulator/(normal metal or semiconductor) tunnel barriers have received attention. The case of a ferromagnet in direct contact to a high mobility semiconductor is relatively unexplored. Possible improvements to the devices discussed in this work, in light of the uncertain nature of the interface, are explained below.

7.1 Spin-Coupled Ballistic Modeling

Towards the end of this work, a concerted effort has been made to understand the role of ballistic transport in modifying our expectations for spin-coupled transport. Along with this, modeling of the effect of Rashba precession in our devices has confirmed that our smallest devices have, almost certainly, spin-preserving properties. The work discussed here is included to verify our earlier assumptions concerning the possibility of weak spin relaxation in our InAs channels. The results are due primarily to the theoretical and numerical efforts of Hongxing Tang. See Appendix C for a more thorough discussion of the ingredients of the model.

7.1.1 The Ballistic Hanle Effect

In the initial spin injection experiments of Johnson and Silsbee, in which Al was used as the free electron paramagnet, the Hanle effect was demonstrated by applying a magnetic field perpendicular to the plane of the sample. In those devices the Al foil was not etched into thin channels and even though the electron mean free path was over 15 μm the contact separation was often several times this value. Electrons propagating from injector to detector could thus follow numerous trajectories with large variation in the total integrated path length. Application of the perpendicular magnetic field induced precession of electrons as they followed these trajectories and the variance in path lengths yielded a variance in accumulated precession among the electrons. Eventually the spin-coupled signal decayed for magnetic fields large enough to cause a variance in precession of order π or greater. Since there was a broad distribution in transit lengths this decay was monotonic; no oscillation was expected (or observed) in the Hanle signal measured by Johnson and Silsbee.

In high mobility 2DEG devices such as ours, etched into narrow channels (less than 1 μm for ebeam devices), electrons are much better confined, and it is possible that most spins precess in-phase. In this case it is possible that *oscillations* may be observed in the Hanle signal., at least until the field becomes strong enough that dephasing takes place. (Dephasing will still occur due to the fact that the channel is not perfectly one-dimensional and transport involves multiple trajectories (1D subbands).) We can express this more succinctly as follows. The period of Hanle oscillations will be given by the field change, ΔB_z, that corresponds to a change in accumulated precession (through a change in Larmor frequency $\Delta\omega_L = (g^*\mu_B/\hbar)\,\Delta B_z$) of 2π radians for electrons propagating some distance $\langle L\rangle$ in a time $\langle t_{TR}\rangle = \langle L\rangle / v_F$; that is, $\Delta\omega_L \langle t_{TR}\rangle \approx 2\pi$, or,

$$\Delta B_z \approx \frac{2\pi\hbar v_F}{g^*\mu_B \langle L\rangle}. \tag{7.1}$$

The oscillation decay, on the other hand, is given by the field scale, δB_z, corresponding to π radians of precessional dephasing due to the variance in electron transit times, $\delta t_{TR} = \delta L/v_F$ (this is the same δt_{TR} introduced in Section 2.3.2). We therefore have

$$\delta B_z \approx \frac{\pi\hbar v_F}{g^*\mu_B \delta L}. \tag{7.2}$$

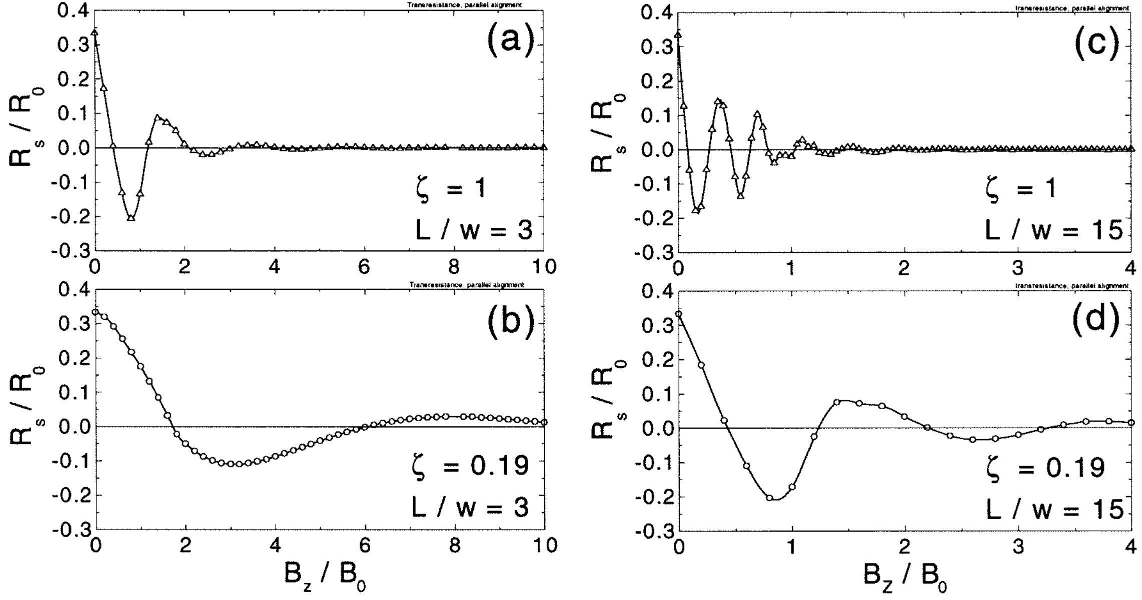

Figure 7.1: Calculation of the ballistic spin transresistance in an in-line geometry as a function of perpendicular magnetic field. In (a) and (b) the channel length-to-width ratio is 3 while in (c) and (d) it is 15. The material parameters used in (a) and (c) are for a ballistic metal, while in (b) and (d) they are for the InAs quantum wells used in this work. The axes are normalized as described in the text.

In order to observe oscillations in the Hanle signal we require that the decay length δB_z be much greater than the oscillation period ΔB_z: $\delta B_z >> \Delta B_z$ or, equivalently, $\delta L << \langle L \rangle$. These quantities will in general be geometry dependent, so we resort to computer modeling for our predictions of Hanle phenomena in high mobility InAs devices.

Figure 7.1 shows results for two different channel lengths and two different types of materials. The influence of material parameters is contained in the important factor $\zeta = \omega_L/\omega_c$ where $\omega_L = g^*(\mu_B/\hbar)B$ is the Larmor frequency and $\omega_c = eB/m^*$ is the cyclotron frequency. For a metal, $\zeta = g^*m^*/2m_e = 1$, but for an InAs quantum well, $\zeta = 0.19$. Since the ζ factor describes the degree to which a spin precesses during each cyclotron orbit, a smaller ζ implies weaker precessional phenomena, as seen in the Figure. We also see that a larger contact separation results in a smaller period of oscillation. This is because at larger separations the electrons have time to precess more as they travel from injector to detector. The vertical axes in Figure 7.1 are normalized to the Sharvin resistance R_o which depends on contact and channel geometry: $R_o = h/2e^2(k_F w/\pi)^{-1}$ for a 2D channel and an edge contact, with spin degeneracy. The horizontal axes in the Figure are normalized to the characteristic field scale $B_o = \hbar k_F/ew$ at which the cyclotron radius, $r_c = \hbar k_F/eB$, is

equal the electrical width of the channel, w. For $w = 0.5$ μm, we have $B_o = 3500$ G.

The large field scale of oscillations predicted in this model make observation of a Hanle signal difficult, as the magnetization state of the soft ferromagnets will have a tendency to change orientation with the application of sufficiently strong external magnetic fields. Moreover, for the weakly oscillatory case encountered in (b) of Figure 7.1 (for InAs material at small contact separation) the trace bears a strong resemblance to the magnetoresistive backgrounds we have encountered in some samples (see Figure 6.16). The origins of such backgrounds are unclear; they may be related to contact phenomena. In any case, we do not interpret them as evidence for spin injection because phenomena of similar magnitude have not been observed in the polarize/analyze experiments, i.e. with in-plane magnetic field. For nonlocal devices, the same difficulty holds—the Hanle effect occurs on a similar length scale as the cyclotron orbit-based decay of the transfer resistance. To remove the difficulties associated with these magnetoresistive backgrounds, we could sweep our external magnetic field in-plane but perpendicular to the ferromagnets' magnetization direction. However, the field strength needed to observe the Hanle effect would be large enough to perturb the ferromagnets (the same holds true, as mentioned above, for perpendicular fields, but for in-plane fields the situation is worse because the in-plane coercivities are smaller).

By making a device with large L/w the oscillation period due to Hanle precession is decreased so that we can, in principle, more easily separate Hanle phenomena from transfer resistance phenomena. Of course, the problem with this approach is that increasing L increases the role of both of bulk elastic scattering and diffuse boundary scattering, which will tend to attenuate the Hanle signal. We conclude this Section by stressing the importance of the above theoretical results. Unlike polarize/analyze experiments, Hanle experiments do not rely on switching the magnetization states of F1 and F2. Hanle precessional phenomena do not, therefore, compete with magnetoelectronic phenomena arising from local Hall voltages. Thus, despite the other difficulties associated with its demonstration, the Hanle effect is a crucial verification of spin-coupled transport. Such verification has been unambiguously demonstrated, to our knowledge, only once in the literature, and demonstrations of Hanle phenomena in the ballistic transport regime do not exist at all. Our efforts make firm predictions for the appearance of such phenomena.

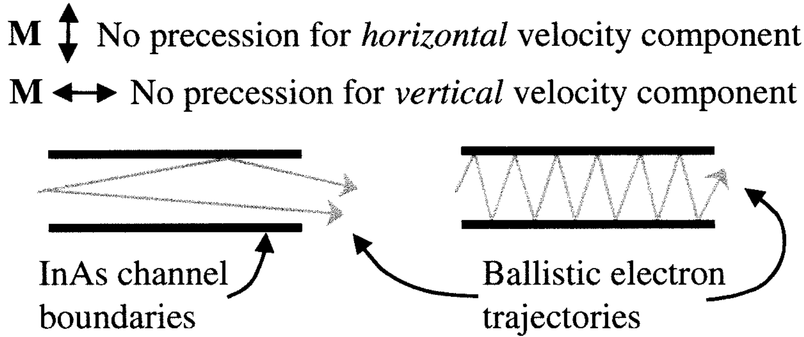

Figure 7.2: Schematic depiction of different electron trajectories, which will encounter differing amounts of spin precession depending on the orientation of **M**, the magnetization of the injector (and thus the direction of injected spins). For the usual geomety with vertical **M**, trajectories such as those on the left will experience little precession. The right trajectory will experience precession because it is bouncing back and forth across the channel, but the sense of rotation will change after each bounce so, assuming specular reflections, much of the precession will tend to average out. For horizontal **M** there will be a large amount of net precession for all trajectories, due to the predominantly horizontal velocity component.

7.2 Rashba Precession

Although spin-flip scattering events should be almost non-existent in our submicron InAs channels, due to their purity, there is still significant spin-dephasing via the Rashba effect. This phenomenon originates from the interfacial electric field in the heterostructure, which transforms into an effective magnetic field in the frame of reference of a moving electron. The basic form of the Rashba Hamiltonian was presented in Chapter 2. Here we will not go into the detailed physics of the phenomenon but instead demonstrate the relevance of the Rashba mechanism to our devices and to the proposed InAs spin transistor of Datta and Das. The degree of precession is very dependent on the relative orientation between an electron's spin and its velocity because the direction of B_R is dependent on the electron's velocity, as illustrated in Figure 7.2. For a carrier with velocity directed perpendicular to the magnetization of the ferromagnets (that is, for the normal injection geometry where the InAs channel is directed perpendicular to the magnetization direction), the effective Rashba magnetic field, B_R, is aligned or anti-aligned with the electron's spin and there is little precession. Some precession does occur, however, because electrons are injected into the channel with a distribution of incident directions, some with significant velocity components parallel to their spin. If the magnetization of the ferromagnets is oriented

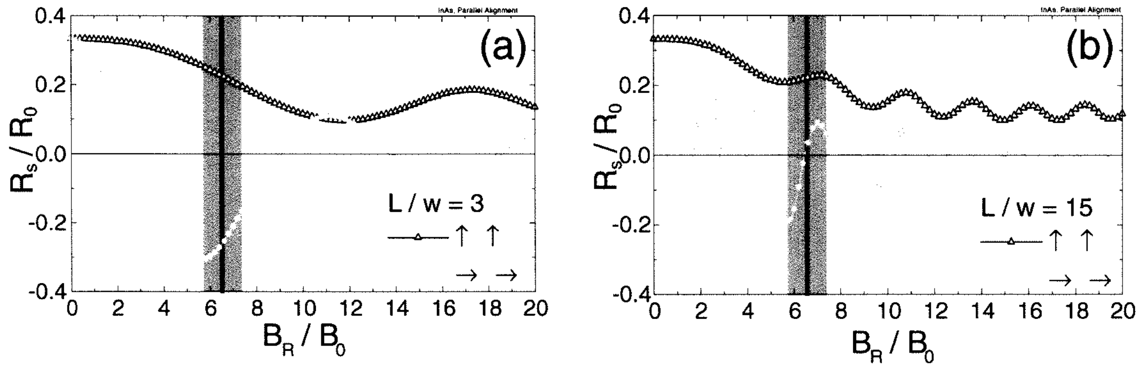

Figure 7.3: Modeling results for spin-coupled resistance vs. Rashba effective field in an InAs in-line device at $l/w = 3$ in (a) and $l/w = 15$ in (b). The black data is for Rashba field parallel to the injected spin direction while the gray data is for the perependicular case. The black line and shaded region denote the range possibly accessible to control by an electrical gate.

along the same direction as the InAs channel (so the electron's spin and net velocity are aligned) we expect stronger precessional effects because in this case B_R is perpendicular to the electron's spin.

Figure 7.3 shows simulation results for InAs channels at two different lengths and for two different orientations of B_R. The case for B_R aligned with spin (black) shows, as expected, weaker precessional oscillations than the case for B_R perpendicular to spin (gray). Assuming the Rashba mechanism is the dominant spin precession mechanism in our InAs quantum well (as it has been found to be in other InAs heterostructures), a typical value for the energy splitting is $\Delta_R = 2$ meV [22]. The effective Rashba field is then $B_R = \Delta_R/(g^*\mu_B) =$ 2.31 T. This value is shown on both of Figures 7.3(a) and (b) as a thick vertical line (the value in the Figures is normalized to the field scale $B_o = 3500$ G for $w = 0.5$ μm). For a channel with $w = 1$ μm this line would be moved to the right in the Figures by a factor of two. Figure 7.3(a) for $L/w = 3$ shows that spins are dephased somewhat for the size of B_R typically found in our quantum wells. Although these results do not include any bulk elastic scattering we note that such effects should be small for a device with contact separation less than a few microns, as in our smallest ebeam devices.[1] Moreover, at 750 nm, we have $L/w < 1$, so there should be less Rashba dephasing than in the Figure for $L/w = 3$. As mentioned in Chapter 2, we stress that Rashba precession is not equivalent

[1]This is certainly true for bulk elastic scattering. The role of diffuse boundary scattering, however, is somewhat uncertain and could be significant, especially at larger values of L/w. Note that the decay of spin polarization in these Figures is due only to geometry (path length variance).

to spin-flip scattering—for B_R perpendicular to spin we clearly get strong oscillations, but this does not lead to decay of the injected magnetization until the distribution of transit times between F1 and F2 becomes important (either due to geometry, elastic scattering in the bulk, or diffuse scattering at the channel sidewalls).

Finally we address the issue of the *tunability* of B_R, and hence the likelihood of making a spin transistor. This is important because such a demonstration would represent a significant technological achievement—an active circuit element whose operation is based on the control of spin transport phenomena, rather than on the modulation of charge densities. In Ref. [22], tunability of the energy splitting on the order of $\pm 25\%$ is achieved by applying a gate voltage between 0 and 1.5 V to an InAs quantum well confined by AlSb, similar to the heterostructure used in this work. The authors conclude, though, that this variation is the result of modulating the electron density, rather than the spin-orbit interaction constant, α. (The energy splitting can be expressed as $\Delta_R = 2\alpha k_F$ where this α is the same α as appears in Eqn. 2.15 . The energy splitting, and hence the effective magnetic field, therefore have an explicit dependence on carrier density through k_F.) Since the total spin precession acquired by an electron in traversing a distance L (assuming spin is perpendicular to B_R) is given by $\Delta\theta = 2m^*\alpha L/\hbar^2$ we see that unless α is changed, there is no variation in spin precession, and hence no gate control of spin-coupled transport. The Rashba effective field at zero gate voltage is shown in Figure 7.3 as a vertical black line at $B_R/B_o = 6.5$ (appropriate for $\Delta_R = 2$ meV).

Gate control of the spin-orbit interaction parameter has, however, been demonstrated in Ref. [21] for a slightly different materials system: InGaAs/InAlAs. In this case the authors found that α could be tuned by $\pm 25\%$ by applying a gate voltage between ± 1.5 V. Though we cannot apply this result directly to the results of our simulation (since the material parameters in the InGaAs systems are closer to $m^* = m_e/20$ and $g^* = 4$ and thus $\zeta = 0.1$) we can gain a sense of how broad this tunable region is by normalizing to our material values. The result is shown as the shaded region in Figure 7.3. Despite this approximation, the prospect of gate control of α looks promising, at least for the larger contact separation, assuming specularity of scattering at the channel boundaries is high. Further experimental work needs to be done to confirm the possibility of this gate control.

7.3 Interface Modeling Possibilities

Given that both our ferromagnets and our InAs channels are well behaved from the standpoint of spin injection, we conclude that the ferromagnet/InAs interface is either intrinsically an inefficient way to inject spin-polarization (because of, e.g., band structure effects) or there is a significant amount of spin-flip scattering due to interdiffusion of materials, or other non-idealities. In Chapter 2 we discussed some results from the literature for ferromagnet/normal metal interfaces. Here we provide a simple demonstration of the importance of the Fermi wavevector mismatch of spin subbands in spin transport across a metal/semiconductor interface, followed by a description of some results from spin-polarized tunneling work

7.3.1 A Simple Interface Model

The most obvious difference between a bi-metallic interface and a metal/semiconductor interface is that in the latter case there is a large density of states mismatch between the two materials. It has been suggested that since the electron density of states in a semiconductor is much smaller than in a metal, a semiconductor will be an inefficient probe of the spin imbalance of the density of states in a ferromagnet. That is, there are many electrons available for transport in the ferromagnet relative to the number of empty states in the semiconductor, and the fact that there is some imbalance in the ferromagnet's density of states is unimportant (of course, for a half-metallic ferromagnet in which electrons are 100% polarized at E_F, the density of states imbalance will dominate, but this is an extreme case). While this is true to some extent, a clearer insight can be gained by referring to Figure 7.4. The Figure (which implies an edge contact between the ferromagnet and the InAs—this is discussed more below) illustrates the difference in Fermi energies and Fermi wavevectors between the ferromagnet and semiconductor (while the Fermi circle representing the InAs 2DEG is accurate, the circle representing the three-dimensional ferromagnet is a gross approximation used for illustrative purposes). Assuming conservation of transverse momentum across the ferromagnet/InAs interface[2] we see that the InAs is sensitive only to a small slice of the ferromagnet's Fermi surface. The Fermi wavevector in our InAs has a magnitude of $k_{F,s} = 0.027$ Å^{-1} (for $E_F = 0.11$ eV). While the corresponding values for NiFe

[2]This assumption, common in modeling of tunneling phenomena, relies on a clean interface. If there is substantial roughness or interdiffusion of materials the assumption may not be valid.

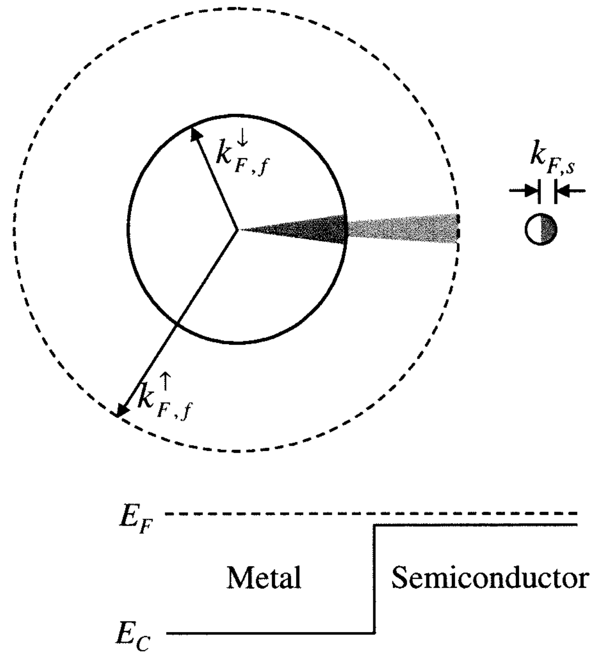

Figure 7.4: Schematic representation of the large difference between the Fermi energies and wave vectors in a ferromagnetic metal (left) and a degenerate semiconductor (right). The shaded slices in the circles are a simplified representation of the available states for injection, assuming conservation of transverse momentum. We assume $k_BT << E_F$ in both the metal and the semiconductor so that transport involves only those states near the Fermi surface. The difference in wavevectors between spin species in the ferromagnet are represented schematically as the difference in radii of the solid and dashed circles at the left. These pictures are not drawn to exact scale—see the text for a more accurate comparison of $k_{F,f}$ and $k_{F,s}$.

are not certain, we can put limits on them by using the numbers from Ni and Fe from [4]: $k_{F,f}^{\uparrow} = 1.09$ Å^{-1} and $k_{F,f}^{\downarrow} = 0.42$ Å^{-1} for Fe and $k_{F,f}^{\uparrow} = 1.16$ Å^{-1} and $k_{F,f}^{\downarrow} = 0.95$ Å^{-1} for Ni. (For comparison, in a normal metal with $n = 10^{23}$ cm^{-3}, the value is $k_F = (3\pi^2 n)^{1/3} = 1.4$ Å^{-1}.) This disparity between spin up and spin down wavevectors is also shown in the Figure.

Although the InAs may be insensitive to the density of states mismatch in the NiFe, it may not be insensitive to the mismatch in spin-resolved wavevectors, if transverse momentum is conserved across the interface. As discussed below, detailed knowledge of the interface is necessary to precisely model spin-polarized transport across an interface. Nevertheless we can gain some sense of the role the wavevector mismatch plays in the conductance by considering the simple quantum mechanical problem of a plane wave incident on a potential step, as depicted in the bottom of Figure 7.4. This problem is solved in quantum mechanics textbooks [86]; the result for the transmission is

$$T = 4\left[2 + \frac{v_{F,,f}\cos\theta_f}{v_{F,s}\cos\theta_s} + \frac{v_{F,s}\cos\theta_s}{v_{F,,f}\cos\theta_f}\right]^{-1} \tag{7.3}$$

where $v_{F,i}$ is the Fermi velocity in the ferromagnet or semiconductor ($i = f$ or s), and the angles θ_i describe the angle that $\mathbf{k}_{F,i}$ makes with the interface normal ($k_{F,f}\sin\theta_f = k_{F,s}\sin\theta_s$). Because of the mismatch in k_F we can make the approximation $\cos\theta_f \approx 1$. Conductance per unit width of the contact, for each spin type, is then [83]

$$\sigma = \frac{e^2 k_{F,s}}{2\pi h}\int_{-\pi/2}^{\pi/2} T(\theta_s)\cos\theta_s d\theta_s. \tag{7.4}$$

Numerical integration of the above expressions gives the following results for the contact resistance ($\rho = 1/\sigma$) for Fe: $\rho^{\uparrow} = 316\,\Omega\mu m$ and $\rho^{\downarrow} = 344\,\Omega\mu m$, and for Ni: $\rho^{\uparrow} = 318\,\Omega\mu m$ and $\rho^{\downarrow} = 312\,\Omega\mu m$. We therefore see that the difference in Fermi wavevectors between spin types can indeed result in a significant spin-resolved interfacial resistance, $\Delta R/R \approx 0.1$. We note that this treatment implicitly assumes an edge contact (as in the proposal of Datta and Das)—that is, a line contact between the 2DEG and the ferromagnet, rather than the planar contact used in our experiments. (Although our contacts are planar, the higher conductivity of the NiFe with respect to the InAs underneath it means that the current will tend to crowd into the 2DEG at the contact edge, approximating line injection.) Such

an edge contact could in principle be made by conventional processing steps, although the fabrication would be more difficult. We note also that edge contacts to a 2DEG have been made via cleaved edge overgrowth [87]. The real case in our experiments (planar contacts) has more stringent mode matching conditions across the interface, again assuming transverse momentum conservation. Since the above example fails to take into account any band bending in the InAs, let alone non-idealities such as interface states, contamination, or spin relaxation we do not pursue it further. Nor can we comment specifically on the likelihood of spin-dependent interfacial resistances in our NiFe/InAs systems, where the interface details are largely unknown. By controlling the interface details more carefully during fabrication we could more reasonably expect to develop an accurate model of spin-dependent transmission at the interface. One way to do this is to add a thin insulating barrier, or passivating layer, between the ferromagnet and the semiconductor.

7.3.2 Spin-Polarized Tunneling

In this Section we provide a brief overview of the theoretical understanding of spin transport through insulating barriers. Given the crucial importance of interface details elucidated in this thesis, it is probable that future semiconductor spin device efforts will be attempted using tunnel barrier contacts. Since the early results of Stearns [4] and Slonczewski [5] a large amount of theoretical and experimental work has been undertaken, especially with ferromagnet/Al_2O_3/(ferromagnetic or normal metal) junctions. This work has been motivated by the potential importance of these magnetic tunnel junctions (MTJs) as memory elements or field sensors. The efforts mentioned here are not intended to provide an all-encompassing review, but instead to give an overview of the state of current understanding. The essential distinction between these theoretical efforts and those described in Chapter 2, which deal with direct metallic interfaces, is that these efforts necessarily take a quantum mechanical approach to the tunneling phenomenon. They are thus better suited to the ballistic transport regime where one does not employ such concepts as local chemical potentials or constitutive properties such as electrical conductivities. (Of course, metallic multilayers can also be treated within a quantum mechanical formalism [88].)

The importance of band structure in modelling spin-polarized tunneling (in this case Fe/ZnSe/Fe) is stressed in Ref. [89]. Band alignment issues, and the efficiency of injecting spins from the majority and minority bands of different materials are, not surprisingly,

found to be very important in determining interfacial conductances. Other researchers have considered tunneling specifically from 3d ferromagnets [90] and have found, in the ballistic conductance regime, that tunneling current has a strong dependence on the nature of the covalent bonding between the ferromagnet and the insulator. Their results imply that the use of different insulating barriers can change not only the magnitude of the tunneling current's spin polarization, but also its sign (that is, whether majority or minority spins dominate). The same researchers have also considered the effects of disorder in the insulating barrier [91], finding that dominant contributions to the tunneling current come from a few random configurations of disorder that happen to provide highly conductive resonant channels. For the amount of disorder typically found in practical devices, spin polarization is found to decrease with increasing disorder and with increasing insulator thickness. The authors point out that this makes sense, qualitatively, by thinking in terms of one-dimensional tunneling through an effective potential barrier whose height decreases with increasing disorder.

Tunneling into a semiconductor has been considered, theoretically, in less detail than the metallic case, though a good treatment of the subject is given in Ref. [92]. As in some of the experiments on these systems, this theoretical treatment relies on creation of spin-polarized carriers by optical orientation, then treats the ferromagnet as a spin-filter for these polarized carriers. The authors find that significant reduction in the tunneling conductance can occur due to spin relaxation in semiconductor surface states. This is not surprising, but amplifies the conclusion that the detailed nature of the interface, whether a tunneling or direct contact, is very important to the observation of spin injection. Finally we note that in the experimental work of Ref. [14], involving some of the same authors of Ref. [92], it was found that a spin-polarized tunneling conductance measured in Co/Al_2O_3/GaAs (Zn or Si doped) was not present when the oxide barrier was removed (after correcting for magneto-optical effects). This result suggests that the passivation provided by the oxide barrier is a necessary component to achieving spin injection in GaAs.

7.4 Possibilities for the Future

It is clear from the above discussion that interfacial transport issues are complex: knowledge of factors such as interface states, barrier disorder, and band matching are all important

for gaining an understanding of spin-polarized transmission. This holds true whether a barrier is intentionally included or not. Our experiments and related theoretical modeling suggest, moreover, that spin-polarized transmission at our NiFe/InAs interfaces may not be occurring to any significant degree. In light of this, we now ask the question of what improvements can be made to the work described in this thesis.

The most obvious, first, recommendation would be to include tunnel barriers to achieve a solid state ferromagnet/insulator/semiconductor device (that is, one relying on electrical rather than 'optical' injection). For such a tunneling device, ohmic contacts are not required. Accordingly, we would not have to use InAs, although we may choose to continue to do so in order to reduce the barrier height to injected carriers. The work of other groups (see Section 1.2 for a listing), using optically pumped spin polarization, either through a tunnel barrier or directly into a semiconductor, suggests that semiconductor spin injection is possible, given the right combination of materials. Our only reservation in making this statement is that the spin relaxation of the hot electrons typically considered in these optical injection experiments may be significantly different from that of electrons at the Fermi energy, i.e. those relevant for a device operating under conditions of linear response. If a semiconductor other than InAs is used to demonstrate solid state spin injection, it is likely that one would still ultimately want to migrate to InAs, or InGaAs, since these narrow gap materials (in which the Rashba term is the dominant spin precessional effect) are the best candidates for gate control of spin-coupled transport. Moreover, the requirement of high mobility (for the gate control proposed by Datta and Das) can be relaxed if one intends only to demonstrate spin injection without gate control. At some point though, experiments with a sufficiently degenerately doped, low mobility, semiconductor would bear little distinction from the large body of work on metallic multilayers.

The use of different ferromagnets or semiconductors is advisable from the standpoint of band matching issues. It may be that NiFe and InAs are not well matched to each other. Although some brief attempts were made at CoFe/InAs structures, a more systematic investigation of different materials (hopefully with improved materials analysis) would be very informative. It is still probable that one would need to provide for fine control of interface properties though, possibly through the use of thin tunnel barriers, if only for passivation. Furthermore, as improvements are made in the growth of ferromagnetic semiconductors, one can envision exotic materials with tunable magnetoelectronic properties,

without the difficulties inherent in combining heterogeneous materials like ferromagnets and semiconductors.

The metallic experiments of Johnson and Silsbee, which served as the basis of our work and other numerous spin-coupled transport efforts, are now over ten years old. To our knowledge these experiments have not been successfully reproduced. (Given the success of other metallic multilayer systems, there has been little motivation to reproduce these difficult experiments). The ultimate goal of making a spin-FET is clearly difficult from a materials standpoint and it is unlikely that such a device would compete with GMR, spin valve, or MTJ devices. Nonetheless, the potential tunability afforded by a semiconductor spin device would be useful as a means of studying spin scattering and precession mechanisms. Also, aside from the goal of making a spin-FET, further spin-coupled ballistic modeling is an interesting topic that has to date received little attention. Such ballistic transport may prove to be helpful in the design of future metallic spin devices.

Our work provides an understanding for the most pressing difficulties, and how to address these difficulties, in the design and implementation of a solid state semiconductor spin device. Though not all of these obstacles have been successfully addressed—in that such a spin device has not been conclusively demonstrated—we note that our devices, and our predictions for device operation, have been consistently refined through the course of both our experimental and theoretical work. With the implementation of some of the materials improvements mentioned above we hope that conclusive demonstration of a spin transistor will occur in the near future.

Bibliography

[1] S. Datta and B. Das, Appl. Phys. Lett. **56**, 665 (1990).

[2] P.M. Tedrow and R. Meservey, Phys. Rev. Lett. **26**, 192 (1971); and P.M. Tedrow and R. Meservey, Phys. Rev. B **7**, 318 (1973). For an excellent review see R. Meservey and P.M. Tedrow, Physics Reports **238**, 173 (1994).

[3] B.D. Cullity, *Introduction to Magnetic Materials*, Addison-Wesley, Reading MA, 1972, pg. 617, 526.

[4] M.B. Stearns, J. Magn. Magn. Mater. **5**, 167 (1977).

[5] J.C. Slonczewski, Phys. Rev. B **39**, 6995 (1989).

[6] M. Julliere, Physics Letters **54A**, 225 (1975).

[7] A.G. Aronov, JETP Lett. **24**, 32 (1976).

[8] M. Johnson and R.H. Silsbee, Phys. Rev. Lett. **55**, 1790 (1985). For a more detailed account of the experiments see M. Johnson and R.H. Silsbee, Phys. Rev. B **37**, 5312 (1988) and M. Johnson and R.H. Silsbee, Phys. Rev. B **37**, 5326 (1988).

[9] M. Johnson, Phys. Rev. Lett. **70**, 2142 (1993) and M. Johnson, Science **260,** 290 (1993).

[10] S.S.P. Parkin, IBM J. Res. Develop. **42**, 3 (1998).

[11] D. Divincenzo, Science **270**, 255 (1995).

[12] J.Y.T. Wei, N.-C. Yeh, and R.P. Vasquez, Phys. Rev. Lett. **79**, 5150 (1997).

[13] S.F. Alvarado and P. Renaud, Phys. Rev. Lett. **68**, 1387 (1992).

[14] M.W.J. Prins, D.L. Abraham, and H. van Kempen, J. Magn. Magn. Mater. **121**, 152 (1993).

[15] A. Filipe, H.-J. Drouhin, G. Lampel, Y. Lassailly, J. Nagle, J. Peretti, V.I. Safarov, and A. Schuhl, Phys. Rev. Lett. **80**, 2425 (1998).

[16] F. Matsukura, H. Ohno, A. Shen, and Y. Sugawara, Phys. Rev. B **57**, R2037 (1998).

[17] I.P. Smorchkova, N. Samarth, J.M. Kikkawa, and D.D. Awschalom, Phys. Rev. Lett. **78**, 3571 (1997) and J.M. Kikkawa, I.P. Smorchkova, N. Samarth, and D.D. Awschalom, Science **277**, 1284 (1997).

[18] M. Oestreich, J. Hübner, D. Hägele, P.J. Klar, W. Heimbrodt, W.W. Rühle, D.E. Ashenford, and B. Lunn, Appl. Phys. Lett. **74**, 1251 (1999).

[19] J.M. Kikkawa and D.D. Awshcalom, Phys. Rev. Lett. **80**, 4313 (1998).

[20] J.M. Kikkawa and D.D. Awschalom, Nature **397**, 139 (1999).

[21] J. Nitta, T. Akazaki, and H. Takayanagi, Phys. Rev. Lett. **78**, 1335 (1997).

[22] J.P. Heida, B.J. van Wees, J.J. Kuipers, T.M. Klapwijk, and G. Borghs, Phys. Rev. B **57**, 11911 (1998).

[23] S.J. Koester, C.R. Bolognesi, M. Thomas, E.L. Hu, H. Kroemer, and M.J. Rooks, Phys. Rev. B **50**, 5710 (1994).

[24] G.L. Chen, J. Han, T.T. Huang, S. Datta, and D.B. Janes, Phys. Rev. B **47**, 4084 (1993).

[25] M. Johnson and R.H. Silsbee, Phys. Rev. B. **35**, 4959 (1987).

[26] M. Johnson and R.H. Silsbee, Phys. Rev. Lett. **60**, 377 (1988).

[27] P.C. van Son, H. van Kempen, and P. Wyder, Phys. Rev. Lett. **58**, 2271 (1987) and Phys. Rev. Lett. **60**, 378 (1988).

[28] A. Fert and S.-F. Lee, Phys. Rev. B **53**, 6554 (1996).

[29] J.J. Krebs, B.T. Jonker, and G.A. Prinz, J. Appl. Phys. **61**, 2596 (1987) and F.A. Volkening, B.T. Jonker, G.A. Prinz, and N.C. Koon, J. Appl. Phys. **67**, 5646 (1990).

[30] A. Filipe and A. Schuhl, J. Appl. Phys. **81**, 4359 (1997).

[31] G. Schmidt, G. Müller, L.S. Molenkamp, M. Behet, J. De Boeck, and P. Panissod, "Electrical and Structural Properties of Cobalt Contacts on Indium Arsenide," 3rd Int. Symposium on Metallic Multilayers, June 14-19 1998.

[32] J. Fabian and S. Das Sarma, Phys. Rev. Lett. **81**, 5624 (1998).

[33] R.J. Elliot, Phys. Rev. **96**, 266 (1954).

[34] Y. Yafet, in *Solid State Physics* **14**, edited by F. Seitz and D. Turnbull, Academic Press, New York (1963).

[35] R.N. Ghosh and R.H. Silsbee, Solid State Comm. **81**, 545 (1992).

[36] S. Bar-ad and I. Bar-Joseph, Phys. Rev. Lett. **68**, 349 (1992).

[37] V.E. Zhitomirskiĭ, V.E. Kirpichev, A.I. Filin, V.B. Timofeev, B.N. Shepel', and K. v. Klitzing, JETP Lett. **58**, 439 (1993).

[38] P.D. Dresselhaus, C.M.A. Papavassiliou, and R.G. Wheeler, Phys. Rev. Lett. **68**, 106 (1992).

[39] M.I. D'yakonov and V.I. Perel', Zh. Eksp. Teor. Fiz. **60**, 1954 (1971) [Sov. Phys. JETP **33**, 1053 (1971)].

[40] E.I. Rashba, Fiz. Tverd. Tela (Leningrad) **2**, 1224 (1960) [Sov. Phys. Solid State **2**, 1109 (1960)] and Y.A. Bychkov and E.I. Rashba, J. Phys. C **17**, 6039 (1984).

[41] G. Lommer, F. Malcher, and U. Rössler, Phys. Rev. B **32**, 6965 (1985) and F. Malcher, G. Lommer, and U. Rössler, Superlattices and Microstructures **2**, 267 (1986).

[42] C. Kittel, *Introduction to Solid State Physics*, 4th ed., Wiley, New York 1971.

[43] S. Datta and B. Das, Appl. Phys. Lett. **56**, 665 (1989).

[44] C. Nguyen, *Device Fabrication of InAs-AlSb Quantum Well Structures*, Appendix B of UCSB Ph.D. Thesis, 1993, pp. 130-152. and C. Nguyen, B. Brar, C.R. Bolgnesi, J.J. Pekarik, H. Kroemer, and J.H. English, J. Electron. Mater. **22**, 255 (1993).

[45] H. Kroemer, C. Nguyen, and B. Brar, J. Vac. Sci. Technol. B **10**, 1769 (1992) and C. Nguyen, B. Brar, H. Kroemer, and J.H. English, Appl. Phys. Lett. **60**, 1854 (1992).

[46] C. Gatzke, S.J. Webb, K. Fobelets, and R.A. Stradling, Semicond. Sci. Technol. **13**, 399 (1998).

[47] S. Gardelis, C.G. Smith, C.H.W. Barnes, E.H. Linfield, and D.A. Ritchie, preprint, Feb. 1999.

[48] A.F. Morpurgo, B.J. van Wees, T.M. Klapwijk, and G. Borghs, Appl. Phys. Lett. **70**, 1435 (1997).

[49] A. Scherer and M.L. Roukes, Appl. Phys. Lett. **55**, 377 (1989).

[50] C. Constantine, D. Johnson, S.J. Pearton, U.K. Chakrabarti, A.B. Emerson, W.S. Hobson, and A.P. Kinsella, J. Vac. Sci. Technol. B **8**, 596 (1990).

[51] S. Miyakuni, M. Sakai, R. Hattori, S. Izumi, T. Shimura, K. Sato, H. Takano, and M. Otsubo, J. Vac. Sci. Technol. B **12**, 530 (1994).

[52] M.L. Roukes, T.J. Thornton, A. Scherer, and B.P. Van der Gaag, in *Electronic Properties of Multilayers and Low-Dimensional Semiconductor Systems*; J.M. Chamberlain, L. Eaves, and J.-C. Portal, eds.; Plenum Press, New York 1990, pp. 95-116.

[53] C.W.J. Beenaker and H. van Houten, Phys. Rev. Lett. **63**, 1857 (1989).

[54] S.J. Koester, C.R. Bolgnesi, E.L. Hu, H. Kroemer, M.J. Rooks, and G.L. Snider, J. Vac. Sci. Technol. B **11**, 2528 (1993).

[55] F.G. Monzon and M.L. Roukes, J. Magn. Magn. Mater. **198**, 628 (1999).

[56] T.J. Thornton, M.L. Roukes, A. Scherer, and B.P. van de Gaag, Phys. Rev. Lett. **63**, 2128 (1989).

[57] F.G. Monzon, M. Johnson, and M.L. Roukes, Appl. Phys. Lett. **71**, 3087 (1997).

[58] M. Johnson, B.R. Bennett, M.J. Yang, M.M. Miller, B.V. Shanabrook, Appl. Phys. Lett. **71**, 974 (1997) and M. Johnson, J. Vac. Sci. Technol. A **16**, 1806 (1998).

[59] K.R. Carson and M.L. Rudee, J. Vac. Sci. Technol. **7**, 573 (1970).

[60] K.K. Choi, D.C. Tsui, and A. Alavi, Appl. Phys. Lett. **50**, 110 (1987).

[61] J. Reijniers and F.M. Peeters, Appl. Phys. Lett. **73**, 357 (1998).

[62] M.L. Roukes, A. Scherer, S.J. Allen, H.G. Craighead, R.M. Ruthen, E.D. Beebe, and J.P. Harbison, Phys. Rev. Lett. **59**, 3011 (1987).

[63] C.W.J. Beenakker and H. van Houten, Phys. Rev. Lett. **63**, 1857 (1989).

[64] F.G. Monzon, D.S. Patterson, and M.L. Roukes, J. Magn. Magn. Mater. **195**, 19 (1999).

[65] A.K. Geim, S.V. Dubonos, J.G.S. Lok, I.V. Grigorieva, J.C. Maan, L.T. Hansen, and P.E. Lindelof., Appl. Phys. Lett. **71**, 2379 (1997).

[66] Y. Zheng and J.-G. Zhu, J. Appl. Phys. **81**, 5471 (1997).

[67] M.R. Freeman, W.K. Hiebert, and A. Stankiewicz, J. Appl. Phys. **83**, 6217 (1998).

[68] J.-G. Zhu, Y. Zheng, and X. Lin, J. Appl. Phys. **81**, 4336 (1997) and J.-G. Zhu, personal communication.

[69] L. Kong and S.Y. Chou, J. Appl. Phys. **80**, 5205 (1991).

[70] M.E. Schabes, J. Magn. Magn. Mater. **95**, 249 (1991).

[71] W. Wernsdorfer, E.B. Orozco, K. Hasselbach, A. Benoit, D. Mailly, O. Kubo, H. Nakano and B. Barbara, Phys. Rev. Lett. **79**, 4014 (1997).

[72] S.E. Russek, J.O. Oti, S. Kaka, and E.Y. Chen, J. Appl. Phys. **85**, 4773 (1999).

[73] D.D. Awschalom, J.R. Rozen, M.B. Ketchen, W.J. Gallagher, A.W. Kleinsasser, R.L. Sandstrom, and B. Bumble, Appl. Phys. Lett. **53**, 2108 (1988).

[74] M.B. Ketchen, D.D. Awschalom, W.J. Gallagher, A.W. Kleinsasser, R.L. Sandstrom, J.R. Rozen and B. Bumble, IEEE Trans. Magn. **25**, 1212 (1989).

[75] W. Wernsdorfer, B. Doudin, D. Mailly, K. Hasselbach, A. Benoit, J. Meier, J.-Ph. Ansermet, and B. Barbara, Phys. Rev. Lett. **77**, 1873 (1996).

[76] M.R. Scheinfein, J. Unguris, D.T. Pierce, and R.J. Celotta, J. Appl. Phys. **67**, 5932 (1990).

[77] A. Tonomura, IEEE Trans. Magn. **29**, 2488 (1993).

[78] J. Unguris, R.J. Celotta, and D.T. Pierce, Phys. Rev. Lett. **79**, 2734 (1997).

[79] G.A. Gibson and S. Schultz, J. Appl. Phys. **73**, 4516 (1993).

[80] P.B. Fischer, M.S. Wei, and S.Y. Chou, J. Vac. Sci. Technol. B **11**, 2570 (1993).

[81] R. Proksch, E. Runge, P.K. Hansma, S. Foss, and B. Walsh, J. Appl. Phys. **78**, 3303 (1995).

[82] A.M. Chang, H.D. Hallen, L. Harriott, H.F. Hess, H.L. Kao, J. Kwo, R.E. Miller, R. Wolfe, and J. Vanderziel, Appl. Phys. Lett. **61**, 1974 (1992).

[83] R. Landauer, Phys. Rev. B **52**, 11225 (1995).

[84] M. Büttiker, Phys. Rev. Lett. **57**, 1761 (1986).

[85] H.X. Tang, F.G. Monzon, R. Lifshitz, M.C. Cross, and M.L. Roukes, submitted to PRL.

[86] C. Cohen-Tannoudji, B. Diu, and Franck Laloë, *Quantum Mechanics* vol. I, JohnWiley & Sons, New York 1977, pp. 67-71.

[87] W. Wegscheider, G. Schedelbeck, G. Abstreiter, M. Rother, and M. Bichler, Phys. Rev. Lett. **79**, 1917 (1997).

[88] S. Zhang and P.M. Levy, Phys. Rev. Lett. **81**, 5660 (1998).

[89] J.M. Maclaren, W.H. Butler, and X-G. Zhang, J. Appl. Phys. **83**, 6521 (1998) and J.M. Maclaren, X.-G. Zhang, W.H. Butler, and X. Wang, Phys. Rev. B **59**, 5470 (1999).

[90] E.Y. Tsymbal and D.G. Pettifor, J. Phys.: Condens. Matter **9** L411 (1997).

[91] E.Y. Tsymbal and D.G. Pettifor, Phys. Rev. B **58**, 432 (1998).

[92] M.W.J. Prins, H. Van Kempen, H. van Leuken, R.A. de Groot, W. Van Roy, and J. De Boeck, J. Phys.: Condens. Matter **7**, 9447 (1995) and R. Jansen, M.W.J. Prins, and H. van Kempen, Phys. Rev. B **57**, 4033 (1998).

Appendix A Recipe for Ebeam Spin Devices

We detail here the procedure for fabrication of ebeam spin devices using SiO_2 as a mask, noting differences between this process and others. Fabrication of PMMA-masked devices was similar, but different patterns were used for some of the layers, and the contact etch and ferromagnet deposition were combined into one layer. We also describe how wet etched PL devices were made with standard photolithography routines. Note that before any layers were fabricated the following procedure was carried out:

1. Spin protective photoresist (PR) layer onto wafer, bake 90° or 100° C, depending on type of PR (see below).
2. Scribe wafer into desired blocks, rinse in acetone.
3. Clean substrate: Trichloroethylene, Acetone, Methanol, each for approximately 1 min., ultrasound briefly if needed.

A.1 Photolithography Routines

These were the building blocks of all fabrication of large patterns. Two types of PR were used for liftoff. PR, as well as PMMA for ebeam lithography was dispensed from bottles with disposable plastic pipettes. Best results for application of resists was obtained when chips were spun off-center on the vacuum chuck. This reduced the size of edge-beads and made the coat more uniform. For all of the PL devices, and some of the templates for ebeam devices, we used the following.

A.1.1 (A) Shipley Microposit S1813 positive PR for Liftoff

1. Spin on, 5000 rpm, 45s.
2. Bake, 90° C, 5 min.
3. Chlorobenzene soak, room temperature, 2 min.
4. Bake, 90° C, 5 min.
5. Expose negative pattern (Cr mask with windows where deposition should occur), approximately 40 s.

6. Develop, Shipley MF319 PR developer, approximately 30 s.
7. Descum (optional, see below).
8. Deposition, and liftoff in acetone.

Due to concerns over the repeatability of the chlorobenzene soak, the following recipe was instituted for later ebeam templates, although the above recipe was still used at times.

A.1.2 (B) Hoechst Celanese AZ5214-E negative PR for Liftoff

1. Spin on, 5000 rpm, 45 s.
2. Bake, 100° C, 45 s.
3. Expose positive pattern, 10 s.
4. Bake, 124° C, 45 s.
5. Flood exposure (entire chip), 2.1 min.
6. Develop, AZ 327MIF PR developer, approximately 35 s.
7. Descum (optional, see below).
8. Deposition, and liftoff in acetone.

A.1.3 Descum

When patterning over chip regions where there was already Au, and/or for layers that had small regions intended for electrical contact to previous layers, we found that a descum step in an ozone dry stripper for 5 min to be useful. After this step a residual oxide layer was left on the chip surface, however, and a brief (few seconds) Ar ion mill at low voltage (usually 500 V) was necessary to remove the oxide. Due to concerns over damage to the semiconductor from the ion mill, these descum steps were not executed for large patterns on the bare semiconductor. This did not cause problems later in the processing.

A.1.4 (C) PR as an Etch Mask

The Shipley PR proved to be a good mask for all the wet etches used in this work, and for Ar ion milling. Typical procedure was as follows.

1. Spin on, 5000 rpm, 45s.
2. Bake, 90° C, 5 min.

3. Expose positive pattern, approximately 15 s.
4. Develop, Shipley MF319 PR developer, approximately 15 s.
5. Post-bake, between 90° C and 115° C, at least 3 min. (90° C worked adequately, but the temperature should not be raised above 15° C, to avoid damaging the PR).
6. Etch, then soak in acetone (for PR exposed to ion milling, ultrasonication was often necessary to remove the PR).

At times an etch step, wet or dry, was followed immediately by a metal deposition. In such cases process (A) was followed, with the addition of a brief post-bake as in (C). Deposition and liftoff then went as usual.

A.1.5 Photoresist Templates

1. Large InAs contact definition: process (A) with post-bake, ion mill or wet etch down to InAs, thermal evaporation of $\sim$ 80 Å Cr, $\sim$ 300 Å Au.
2. For PMMA masked devices: isolation etch, leaving small regions of active, unetched material, for ebeam lithography.
3. Interconnect metallization: process (A) or (B) and deposition of $\sim$ 80 Å CR, $\sim$ 1200 Å Au.

A.2 Ebeam Lithography

After definition of templates, which usually encompassed 8 to 16 chips of dimensions 3 mm $\times$ 3 mm, pairs, or sometimes individual, chips were scribed out for ebeam lithography. Beam voltage in the scanning electron microscope (SEM) was always 40 V, with a nominal working distance of 15 mm. Magnification was normally 1000$\times$ and the beam current was 10 pA. Bilayers of PMMA were applied as follows. Unless otherwise noted, procedures are for SiO_2-masked devices.

1. Spin on 4% PMMA, 3500 rpm, 45 s.
2. Bake, 180° C, 5 min.
3. Spin on 2% PMMA, 3500 rpm, 45 s.
4. Bake, 180° C, 5 min.

For PMMA-masked devices, one layer of 4% PMMA was used as an etch mask for Ar ion milling, with inconsistent results. In all cases developing was done by a solution of 3:1 isopropyl alcohol:4-methyl 2-pentanone.

A.2.1 Layer 1: SiO_2 Mask for Ferromagnetic Contacts

1. Apply PMMA bilayer.
2. Write pattern, typically with 400 Å line-to-line and center-to-center spacings, at dosage of 400 $\mu C/cm^2$.
3. Develop, $\sim$ 1 min.
4. Ebeam evaporate SiO_2, $\sim$ 1100 Å, for best results at less than 2 Å/s. This layer protects the future active channel area while leaving the contact area, and the rest of the chip, exposed.
5. Liftoff in acetone with brief, $\sim$ 1 s, ultrasonication.
6. Dry etch, either:
   (a) Ar ion mill for 2:30 min. at 300 V total voltage (beam plus accelerator), 10 mA beam current, and 5 sccm Ar flow (usual chamber pressure around 0.12 mTorr);
   –or–
   (b) ECR etch at 1.5 mTorr chamber pressure with 9:1 Ar:Cl_2, or pure Ar, at 20 sccm total flow rate with rf bias such that self-bias is 50 V dc. Timing of this etch varied but was on the scale of a few minutes. Test etches were always done prior to the real etch. In addition, small dots of PR were placed manually on a chip corner and then removed after the etch to check stepheight with the AFM. Further etching was done if stepheight was too low. The ECR etching was not as reproducible as desired.

A.2.2 Layer 2: Ferromagnetic Contact Deposition

1. Apply PMMA bilayer
2. Write pattern, typically with 200 Å line-to-line and center-to-center spacing, at dosage of 450 $\mu C/cm^2$.
3. Develop, $\sim$ 1 min.
4. (a) For PMMA-masked devices, execute contact etch with ion mill as above, then evaporate (thermally or by ebeam), with magnetic bias field, NiFe ($\sim$ 500 Å) and Au ($\sim$ 300 Å).
   –or–
   (b) For ion-milled, SiO_2-masked devices, evaporate NiFe and Au as above.
   –or–
   (c) For ECR-etched, SiO_2-masked devices, briefly ($\sim$ 5 s) clean InAs surface in ECR in pure Ar with same parameters as above; then thermally evaporate, without breaking vacuum, NiFe or CoFe ($\sim$ 200 Å, no bias field) and Au ($\sim$ 300 Å).
5. Liftoff in acetone, with or without ultrasonication depending on ease of liftoff.

A.2.3 Layer 3: SiO_2 Mask for Isolation Etch

1. Apply PMMA bilayer (or single layer for PMMA-masked devices).

2. Write pattern, typically with 200 Å line-to-line and center-to-center spacing, at dosage of 400 $\mu C/cm^2$. For SiO_2-masked devices this pattern covers most of the ferromagnets (except for the part to be contacted with the final metallization) and the injection region between the magnets; the rest of the chip, which has already been etched down to InAs, is now etched past the InAs (Au masks the larger chip areas). For PMMA-masked devices this pattern covers everything but two lines, each about 1 μm wide, on either side of the active channel. These trenches are etched to isolate the active channel from the rest of the InAs.

3. Develop, $\sim$ 1 min.

4. Ebeam evaporate SiO_2, $\sim$ 1200 Å.

5. Liftoff in acetone with brief ultrasonication.

6. Dry etch, either:

   (a) Ar ion mill, 3:15 for the SiO_2-masked, or 5:45 for the PMMA-masked devices;
   –or–

   (b) ECR etch at self bias of 100 V dc for approximately 3:30. Again this etch was not quite reproducible. Appropriate etch depth could be determine by observing color change of the chip surface.

7. For PMMA-masked devices, remove PMMA with acetone as much as possible. Likely necessary to descum in O_2 plasma.

A.2.4 Layer 4: Metallization to Connect Ferromagnetic Contacts

1. Apply PMMA bilayer.

2. Write pattern, typically with 200 Å line-to-line and center-to-center spacing, at dosage of 450 $\mu C/cm^2$.

3. Develop, $\sim$ 1 min.

4. Thermally evaporate connections from ferromagnetic contacts to previously deposited (by photolithography) Cr/Au lines, $\sim$ 80 Å CR, $\sim$ 1200 Å Au.

5. Liftoff in acetone.

In most cases through the course of ebeam processing some of the Cr/Au template lifted off or, in the case of SiO_2-masked devices, was thinned during the contact and isolation etches. Another metallization layer of photolithography was then performed for wirebond pads and interconnects, as in the initial template step, with $\sim$ 80 Å CR, $\sim$ 1500 Å Au.

Appendix B Calculation of Local Hall Fields

In this Appendix we detail the calculation of local Hall fields for two cases. The first case is for the PL LHE devices depicted in Figure 5.4. In this case we go on to compute a Hall resistance based on a simple spatial average of the calculated perpendicular magnetic field. The results are shown in Figure 5.6. In the second case we compute the perpendicular field gradient some distance out from the edge of a thin film ferromagnet.

B.1 Case 1: Calculation of $\langle B_z \rangle$ and ΔR_H for LHE Devices

As mentioned in Chapter 5, we would like to know what effect the non-single domain nature of our thin film ferromagnets might have on the average perpendicular field in a Hall cross underneath the ferromagnet. We model this by distributing the magnetic poles at the edge of the ferromagnet evenly over some volume of length δ back from the edge of the ferromagnet. This crudely estimates the effect of closure domains and lithographic roughness. An even better approximation would involve decreasing the pole strength depending on the degree to which closure domains decrease the magnetization at the edge of the chip. We do not attempt this, in part because such domains would vary with each magnet and also because we are more interested in how the fringe field decays away from the magnet than in its actual overall strength, which is actually modeled relatively well (within a factor of 2) by the simple line charge model of Chapter 5.

We take as our origin the point halfway up the magnet, at its end. We take the $\widehat{z}$ axis perpendicular to the chip surface and the $\widehat{x}$ axis along the current direction. We allow our magnet to be infinitely wide in order to simplify the calculation. As stated in Chapter 5 this likely affects the overall magnitude of our estimate but should not change the behavior of the field decay. Our magnetic charge per unit area is just M_s. The volume density is $\rho_m = M_s/\delta$. The magnetic field at a point $\mathbf{r}$ resulting from a differential element of magnetic charge at $\mathbf{r}'$ is

$$d\mathbf{B} = \frac{\rho_m d^3 r'}{|\mathbf{r} - \mathbf{r}'|} \frac{(\mathbf{r} - \mathbf{r}')}{|\mathbf{r} - \mathbf{r}'|^{1/2}}. \tag{B.1}$$

We are only interested, in this case, in the perpendicular component of magnetic field. Integrating the dot product of (B.1) with $\hat{z}$ and expanding the vector notation:

$$B_z(x) = \rho_m \int_0^\delta dx' \int_{-t/2}^{t/2} dz' \int_{-\infty}^{\infty} dy' \frac{z-z'}{(r^2 + r'^2 - 2\mathbf{r}\cdot\mathbf{r}')^{3/2}} \tag{B.2a}$$

$$= \rho_m \int_0^\delta dx' \int_{-t/2}^{t/2} dz' \left(z-z'\right) \int_{-\infty}^{\infty} dy' \left[x^2 + y^2 + z^2 + x'^2 + z'^2 - 2\left(xx' + zz'\right) + y'^2 - 2yy'\right]^{3/2} \tag{B.2b}$$

$$= 2\rho_m \int_0^\delta dx' \int_{-t/2}^{t/2} dz' \frac{(z-z')}{x^2 + z^2 + x'^2 - 2xx' + z'^2 - 2zz'} \tag{B.2c}$$

$$= \rho_m \int_0^\delta dx' \ln\left[\frac{(x-x')^2 + (x-x')^2}{(z-t/2)^2 + (x-x')^2}\right]. \tag{B.2d}$$

For the GaAs 2DEGs used in this phase of the experiments, the distance z is fixed (the vertical distance between the 2DEG and the center of the ferromagnetic thin film). We let $a = z - t/2$ denote the vertical distance from the 2DEG to the bottom of the magnet and $b = z + t/2$ the vertical distance from the 2DEG to the top of the magnet. We obtain

$$B_z(x) = \rho_m \int_0^\delta dx' \ln\left[\frac{b^2 + (x-x')^2}{a^2 + (x-x')^2}\right] \tag{B.3a}$$

$$= \rho_m \left\{ 2b\left[\tan^{-1}\frac{(\delta - x)}{b} + \tan^{-1}\frac{x}{b}\right] - 2a\left[\tan^{-1}\frac{(\delta-x)}{a} + \tan^{-1}\frac{x}{a}\right] + \delta\ln\left[\frac{b^2 + (x-\delta)^2}{a^2 + (x-\delta)^2}\right] + x\ln\left[\frac{\left(b^2 + (x-\delta)^2\right)\left(a^2 + x^2\right)}{\left(a^2 + (x-\delta)^2\right)\left(b^2 + x^2\right)}\right] \right\}. \tag{B.3b}$$

Thus for a given value of δ and a given magnet size and 2DEG depth we can calculate the perpendicular component of magnetic field at any point in the 2DEG. In order to turn this into a Hall resistance we make the approximation of spatially averaging the field in the cross region, neglecting any shorting effects that may occur in the 2DEG due to the inhomogeneous field. The limits of the averaged region depend on the magnet offset, s, relative to the cross-junction center, so in general terms:

$$\langle B_z \rangle = \frac{1}{x_{\max} - x_{\min}} \int_{x_{\min}}^{x_{\max}} B_z(x)dx, \tag{B.4a}$$

or, substituting in for $B_z(x)$,

$$\langle B_z \rangle = \frac{\rho_m}{x_{\max} - x_{\min}} \left\{ 2a \left[(x-\delta)\tan^{-1}\frac{(x-\delta)}{a} - x\tan^{-1}\frac{x}{a} \right] \right.$$
$$- \; 2b \left[(x-\delta)\tan^{-1}\frac{(x-\delta)}{b} - x\tan^{-1}\frac{x}{b} \right] - \frac{x^2}{2}\ln\left[\frac{x^2+a^2}{x^2+b^2}\right]$$
$$\left. + \; \frac{(x-\delta)^2}{2}\ln\left[\frac{a^2+(x-\delta)^2}{b^2+(x-\delta)^2}\right] - \frac{a^2}{2}\ln\left[\frac{a^2+(x-\delta)^2}{a^2+x^2}\right] + \frac{b^2}{2}\ln\left[\frac{b^2+(x-\delta)^2}{b^2+x^2}\right] \right\}\Bigg|_{x_{\min}}^{x_{\max}} . \tag{B.4b}$$

If the electrical width of the legs of the cross is w and the magnet offset is s, the averaging region spans $x_{\max} = s + w/2$ and $x_{\min} = s - w/2$. The total Hall resistance deflection in one of our LHE measurements is then $\Delta R_H = 2\langle B_z \rangle / n_s e$. A more careful accounting of the inhomogeneous fringe fields and the resulting Hall voltages in the LHE device is given in Ref. [61].

B.2 Case 2: Calculation of $\partial B_z/\partial z$

Another potentially useful calculation is the strength of the field gradient $\partial B_z/\partial z$ some distance away from the edge of the ferromagnet. For this calculation we use the same coordinate system as above ($\widehat{z}$ direction perpendicular to the plane of the ferromagnet, $\widehat{x}$ direction along the long axis of the ferromagnet, and the origin in the center of the edge of the film), but we no longer assume that the magnet is infinite in the $\widehat{y}$ direction, and we take the magnetization charge density as concentrated on the magnet's surface ($\delta = 0$). For a magnet of width w and thickness t the $\widehat{z}$-field gradient at some point $\mathbf{r}$ resulting from a differential element of magnetic charge at $\mathbf{r}'$ is

$$\partial B_z/\partial z = \frac{\partial}{\partial z}\left\{ M_s \int_{-t/2}^{t/2} dz' \int_{-w/2}^{w/2} dy' \frac{z-z'}{|\mathbf{r}-\mathbf{r}'|^3} \right\}. \tag{B.5}$$

All of our charge is at the edge of the magnet, so we let $x' = 0$. Expanding the vector notation,

$$\partial B_z/\partial z = M_s \frac{\partial}{\partial z} \int_{-w/2}^{w/2} dy' \int_{-t/2}^{t/2} dz' \frac{z-z'}{\left[x^2 + (y-y')^2 + (z-z')^2\right]^{3/2}} \tag{B.6a}$$
$$= - \; M_s \frac{\partial}{\partial z} \int_{-w/2}^{w/2} dy' \int_{z+t/2}^{z-t/2} dp \frac{p}{\left[x^2 + (y-y')^2 + p^2\right]^{3/2}}, \tag{B.6b}$$

where we have made the variable substitution $p = z - z'$. Evaluating the first integration we obtain

$$\partial B_z/\partial z = M_s \frac{\partial}{\partial z} \int_{-w/2}^{w/2} dy' \left\{ \frac{1}{\sqrt{x^2 + (y-y')^2 + (z-t/2)^2}} - \frac{1}{\sqrt{x^2 + (y-y')^2 + (z+t/2)^2}} \right\}. \tag{B.7}$$

We make another substitution, $q = y - y'$, and evaluate the integration:

$$\partial B_z/\partial z = - M_s \frac{\partial}{\partial z} \ln \left\{ \frac{\left[y - w/2 + \sqrt{x^2 + (y-w/2)^2 + (z-t/2)^2}\right]}{\left[y + w/2 + \sqrt{x^2 + (y+w/2)^2 + (z-t/2)^2}\right]} \times \frac{\left[y + w/2 + \sqrt{x^2 + (y+w/2)^2 + (z+t/2)^2}\right]}{\left[y - w/2 + \sqrt{x^2 + (y-w/2)^2 + (z+t/2)^2}\right]} \right\}. \tag{B.8}$$

Before taking the derivative we can use the above expression to compute B_z, if needed. Upon taking the derivative we find

$$\begin{aligned} \partial B_z/\partial z = M_s \Bigg\{ & \frac{z - t/2}{\sqrt{x^2 + (y+w/2)^2 + (z-t/2)^2}\left[y + w/2 + \sqrt{x^2 + (y+w/2)^2 + (z-t/2)^2}\right]} \\ & + \frac{z + t/2}{\sqrt{x^2 + (y-w/2)^2 + (z+t/2)^2}\left[y - w/2 + \sqrt{x^2 + (y-w/2)^2 + (z+t/2)^2}\right]} \\ & - \frac{z - t/2}{\sqrt{x^2 + (y-w/2)^2 + (z-t/2)^2}\left[y - w/2 + \sqrt{x^2 + (y-w/2)^2 + (z-t/2)^2}\right]} \\ & - \frac{z + t/2}{\sqrt{x^2 + (y+w/2)^2 + (z+t/2)^2}\left[y + w/2 + \sqrt{x^2 + (y+w/2)^2 + (z+t/2)^2}\right]} \Bigg\}. \end{aligned} \tag{B.9}$$

We can gain a feel for how B_z and $\partial B_z/\partial z$ behave by looking at a few examples. We use a value for M_s from our NiFe magnets, 838 emu/cm^3. We let $y = 0$ and $x = 100$, 200, 300, and 400 nm, and we vary z. The results for a magnet 1 μm wide and 150 nm thick are shown in Figure B.1. We note that B_z is zero on axis ($y = z = 0$), as we might expect, while $\partial B_z/\partial z$ is maximum, decaying to zero in just over 100 nm of $\hat{z}$ displacement for

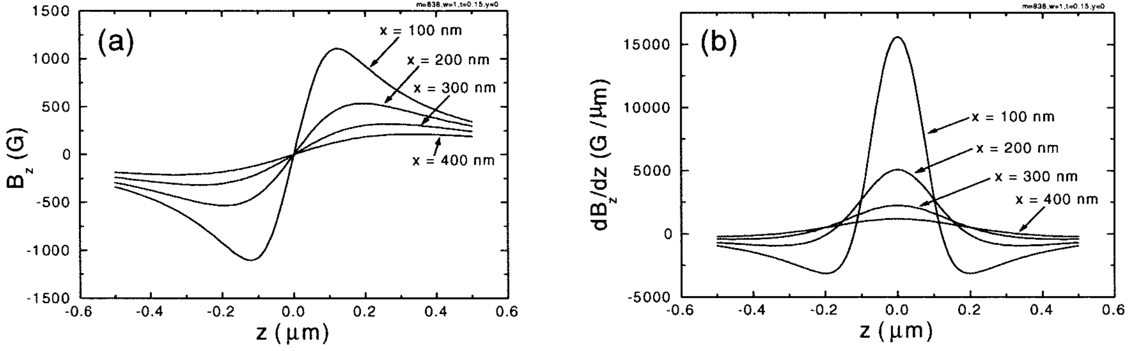

Figure B.1: Plots for B_z in (a) and $\partial B_z/\partial z$ in (b) at on-axis distances of $x = 100$, 200, 300, and 400 nm away from the magnet's face.

$x = 100$ nm. The maximum field achieved in B_z is over 1000 G for 100 nm separation, but it decays rapidly. In the above calculations we neglected contributions from the opposite face of the magnet, assuming that such contributions are negligible. Since B_z decays very rapidly this is a very good assumption provided the magnet's length is appreciably larger than its other dimensions. We also note that both the peak in B_z and the decay in $\partial B_z/\partial z$ broaden at the larger separation. From the plot for $\partial B_z/\partial z$ we see that the maximum values for the derivative for each of $x = 100$, 200, 300, 400 nm are about 15,600; 5,070; 2,230; 1180 G/μm, respectively. The dependence of $\partial B_z/\partial z$ on x is shown more explicitly in Figure B.2. We see that the derivative decreases very rapidly for $x < 200$ nm, and at 1 μm has diminished to only 110 G/μm. The inset shows a contour plot for B_z, where it is clear that the maximum in $B_z(z)$ shifts toward smaller values of z as x is decreased. Finally, we plot $\partial B_z/\partial z$ vs. y in Figure B.3. In this case the decay of the derivative is much less rapid, compared to Figure B.1(b), as the off-axis distance is increased. This is related to the fact that the magnet is much wider than it is thick. From the above calculations for the strength of B_z and $\partial B_z/\partial z$ near a thin film ferromagnet, along with the results of Chapter 5 which demonstrate the robustness of the LHE, it is likely that, in the future, novel magnetoelectronic device concepts based on the LHE will be investigated.

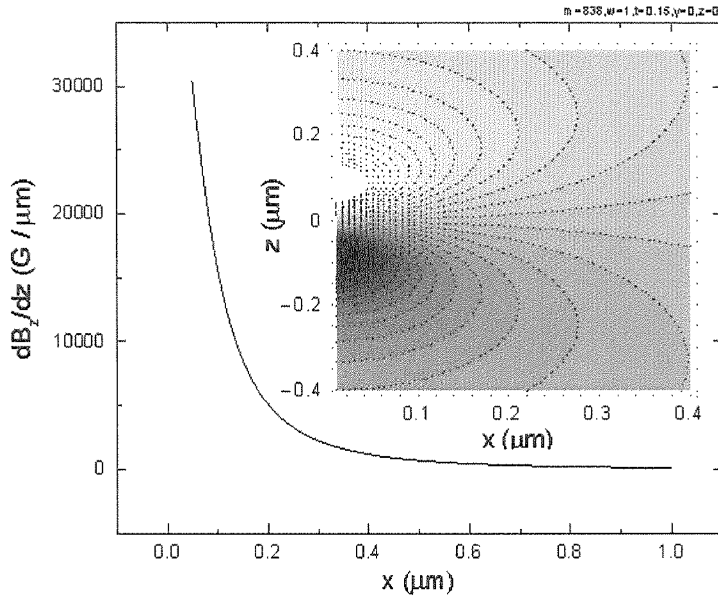

Figure B.2: Modeling results for the decay of $\partial B_z/\partial z$ with x. In the inset we show a contour plot for B_z. The contours are evenly spaced, with lighter shading for more positive values. The last full contour on the right of the inset is for a value of 210 G and the contours demarcate values for B_z separated by 150 G.

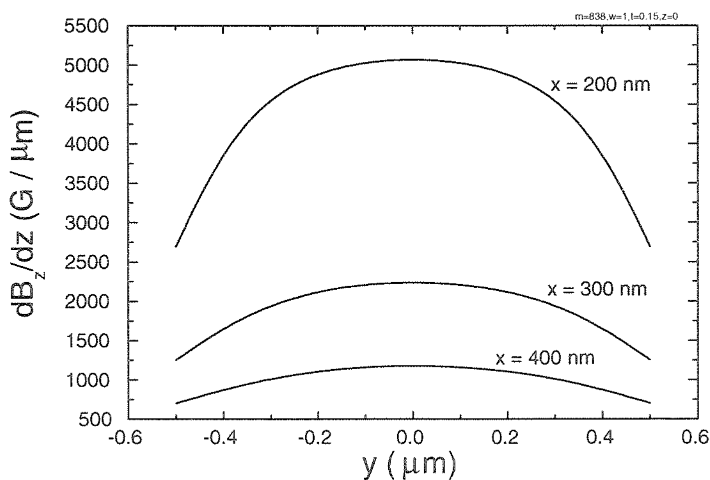

Figure B.3: Modeling results for the decay of $\partial B_z/\partial z$ vs. y for separations of 200, 300, and 400 nm.

Appendix C Transfer Resistance Devices and Ballistic Modeling

One method of characterizing the ballistic nature of high mobility 2DEGs is through the observation of the transfer resistance phenomenon [52][53]. Although this phenomenon will not be explained at length here, we point out the relevant characteristics of a transfer resistance device in Figure C.1. The measurement is a nonlocal resistance (or transresistance) measurement vs. applied perpendicular magnetic field. For diffusive systems this measurement gives a constant resistance value that decreases to zero as the separation L is increased. In ballistic systems, however, where the mean free path of electrons, l_e, is of the same order or larger than L a prominent magnetoresistive feature, centered about zero magnetic field, is obtained, as shown in Figures 4.12(a) and (b) and Figure C.2. In the ballistic transport regime it is not appropriate to speak of local chemical potentials in the high mobility 2DEG for length scales shorter than l_e. Instead we treat the InAs channels as perfect conductors connecting electron reservoirs (the disordered contacts), in the spirit of the Landauer-Büttiker (LB) model, as described below.

Aside from the channel length L, channel electrical width w, and mean free path l_e, there are in principle three additional device parameters that characterize a transfer resistance device. These are: 1) the degree to which boundary scattering is specular, p, 2) the radius of curvature, r, of the corners of the junctions, and 3) the lead length, or the relevant length of the channel between the junction region and the reservoirs, L^*. Computer modeling experiments, based on the LB model of ballistic transport [83][84], confirm the importance of these parameters in understanding the details of transfer resistance phenomena (this model will be discussed in slightly more detail below, where it has been extended to include spin-polarized electrons and reservoirs, and spin precession). An example of a simulation is shown in Figure C.2(b). (As in the simulations of Chapter 7, resistance is normalized to the Sharvin resistance R_o and magnetic field is normalized to the characteristic field scale $B_o = \hbar k_F/ew$. For $w = 0.5$ μm, $B_o = 3500$ G.) Referring to Figure C.1, the basic form of a transfer resistance curve results from the fact that electrons injected from the left

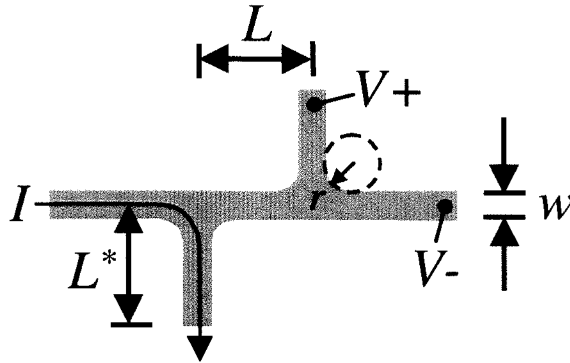

Figure C.1: Schematic drawing of a transfer resistance device with channel width w (which in general can be less than the lithographic width due to electrical depletion at the channel edges), channel length L, junction radius of curvature r, and lead length L^*.

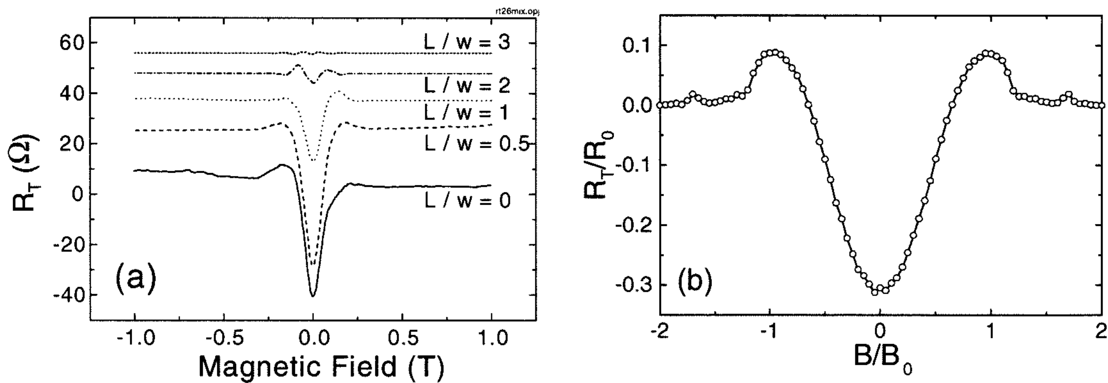

Figure C.2: Example transfer resistance curves (a) for SiO_2-masked ebeam InAs devices with channel width 1 μm. Curves are offset vertically for clarity. In (b) we display the result of a computer simulation with $L/w = 1$, $L^*/w = 1$, $r/w = 0.5$, $p = 0$, and $l_e = \infty$.

lead have a tendency to propagate ballistically through the channel longitudinally, beyond the net path of the current, rather than being (diffusively) scattered along a path leading to the bottom lead (the current sink lead). Electrons therefore accumulate in the right lead, raising its chemical potential until the *net* flow satisfies the boundary conditions. Voltage measured between the top and right leads is therefore negative at zero applied magnetic field, reflecting the anisotropic angular distribution of the electron flux incident upon these reservoirs. As the magnetic field is increased electrons follow curved trajectories, eventually executing skipping orbits along the channel sidewalls. When fully developed, this regime causes the transfer resistance signal to decay. By counting electrons injected into each reservoir the transmission coefficients into each lead, the chemical potentials at the reservoirs, and thereby the resistances involving different pairs of leads, are calculable.

For the purposes of the spin devices discussed in this thesis, transfer resistance devices have been employed as a tool for verifying the ballistic nature of our InAs channels. Since the transfer resistance signal is easily degraded by channel defects or edge roughness, the observation of the phenomenon is a qualitative indicator of channel quality and optimal fabrication. We also used these devices as a check for device isolation. To achieve channel definition in our initial attempts at ebeam fabrication of transfer resistance devices, we utilized PMMA as a mask for subtractive patterning of isolation trenches (just as in the early ebeam spin devices where PMMA was used as the isolation mask). Figure C.3(a) shows the layout of three devices in a set of photolithographically defined finger pads. Devices with channel widths of 0.5, 0.75, and 1 μm were fabricated with L/w ratios of 0, 0.5, 1, 2, 3, 5, 7, and 10 μm. In the Figure there are bright lines, marking the edges of the isolation trenches, due to residual bits of PMMA. In certain places these bits have clearly been removed—a close-up of such a region is shown in (b). Measurement results from PMMA-masked transfer resistance devices were not reproducible, even though the processing was straightforward and often appeared very clean (close-ups of two devices are shown in (c) and (d) of Figure C.3). It was determined that this was due to inconsistent removal of PMMA in the regions designated for ion milling, leading to inconsistent device isolation. Later devices fabricated with SiO_2 masking gave much more consistent results both in terms of device isolation and in the observation of transfer resistance.

Results from transfer resistance measurements of SiO_2-masked devices are shown in Figure C.4 where the size of the transfer resistance dip at zero applied field is plotted vs.

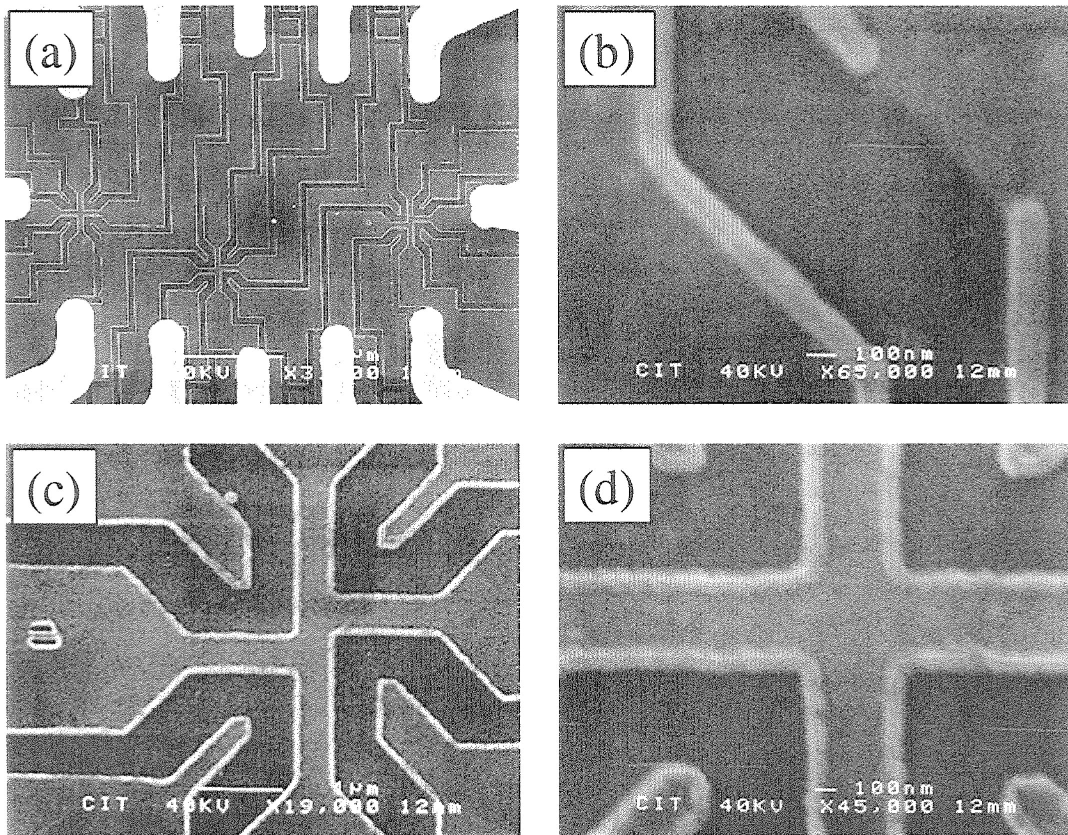

Figure C.3: Micrographs of PMMA-masked ebeam transfer resistance devices. In (a) is the overall layout of finger pads along with three devices with 500 nm wide channels. The same layout was used for SiO_2-masked devices. Note the bright lines resulting from PMMA residue. In (b) we display a close-up of an isolation trench where the PMMA residue is partially removed. In (c) and (d) are close-ups of devices with $w = 500$ nm, and $L/w = 1$ and 0, respectively.

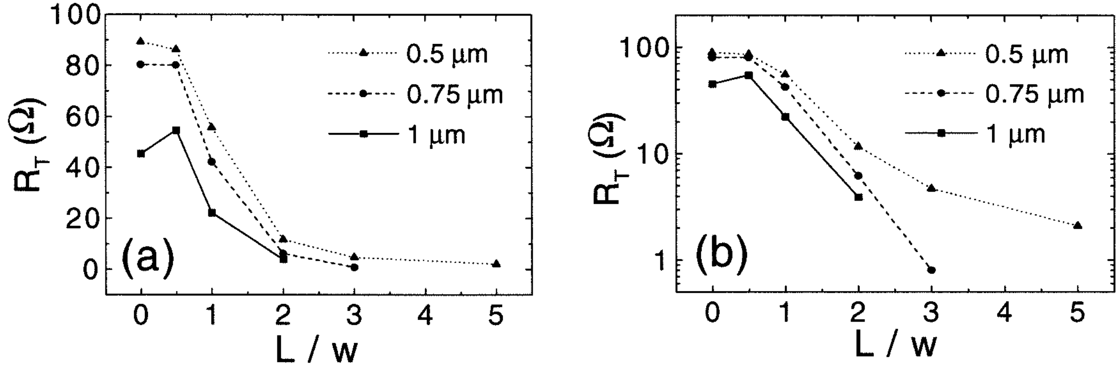

Figure C.4: Maximum transfer resistance (at zero field) vs. lead separation for devices with channel widths of 0.5, 0.75, and 1 μm. Linear plot in (a), semi-log in (b).

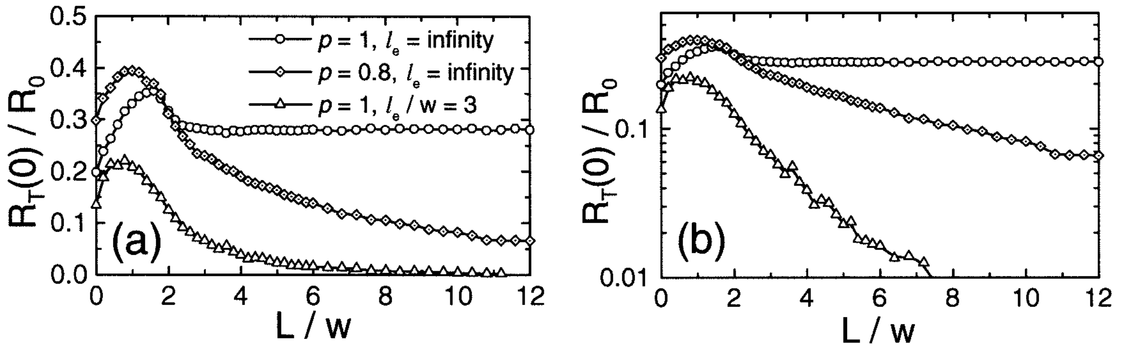

Figure C.5: Simulation results of maximum transfer resistance vs. lead separation for $L^*/w = 1$ and $r/w = 0.25$. Boundary scattering specularity p and mean free path l_e are varied. Linear plot in (a), semi-log in (b).

channel length. Boundary scattering is modeled by a specularity (i.e. Fuchs) parameter; for completely specular scattering $p = 1$, while for the completely diffuse case $p = 0$ (see Ref. [52]). Some further simulation results, varying p and l_e for $L^*/w = 1$ and $r/w = 0.25$ are shown in Figure C.5. For $p = 1$ and $l_e = \infty$ there is no scattering in the junction and a transfer resistance exists for arbitrarily large separation, L/w. Also note that for all of the plots the maximum R_T occurs not at $L/w = 0$ but at some small value which depends on other parameters—this can also be seen in Figure C.2(a) or Figure C.4 for $w = 1$ μm (for the other values of w there are not enough points to capture the hump in R_T). As p and l_e are decreased, the decay of R_T vs. L/w happens more quickly.

Details such as the asymmetries apparent in Figure C.2(a) are not likely to be captured by simulations because they arise from processing imperfections or impurities in the InAs

itself. Nevertheless, general trends such as the influence of decreasing p and l_e mentioned here are readily captured by our modeling. Future work will address the separate influence of each of the device parameters L, w, p, l_e, r, and L^* on the behavior of transfer resistance devices with the aim of a more complete understanding of ballistic transport, and of the role of surface and bulk scattering processes, for both the spin-polarized and unpolarized cases.

C.1 Landauer-Büttiker Formalism Applied to Spin-Polarized Currents

Here we briefly elaborate on the discussion of the computer modeling of ballistic transport outlined above. We also extend the modeling to include spin-polarized electrons. From this we are able to delineate concrete expectations, in the *ballistic* transport regime, for Hanle phenomena (precession of spins in the presence of a perpendicular external field) and for the importance of Rashba precessional mechanisms, as presented in Chapter 7.

Both in-line and nonlocal device geometries can be modeled using the Landauer-Büttiker (LB) formalism. Figure C.6 shows a schematic view of our modeling paradigm for the in-line geometry. In this case we calculate the ballistic spin transresistance with either the current source or sink contact ferromagnetic, and similarly for the voltage contacts. Voltage is detected nonlocally; that is, the probe configuration is the R_m configuration of Chapters 4 and 6. As a first approximation we assume our ferromagnets are 100% spin-polarized (half-metallic) and that there is no spin-flip scattering at the ferromagnet/InAs interface. We thus reduce the problem to a question of how a spin-polarized current behaves once it is injected into a 2DEG. (Interface issues and their relation to spin injection are discussed in Chapter 7.) This problem is further broken down into eight reservoirs, rather than four as in the standard LB model. Two reservoirs represent the unpolarized, normal metal, contacts which accept all electrons regardless of spin orientation. Two represent the fully spin-polarized ferromagnets, with nonzero density of states at the Fermi level for only one spin orientation. In perfect contact with each of these ferromagnets are two more reservoirs, one for spin up and one for spin down electrons. These four spin-resolved reservoirs, labeled $1\uparrow$, $1\downarrow$, $2\uparrow$, and $2\downarrow$ in Figure C.6, model the disordered, but still spin preserving, regions beneath the ferromagnetic contacts in our real devices. We assume that in these regions

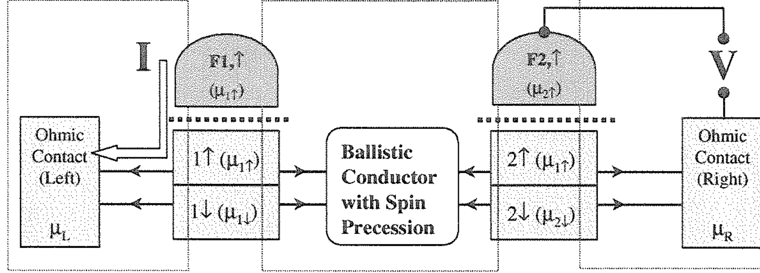

Figure C.6: Schematic representation of the basic components of our ballistic transport model with spin polarization and precession, for the in-line geometry. Chemical potentials are defined at each reservoir.

local equilibrium and, therefore, separate electrochemical potentials exist for the *separate* spin bands. Thus our spin-selective contacts are comprised of essentially two elements: the ferromagnet and the momentum randomizing but spin-preserving reservoirs underneath the ferromagnets. This is intended to approximate the InAs contact areas which, having the cap material removed and being exposed to the ferromagnets, have significantly shorter electron mean free paths than the unexposed InAs quantum well but (hopefully) spin relaxation lengths that are still long.

A more detailed account of the calculation can be found in Ref. [85] but the basic procedure is as follows. The problem separates into three sub-problems, two of which yield relations between the electrochemical potentials at 1 and 2; the electrochemical potentials at the device contacts F1, F2, L (left), and R (right); and the imposed current. The third problem reduces to a four probe calculation involving the reservoirs at 1 and 2, and the multichannel conductor, representing the device channel, in which electrons can precess as they propagate. The solution of this reduced problem is approached semi-classically: electrons are injected at one of the leads with velocity $\mathrm{v} = v_F(\cos\alpha)/2$ where $\alpha = 0$ denotes the direction straight down the channel. The transresistance can then be expressed in terms of the spin-resolved transmission probabilities T_{ij} that measure the likelihood of transmission from lead i to lead j. These probabilities are in turn calculated numerically, using a semiclassical Monte Carlo technique in which we follow ballistic electron trajectories and the phase of spin wavefunctions through the device, while ignoring the phase of the spatial part of the electron's wavefunction. Though our model is set up to account for elastic scattering both at the channel boundaries and within the 2DEG channel, the preliminary

results discussed here assume specular reflection from the boundaries and no scattering in the channel. Spin precession due both to external and internal magnetic fields can be included. With these ingredients, our simulations are able to produce detailed predictions for spin-coupled transport in the ballistic regime.